

Diss. ETH No. 25361

Through X-ray eyes: Solar flares and advances in observational techniques

A thesis submitted to attain the degree of
DOCTOR OF SCIENCES of ETH ZÜRICH
(Dr. sc. ETH Zürich)

presented by

MATEJ KUHAR

Mag. Phys., University of Zagreb

born on 03.08.1990

citizen of Croatia

accepted on the recommendation of

Prof. Dr. Günther Dissertori

Prof. Dr. Säm Krucker

Prof. Dr. Astrid Veronig

2018

Acknowledgments

First of all, I give my greatest gratitude to Säm Krucker for all his help, advices and knowledge passed onto me, and for giving me the chance of growing professionally in a friendly and open environment. I cannot think of a more compatible advisor, both professionally and on a human level. He has been a great mentor in every meaning of the word, and I hope our collaboration to continue for many years.

Big thanks to my *STIX* advisor, Diego Casadei, for giving me a different perspective to physics and research (and Italian cousine together with his family). He has been there in every bump on the rocky path of *STIX* grids analysis. Special thanks to Gordon Hurford as well, an encyclopedia on space science instrumentation. It's been a privilege to learn from you, guys.

A special 'thank you' to other members of our heliophysics group at FHNW. I hope I do not skip anyone: Marina (thanks for reading the manuscript), Lucia, Erica, Brandon, Oliver, Stefan and Rohit.

Gratitude goes to my official advisor at ETH, professor Günther Dissertori, for being open and giving me the chance to do this research by accepting me to the ETH doctorate studies.

Big thanks to professor Astrid Veronig for agreeing to be a co-examiner and for reading the manuscript. And also to professor Andreas Vaterlaus for chairing the committee.

Special thanks goes also to my master thesis advisor Roman Brajša, for supporting me and directing me always in the right paths. Two things he never stopped doing.

Finally, I thank all my math and physics teachers who lit the spark of interest for physics in me: Tanja Popović, Slavica Bošnjak, Ivan Lalić, Marija Radovanović, Drago Danilović and Katica Matić. And above all, grandma Janja.

Emotional path to the thesis was as interesting as the profesional one, with numerous people influencing me one way or another. Thanks to my high school friends for giving me a healthy, not-PhD-related-time filled with fun. And especially to Domagoj, the oldest friend of all. Contacts with my faculty friends have also made my life a lot easier and more fun. I am glad to have you in my life.

Coming to Switzerland was never easy, despite its (fulfilled) reputation of one of the best countries in the world. I thank my many friends here for making life a little bit better and more interesting every time we met. This includes everything from beers in the pub, wanders in the nature, watching football games (go Croatia!) or playing tennis in Untersiggenthal.

Acknowledgments

I am also extremely grateful to additional families I obtained during my studies. The first one is of my best-man Marko and his wife Marijana, together with their newborn kid Matej. Cannot fault the name. The other, much greater and equally important family I got is the family of my wife Ivana. Her parents, siblings and broader family represent some of the most important people in my life. Thanks to all their animals as well; I am eternally grateful for the best cats and the dog I could get. And to my Maca, a cat above all others; we miss you, little friend.

Thanks to all my relatives and family friends, especially to families Kuhar, Barišić, Mihić, Mrvičin, Hadžić, Abramović, Aberle, and aunt Anica. I do not think I could have had a better childhood (and adulthood).

Thanks to dad for passing me a bit of his creativity and making me the best tomahawk toy. And all the mushroom hunts, paintings and great memories; you live through them. I am grateful to the two people who have been with me always: my brother Martin and mother Jasminka. Mom, thanks for letting me choose my own paths while being there all the time. Brother, thanks for being the best friend and roommate ever. I am looking forward to the wedding and happy to gain a sister in Draženka.

Finally, and most of all, to my sun Ivana.

Matej Kuhar

Abstract

This thesis investigates the X-ray emission from solar flares and gives a comprehensive introduction to modern observational techniques in this energy range.

Solar flares are eruptive phenomena on the Sun that can release energies of up to 10^{32} erg (10^{25} J). They are caused by the release of energy stored in magnetic fields, which results in the acceleration of particles in the corona and plasma heating. Even though the most energetic flares catch most of the scientific interest due to their significance and potential (negative) impacts on man-made technologies and human lives, flares on the smallest scales might explain the coronal heating problem. It has been proposed that these flares, also called nanoflares, are responsible for heating the solar atmosphere from thousands of degrees on its surface to millions of degrees in the corona. If nanoflares are indeed just small versions of regular flares, their X-ray spectra should reveal signs of accelerating and heating processes present in all flares, resulting from the release of magnetic energy in the corona. Chapter 1 gives an overview of the coronal heating problem, nature of solar flares and their contribution to solar heating, as well as the importance of solar X-ray observations.

The part of the thesis about observational techniques discusses two main approaches in modern X-ray observations: indirect methods and focusing optics. Indirect methods reconstruct the incoming signal from either temporal or spatial modulations of incoming X-ray flux, caused by pairs of X-ray opaque grids that are placed in front of the detectors. From the observed modulation, Fourier components (visibilities) of the source can be derived. By using data from multiple grid pairs with different geometrical properties, one can gather enough visibilities for image reconstruction. In order to use this approach efficiently, geometrical properties of grids have to be determined precisely. A method of extracting this information from the X-ray and optical data gathered at the Paul Scherrer Institute (PSI, Switzerland) is described in Chapter 2. This method has been successfully used to infer the properties of grids in the *Spectrometer/Telescope for Imaging X-rays (STIX)*, one of the ten instruments to be launched on-board *Solar Orbiter* mission in 2020. In recent times, technological improvements have led to the possibility of using focusing optics in new-generation X-ray telescopes. Focusing optics has been used in the *Nuclear Spectroscopic Telescope Array (NuSTAR)*, and it has many advantages compared to indirect methods, such as lower background rates and better dynamic range (leading to much higher sensitivity).

The analyzed X-ray data come from two telescopes: the *Reuven Ramaty High*

Energy Solar Spectroscopic Imager (RHESSI) and *NuSTAR*. Because sensitivities of the two instruments are largely different, the analyzed flares span 8 orders of magnitude in soft X-ray flux and include events of all scales.

- *RHESSI* data have been used to study the correlation of hard X-ray and white light (optical continuum) emission in 43 large solar flares occurring between 2011 and 2014 (Chapter 3). Both emissions come from the chromosphere, where the accelerated electrons thermalize by collisions and heat the chromospheric plasma. X-ray emission is directly produced in this process via bremsstrahlung, while the white light emission, observed with the Helioseismic and Magnetic Imager (HMI), describes the chromospheric response to the heating. A good correlation between the two types of radiation was found in time, space and intensity, with the best correlation found for 50 keV electrons, indicating the WL emission is mostly produced by electrons around this energy.
- *NuSTAR* data, on the other hand, have been used to study faint, late phase emission from a solar flare 24 hours after its occurrence (Chapter 4). The X-ray emission was observed very high in the corona and the X-ray source was found to have the temperature of ~ 4 MK. This implies that flare loops, heated to \sim MK temperatures, still existed at the time of observations. The explanation lies in magnetic energy releases continuing long after the main phase of the flare, releasing an energy estimated to be an order of magnitude larger than the energy released just during the flare peak.
- In Chapter 5, *NuSTAR* observations of three flares in the quiet Sun, during two solar-dedicated campaigns in 2016 and 2017, are described. The importance of these observations lies in the fact that these flares are energetically between usual flares, observed in active regions, and nanoflares, which should occupy the whole solar disk. X-ray imaging spectroscopy was performed on quiet Sun flares for the first time and revealed temperatures in the range 3.1 – 4.2 MK, an order of magnitude lower than temperatures present in regular flares.

Possible future studies and collaborations are discussed in Chapter 6. Special emphasis is given to the simultaneous *NuSTAR* observations with the Atacama Large Millimeter/submillimeter Array (ALMA), as they can provide the full picture of flare energization in both the chromosphere and the corona. In the context of X-ray observations, NASA team at the Goddard Space Flight Centre, in collaboration with various other institutes, proposed a next-generation solar-dedicated focusing optics X-ray telescope, called the *Focusing Optics X-ray Solar Imager (FOXSI)*, as a NASA Small Explorer Mission (SMEX). As the whole fleet of instruments is currently under development, the next decade(s) will be surely filled with interesting new discoveries about our closest star.

Zusammenfassung

Diese Dissertation befasst sich mit Sonneneruptionen sowie ihrer Röntgenemissionen und gibt eine umfassende Einführung in moderne Beobachtungstechniken im Röntgenbereich.

Sonneneruptionen sind eruptive Phänomene der Sonne, die Energien von bis zu 10^{32} erg (10^{25} J) freisetzen können. Sonneneruptionen entstehen durch die Freisetzung von magnetischer Energie und bewirken Teilchenbeschleunigung und Plasmaheizung. Obwohl die grössten Sonneneruptionen auf Grund ihrer Wichtigkeit und ihrer möglichen (negativen) Auswirkungen auf Technologien und Menschenleben am meisten beachtet werden, sind die kleinsten Sonneneruptionen wahrscheinlich für die Heizung der Korona verantwortlich. Es wird spekuliert, dass die grosse Anzahl der kleinsten Sonneneruptionen, oder *nanoflares*, für die Heizung der Sonnenatmosphäre von \sim kK in der Photosphäre zu \sim MK in der Korona verantwortlich sind. Wenn nanoflares tatsächlich nur kleinere Versionen von regulären Eruptionen wären, sollten ihre Spektren im Röntgenlicht die gleichen Anzeichen der Beschleunigungs- und Heizungsprozesse wie bei regulären Eruptionen zeigen. Kapitel 1 gibt eine Einführung in die Natur der Sonneneruptionen und ihren Beitrag zur Koronaheizung, und diskutiert auch die Wichtigkeit von Röntgenbeobachtungen und den Parametern welche man mittels dieser Beobachtungen messen kann.

Der Abschnitt über Röntgenbeobachtungen diskutiert zwei verschiedene Zugänge in modernen Röntgenbeobachtungen: indirekte Abbildung und die abbildende Optik. Indirekte Methoden rekonstruieren das ankommende Signal aus zeitlichen oder örtlichen Modulationen der einfallenden Röntgenstrahlung, die durch ein Paar von (fast) gleichen Gittern erzeugt werden. Aus der beobachteten Modulation können Fourier-Komponenten (Sichtbarkeiten) des Bildes abgeleitet werden. Mit der Kombination von Daten aus mehreren Gitterpaaren mit unterschiedlichen geometrischen Eigenschaften kann man genug Fourier Komponenten sammeln und ein Bild der Sonneneruption konstruieren. Um das zu erreichen, müssen die geometrische Merkmale der Gitterpaare mittels Röntgen und optischen Daten genau ausgemessen werden. Kapitel 2 beschreibt die Methoden, welche erfolgreich verwendet wurden, um die Eigenschaften von Gittern in *Spectrometer/Telescope for Imaging X-rays (STIX)*, eines der zehn Instrumente, welche im Jahr 2020 an Bord der Mission Solar Orbiter fliegen werden, zu vermessen. Technologische Entwicklungen in den letzten Jahren haben die Anwendung abbildender Optik im Röntgenlicht ermöglicht. Die abbildende Optik

wird in *Nuclear Spectroscopic Telescope Array (NuSTAR)* benutzt und bietet viele Vorteile gegenüber den indirekten Methoden, wie niedrigere Hintergrundraten und einen grösseren Kontrastumfang in den erzeugten Bildern.

Die wissenschaftliche Datenauswertungen, welche in dieser Doktorarbeit dargelegt werden, kommen von zwei Röntgenteleskopen: *Reuven Ramaty High Energy Solar Spectroscopic Imager (RHESSI)* und *NuSTAR*. Die unterschiedlichen Empfindlichkeiten der beiden Instrumente machen es möglich, Sonneneruptionen über 8 Grössenordnungen in der Röntgenstrahlung zu untersuchen.

- Mit *RHESSI* Daten wurde die Beziehung zwischen optischer Strahlung und Emissionen im Röntgenbereich in 43 grossen Sonneneruptionen zwischen den Jahren 2011 und 2014 untersucht (Kapitel 3). Beide Emissionen werden durch den Prozess der Thermalisierung von beschleunigten Elektronen und ihre Wechselwirkung mit dem Plasma in der Chromosphäre produziert. Röntgenemission wird direkt in diesem Prozess durch Bremsstrahlung produziert, während die optische Strahlung durch die Aufheizung der Chromosphäre entsteht. Einen engen Zusammenhang zwischen den zwei Emissionstypen wurde in der Zeit, im Raum und in der Intensität gefunden. Die beste Korrelation liefern Elektronen mit der Energie von 50 keV. Dies zeigt, dass die Elektronen mit dieser Energie für die Aufheizung verantwortlich sind.
- *NuSTAR* Daten wurden benutzt, um schwache Emissionen, die 24 Stunden nach der Hauptphase der Sonneneruption noch sichtbar sind, zu untersuchen (Kapitel 4). Die Röntgenemission kommt sehr hoch aus der Korona und beinhaltet immer noch geheiztes Plasma von 4 MK. Das bedeutet, dass die Energiefreisetzung selbst nach einem Tag noch nicht abgeschlossen ist. Die totale freigesetzte Energie ist deshalb eine Grössenordnung höher als die Energie, welche während der Hauptphase der Sonneneruption abgegeben wird.
- Im Kapitel 5 werden *NuSTAR* Beobachtungen von 3 Sonneneruptionen in der ruhigen Sonne beschrieben. Diese kleinsten Ereignisse sind wichtig, weil die beobachteten Sonneneruptionen Energien genau zwischen regulären Eruptionen aus Aktivregionen und nanoflares, die die ganze Sonnendisk bedecken sollten, beinhalten. *NuSTAR* erlaubt uns zum ersten Mal, Röntgenspektroskopie für diese kleinsten Eruptionen durchzuführen. Die Temperaturen von diesen Eruptionen liegen zwischen 3.2 und 4.1 MK, eine Grössenordnung tiefer als in regulären Eruptionen.

Weiterführende Studien und Zusammenarbeiten werden im Kapitel 6 diskutiert. Von besonderem Interesse sind gleichzeitige Beobachtungen mit *NuSTAR* und Atacama Large Millimeter/submillimeter Array (ALMA), welche komplementäre Informationen über die Energie der Eruption in der Korona und

der Chromosphäre liefern. Die wichtigste neue Mission für die solaren Röntgenbeobachtungen ist *Focusing Optics X-ray Solar Imager (FOXSI)*, das Röntgenteleskop der nächsten Generation, geplant als NASA Small Explorer Mission (SMEX) unter der Leitung eines Teams in Goddard Space Flight Center mit FHNW Beteiligung. Mit *FOXSI* und den vielen anderen Instrumenten in Entwicklung sind wir sicher, dass die nächsten Jahrzehnte viele neue interessante Entdeckungen über unseren nächsten Stern bringen werden.

Contents

| | |
|--|-----|
| Acknowledgments | v |
| Abstract | vii |
| Zusammenfassung | ix |
| 1. Introduction: Coronal heating problem, solar flares and hard X-rays . . | 1 |
| 1.1 Coronal heating | 1 |
| 1.2 Solar flares | 3 |
| 1.2.1 Solar cycle, active regions, solar flares, and their properties . | 3 |
| 1.2.2 Flare energy budget and partition | 10 |
| 1.2.3 Flare frequency distribution | 12 |
| 1.3 Why hard X-rays? | 13 |
| 1.3.1 Flare spectra | 13 |
| 1.3.2 Observables | 16 |
| 1.4 X-ray instruments | 21 |
| 1.4.1 <i>RHESSI</i> , <i>STIX</i> and <i>MiSolFa</i> | 21 |
| 1.4.2 <i>NuSTAR</i> and <i>FOXSI</i> : Towards focusing optics | 24 |
| 2. <i>STIX</i> imaging concepts and grids calibration | 29 |
| 2.1 <i>RHESSI</i> and <i>STIX</i> imaging systems | 29 |
| 2.1.1 Fourier transform | 29 |
| 2.1.2 <i>RHESSI</i> | 30 |
| 2.1.3 <i>STIX</i> | 33 |
| 2.2 <i>STIX</i> grids calibration | 36 |
| 2.2.1 Optical characterization | 39 |
| 2.2.2 X-ray characterization | 47 |
| 3. Correlation of hard X-ray and white light emission in solar flares . . . | 61 |
| 3.1 Introduction | 61 |
| 3.2 Observations | 63 |
| 3.2.1 Time profiles | 63 |
| 3.2.2 HXR imaging and WL flux derivation | 64 |
| 3.2.3 HXR spectral fitting | 65 |
| 3.3 Results | 65 |
| 3.3.1 The data analysis steps for two examples | 65 |
| 3.3.2 Relation between HXR and WL fluxes | 66 |

Contents

| | | |
|-----------|--|------------|
| 3.3.3 | The correlation between HXR energies and WL fluxes | 71 |
| 3.4 | Discussion and conclusions | 73 |
| 4. | Evidence of significant energy input in the late phase of a solar flare | 81 |
| 4.1 | Introduction | 82 |
| 4.2 | Observations | 83 |
| 4.3 | Analysis of the high coronal source | 87 |
| 4.3.1 | Spectral fitting | 87 |
| 4.3.2 | Comparison of <i>NuSTAR</i> to <i>SDO/AIA</i> | 89 |
| 4.3.3 | Comparison of <i>NuSTAR</i> to <i>FOXSI</i> | 92 |
| 4.4 | Discussion and conclusions | 93 |
| 5. | <i>NuSTAR</i> detection of X-ray heating events in the quiet Sun | 97 |
| 5.1 | Introduction | 98 |
| 5.2 | Observations | 100 |
| 5.2.1 | Time evolution | 100 |
| 5.2.2 | Flare locations and morphology | 101 |
| 5.3 | Data Analysis | 103 |
| 5.3.1 | Spectra | 103 |
| 5.3.2 | Thermal energy content | 104 |
| 5.3.3 | Nonthermal emission | 104 |
| 5.4 | Discussion and conclusions | 106 |
| 6. | Summary and outlook | 111 |
| 6.1 | Summary of presented and possible follow-up studies | 111 |
| 6.1.1 | <i>STIX</i> grids calibration | 111 |
| 6.1.2 | Correlation of HXR and WL emission | 112 |
| 6.1.3 | Long-lasting emission in the gradual phase | 113 |
| 6.1.4 | X-ray emission from flares in the quiet Sun | 114 |
| 6.2 | Simultaneous observations with ALMA and other instruments | 114 |
| 6.3 | What is next in solar physics? | 119 |
| 6.3.1 | Focusing optics in X-rays | 119 |
| 6.3.2 | Other wavelengths | 120 |
| 6.3.3 | Bright future | 121 |
| | Curriculum vitae | 123 |
| | Publications | 125 |

Chapter 1

Introduction: Coronal heating problem, solar flares and hard X-rays

In this chapter, the most important concepts and theories that are addressed in the thesis are introduced. The coronal heating problem, one of the most interesting but still unexplained phenomena in astrophysics, is discussed in Section 1.1. Two main theories that aim to explain this phenomenon are presented: wave and flare theory, with much more emphasis given to the latter. Basic properties of solar flares and their multiwavelength nature are described in Section 1.2. The progress in solar flare observations since their first detection by Carrington (1859) is also presented. A closer look into the total energy content of solar flares is given, together with their frequency distribution. Section 1.3 explains the importance of hard X-ray observations of solar flares, together with the observables one can obtain. Finally, a short introduction to current and planned X-ray instruments is given in Section 1.4.

1.1 Coronal heating

The Sun is the G-type star in the center of our Solar system, located some 150 million kilometers (1 astronomical unit, AU) from Earth. Its mass of 2×10^{30} kg forms conditions in the core that enable the process of hydrogen fusion to occur (Freedman & Kaufmann 2005). The net result of this process is the fusion of 4 hydrogen atoms into a helium atom, together with the release of energy (see Figure 1.1).

Since millions and millions of these reactions occur constantly in the solar core, huge amounts of energy are released. This energy heats the inner parts of the Sun and its atmosphere. If we would think of the solar core as a campfire, the temperature should monotonically decrease with distance to the center (the further away from the energy source we are, the colder it gets). This is indeed observed in the solar interior and its surface, the *photosphere*. However, the atmospheric layer above the photosphere, the *chromosphere*, shows a different temperature behaviour: a temperature minimum of 4100 K is observed at ~ 500 km above the surface (e.g., Avrett & Loeser 2008). At heights above the temperature minimum, the temperature increases gradually until ~ 2300 km above the surface, where a dramatic change is observed. There, the temperature increases

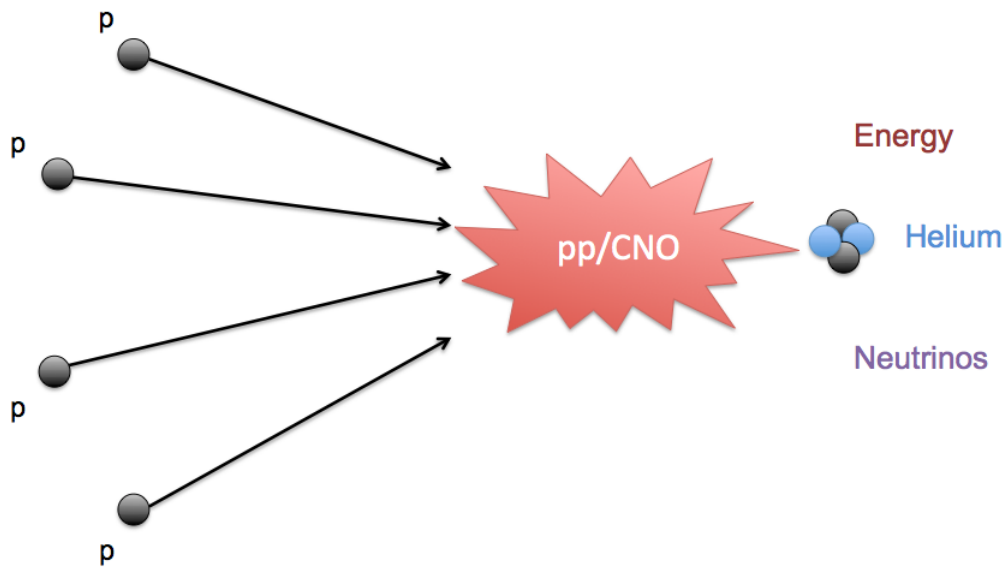


Figure 1.1: Fusion of hydrogen into helium. Depending on the temperature of a stellar core, proton-proton (pp) or carbon-nitrogen-oxygen (CNO) cycles occur. For the Sun and solar-type stars the pp cycle is dominant. The net result is the formation of a helium atom and released energy.

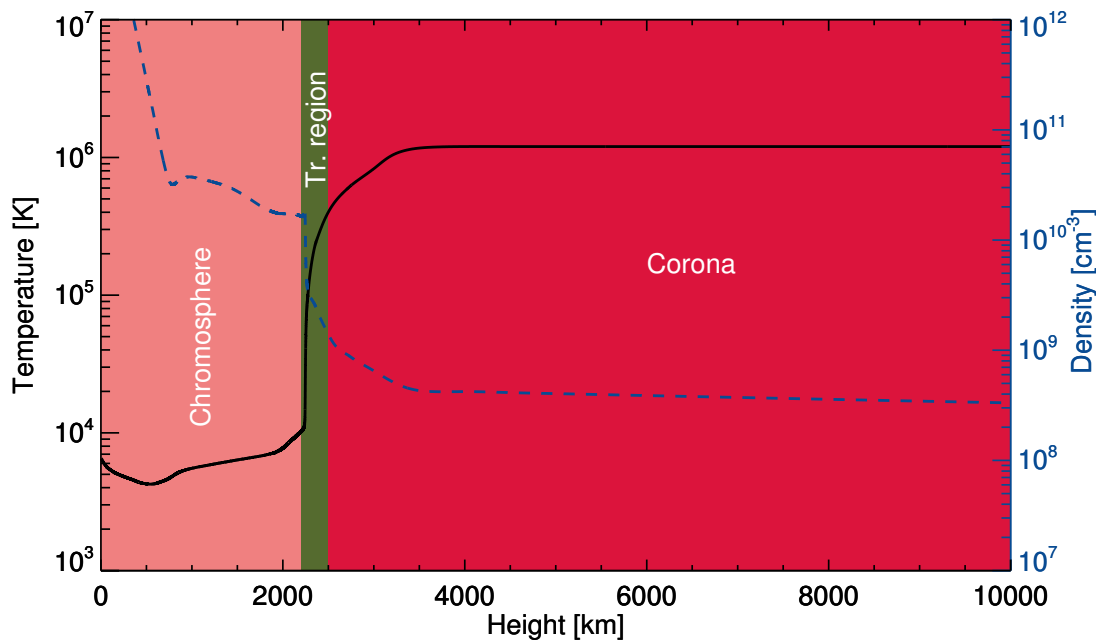


Figure 1.2: Temperature and density as a function of height in the (quiet) solar atmosphere. The chromosphere, the transition region and the corona are depicted with different colors. Data show the model of the solar atmosphere from Avrett & Loeser (2008).

abruptly in a thin layer called the *transition region* from $\sim 10\,000$ K to ~ 1 MK in the *corona*, the hottest and the least dense ($10^8 - 10^9$ cm $^{-3}$) layer of the solar atmosphere. The temperature and density profiles of a quiet Sun atmosphere as a function of height above the photosphere can be found in Figure 1.2. Images of the Sun with the Helioseismic and Magnetic Imager (HMI, Schou et al. 2012) and the Atmospheric Imaging Assembly (AIA, Lemen et al. 2012) on the *Solar Dynamics Observatory* (SDO, Pesnell et al. 2012) in wavelengths that probe the photosphere, the chromosphere and the corona can be found in Figure 1.3, showing their different nature. The unusual behavior of temperature in the solar atmosphere is termed the *coronal heating problem* (Klimchuk 2006) and it represents one of the long-lasting problems in astrophysics. While the mechanism(s) of energy conversion in the corona are not well understood, there is a general agreement that the source of energy for coronal heating lies in the magnetic fields which are stressed by motions in the photosphere and below (e.g., Klimchuk 2006, and references therein). Magnetic fields on the Sun are produced by motions of plasma (so called *hydromagnetic dynamo*) in the *convective zone* below the photosphere (e.g., Parker 1955).

Wave theories explain the coronal heating by waves which are formed in the photosphere and carry energy upwards. While their energy flux in the photosphere is enough to explain coronal radiative losses, the problem lies in the fact that the majority of waves formed this way dissipate in the chromosphere, before they even reach the corona. Of all wave types, Alfvén waves (oscillations of ions and the magnetic field) have the highest probability of reaching the corona (e.g., Cranmer & van Ballegoijen 2005). Their influence on coronal heating has, therefore, been studied in much detail (e.g., Tomczyk et al. 2007; McIntosh et al. 2011).

Flare theory explains the coronal heating problem through numerous tiny releases of magnetic energy which constantly heat the corona. This theory has been proposed by Parker (1988) in an attempt to explain the observed coronal radiative losses, and will be the focus of the remainder of this and some of the following chapters.

1.2 Solar flares

1.2.1 Solar cycle, active regions, solar flares, and their properties

The Sun experiences changes in activity in 11-year cycles. Periods of low activity are called *solar minimum*, while periods of high activity are termed *solar maximum*. Solar maxima are characterized by generally stronger magnetic fields, more sunspots and large numbers of explosive phenomena such as solar flares and coronal mass ejections (CMEs). These changes in activity are caused by the effects of the solar differential rotation on the magnetic fields formed in the convection zone. Because plasma near the equator rotates more rapidly than plasma near the poles, poloidal magnetic field lines get coiled up and produce flux tubes.

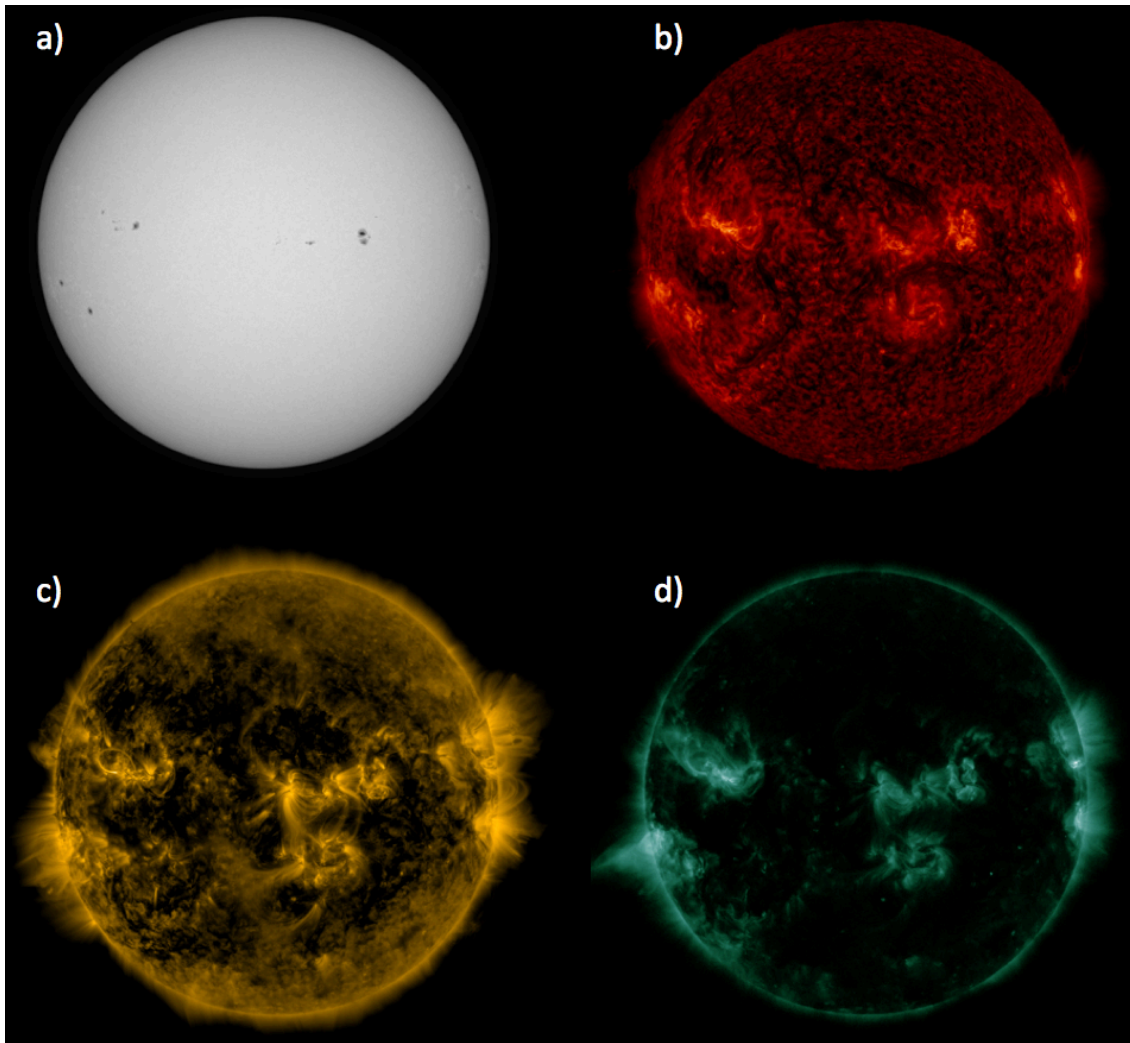


Figure 1.3: Multiple faces of the Sun. *a)* The HMI 6173 Å image reveals the solar photosphere. *b)* Chromosphere/transition region at temperatures of $\sim 50\,000$ K, as observed by the AIA 304 Å channel. *c)* The AIA 171 Å image of the Sun reveals cool features of ~ 0.7 MK in the solar corona. *d)* The AIA 94 Å image of the Sun, showing hot features of ~ 6 MK in the corona.

Due to the enhanced magnetic field strengths, pressure and density inside flux tubes are lower than in the surrounding medium, causing them to move upwards and create sunspots (Babcock 1961). Once the toroidal magnetic fields reach east-west direction, the activity is at maximum and with time, due to ongoing differential rotation, the flip of the magnetic field occurs. The magnetic activity on the surface slowly declines again and the magnetic field lines retrieve their longitudinal directions (but with reverse polarity). The process has to repeat once again to return to the initial state, which is why complete solar cycles last 22 years. This is presented schematically in Figure 1.4.

Sunspots are places of strong magnetic field concentration with average values in the 1000 – 1700 G range (Solanki & Schmidt 1993) and maximum field

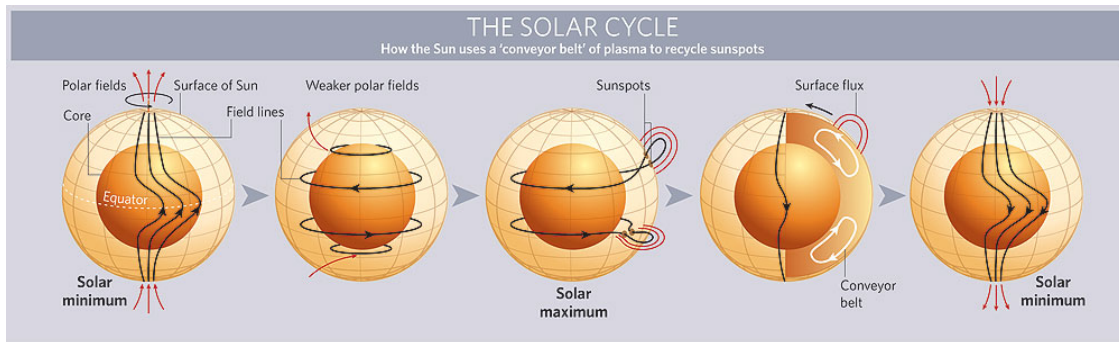


Figure 1.4: Differential rotation of the Sun leads to twisting of the magnetic fields, producing changes in the activity on the surface. Taken from http://www.timmytelescope.com/outreach-materials/board05/sun_pole-reversal.jpg.

strengths of up to $\sim 5000 - 6000$ G (Livingston et al. 2006). They are observed as dark spots (indicating temperatures below 5700 K of the surrounding medium) in the photosphere. This is caused by somewhat suppressed convection due to strong magnetic fields, which decreases the flow of energy and reduces the temperature. Examples of few sunspots can be seen in panel *a* of Figure 1.3. Individual sunspots have vastly different sizes and lifetimes, with the latter ranging anywhere from days to months (e.g., Solanki 2003). Their appearance at mid latitudes of $\sim 30^\circ$ indicates the increase of solar activity after solar minimum. As the activity increases, sunspots move towards lower latitudes until the solar activity reaches the maximum. As the activity fades again, they appear in fewer numbers and constantly closer to the equator. The new cycle begins with their appearance at higher latitudes, and the above process is repeated. This behaviour is also shown in the top panel of Figure 1.5. It is popularly called the *butterfly diagram* and its first version was mapped by Maunder (1904).

Bright structures in the extreme ultraviolet (EUV) and (hard) X-rays (HXRs) at coronal heights, which appear over sunspots observed in the photosphere, are called *active regions*. They can be clearly seen in panels *c* and *d* of Figure 1.3 as regions of higher intensity, temperature and density. Active regions are subject of great interest since they are associated with the strongest magnetic fields and most energetic of solar phenomena: *solar flares*. Flares are places of efficient particle acceleration and heating, resulting from the release of magnetic energy. Solar flares are observed across the whole electromagnetic spectrum, from radio waves to gamma-rays. Even though flare observations date back to the 19th century, many aspects of their nature are still not well-understood. Some of the most important unresolved questions include:

- How is magnetic energy released?
- Which particle acceleration mechanisms are involved?
- What is the total energy budget of flares?

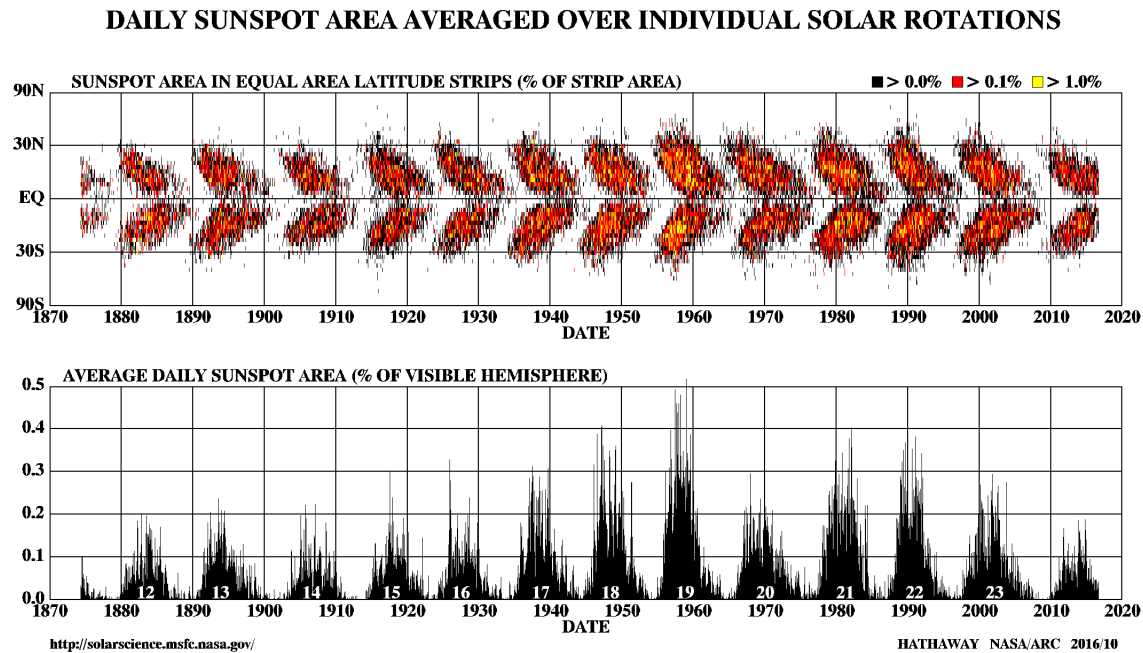


Figure 1.5: *Top:* Butterfly diagram of sunspots. *Bottom:* Changes in solar activity represented as the average daily sunspot area. Taken from <https://solarscience.msfc.nasa.gov/SunspotCycle.shtml>

- Is the majority of the energy budget/release in the corona or the chromosphere?
- How is the flare energy partitioned throughout the electromagnetic spectrum?
- How is optical emission created?
- What are the relevant transport effects of accelerated particles in solar flares?

In order to answer these questions completely and derive correct physical interpretations, it is of utmost importance to conduct multiwavelength observations of solar flares, as different physical aspects of solar flares manifest themselves in various parts of the electromagnetic spectrum. In that respect, much has changed since first flare observations by Carrington (1859). To emphasize this further, a comparison between the original Carrington’s observation of a flare on 1859 September 1 (sketched by hand) and modern-type observations with AIA, HMI and the *Reuven Ramaty High Energy Solar Spectroscopic Imager (RHESSI*, Lin et al. 2002) is provided in Figure 1.6, giving a view on optical, X-ray and EUV emission from the same flare on 2012 July 19.

The ‘standard’ model of solar flares is schematically presented in Figure 1.7 (Benz 2017). During the process of magnetic energy release, magnetic field lines reconnect and rearrange from the complex high energy state to the simpler low

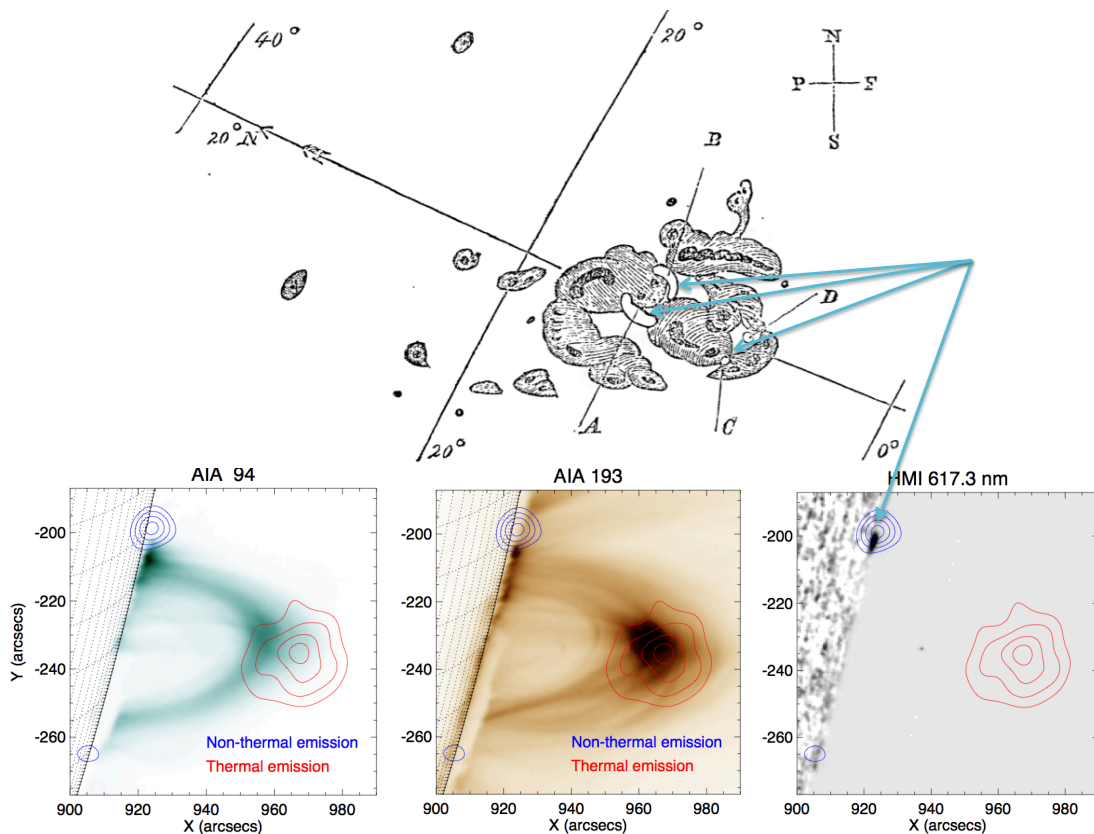


Figure 1.6: *Top:* Carrington (1859) map of a solar flare on 1859 September 1. *Bottom:* Images of the flare 2012-07-19 (M7.7) in the EUV, X-ray and optical. The flare emission in the optical continuum of both events, originating in the chromosphere, is highlighted with arrows, relating the sets. In the more recent observations, only one nonthermal source is visible due to the flare location just at the limb (the other source is probably located just behind the limb). Blue contours show nonthermal emission in X-rays, caused by flare accelerated electrons, while the red contours show the hottest part of the thermal flare loop.

energy state, causing particle (electrons and ions) acceleration in the corona and plasma heating. The accelerated particles precipitate along the closed magnetic field lines to the lower layers of the solar atmosphere and interact with the ambient plasma along the way, or escape directly from the acceleration site to the interplanetary space along the open field lines. As the densities in the corona are generally low, most of the collisional energy loss occurs in the chromosphere, in the sites called *footpoints*. This energy is emitted in all parts of the electromagnetic spectrum, from gamma-rays and X-rays to radio wavelengths. In the following sections we will come back to the problem of extracting physical parameters from this radiation. The emission from accelerated particles is usually referred to as *nonthermal*, while the emission from heated plasma is termed *thermal*.

The acceleration site is thought to be located above flare loops. However, because nonthermal emission is produced by bremsstrahlung, whose effectiveness positively correlates with density, HXR emission from the chromosphere is much

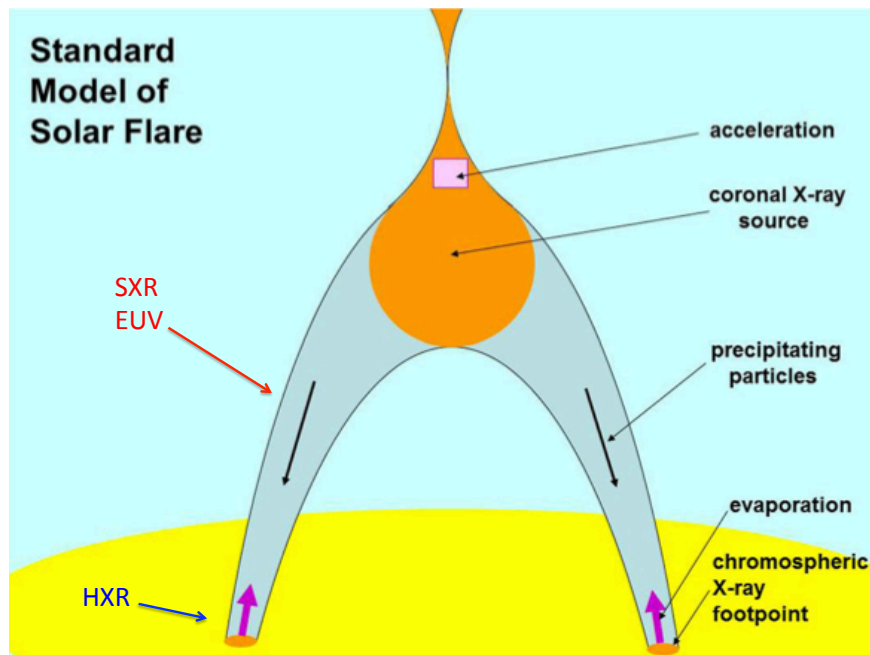


Figure 1.7: Schematic view of solar flares. Taken from Benz (2017).

stronger than from the corona. Therefore, nonthermal bremsstrahlung emission from the acceleration site has been observed directly only in few extraordinary events (Masuda et al. 1994; Krucker et al. 2010), due to limitations of present instruments and intensity of the signal. The event on 1992 January 13 shown in Figure 1.8 has had such a profound impact on the solar physics community that it is termed *Masuda flare*. The best case for observations of the acceleration site is when the flare footpoints are occulted, so the whole dynamic range is reserved for the coronal source. The importance of these observations cannot be overestimated, as they provide the only opportunity for direct observations of the acceleration site and might provide key insights into understanding fundamental processes of particle acceleration in astrophysical plasmas.

As a result of the particle acceleration, large amounts of energy are transferred to the chromosphere. The chromospheric material experiences a process called *chromospheric evaporation*, in which it is abruptly heated due to this energy deposition and expands to higher altitudes along the closed magnetic field lines. Here we note that the term ‘evaporation’ is a historical misnomer and should not be taken in the classical sense as the change of state. The only process that takes place is the abrupt heating of the chromospheric plasma, which increases its temperature in very short timescales, making it unstable and leading to expansion. With this in mind, perhaps the better term would be *chromospheric ablation*, more accurately describing the process. The structures of expanding heated plasma with temperatures usually above 10 MK are called *flare loops*. An important parameter for the structure of flare loops is plasma β , defined as the ratio of the plasma kinetic pressure to the magnetic pressure. As particles in flare loops follow the field lines, the magnetic pressure is stronger than the plasma pressure,

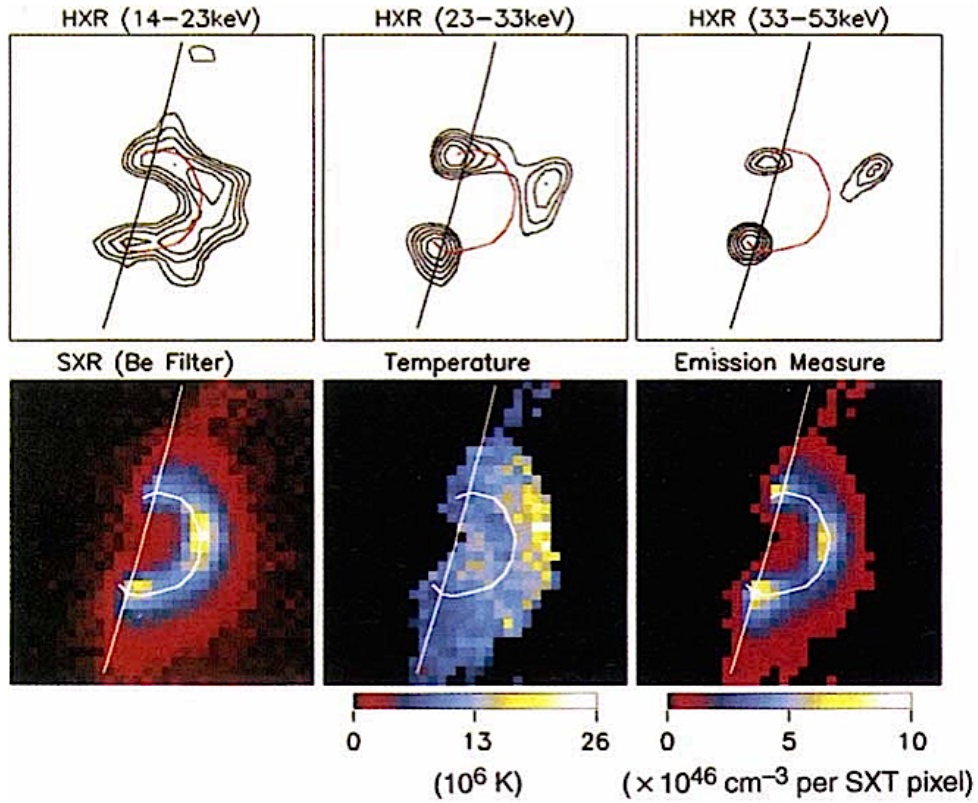


Figure 1.8: Observations of the Masuda flare, representing the first direct X-ray imaging of the acceleration site in a solar flare. Taken from Masuda et al. (1994).

i.e. $\beta < 1$. If plasma would gain additional kinetic energy (through heating), flare loops could become unstable ($\beta > 1$) and crumble. Therefore, their very existence implies conditions in which the magnetic field dominates over the kinetic energy of the heated plasma. Flare loops are best observed in the lower range of X-ray energies and the EUV, also shown in Figure 1.6. Here we also point to the often interchangeable usage of terms SXR/thermal and HXR/nonthermal emission. Depending on the flare, nonthermal emission from accelerated electrons can extend to energies above 100 keV or dominate at even very low energies of ~ 10 keV and less (Sui et al. 2006; Hannah et al. 2008b). Similarly, thermal emission from flare loops can be observed anywhere from the sub-keV range to energies above 30 keV (e.g., Caspi et al. 2014). Even though nonthermal emission can extend into the SXR range and vice versa, the term HXR emission in publications usually points to the emission by accelerated electrons, and the SXR emission points to the thermal emission by hot plasma in flare loops.

The thermal emission shows a time delay with respect to the peak nonthermal emission, termed the *Neupert effect* (Neupert 1968). Even though it was first observed in microwaves, it is usually used to correlate the SXR and HXR fluxes with the following formula:

$$\frac{dF_{\text{SXR}}}{dt} \propto F_{\text{HXR}}. \quad (1.1)$$

The derivative of the SXR flux is proportional to the HXR flux or, equivalent, the time-integrated HXR flux is proportional to the SXR flux. The temporal evolution of the SXR flux in the *Geostationary Operational Environmental Satellite (GOES)* 1 – 8 Å channel and the 50 – 100 keV HXR flux in Figure 1.9 shows a nice example of the Neupert effect for the flare SOL2011-09-06 (X2.1). The derivative of the SXR flux correlates well with the observed HXR flux. The Neupert effect and the formula above explains the fact that it takes some time (typically of the order of a minute, but can be even above 10 minutes, e.g. Dennis & Zarro 1993) for the heated plasma to reach high temperatures and start emitting in this range. Therefore, the thermal emission can be understood as a response to the heating by the accelerated electron population. This simplified picture, however, cannot explain all observations, and it is generally more valid for events with pronounced non-thermal emission (Veronig et al. 2002). Even though it was discovered in solar flares, Neupert effect is a more universal phenomenon, observed in stellar flares as well (e.g., Hawley et al. 1995).

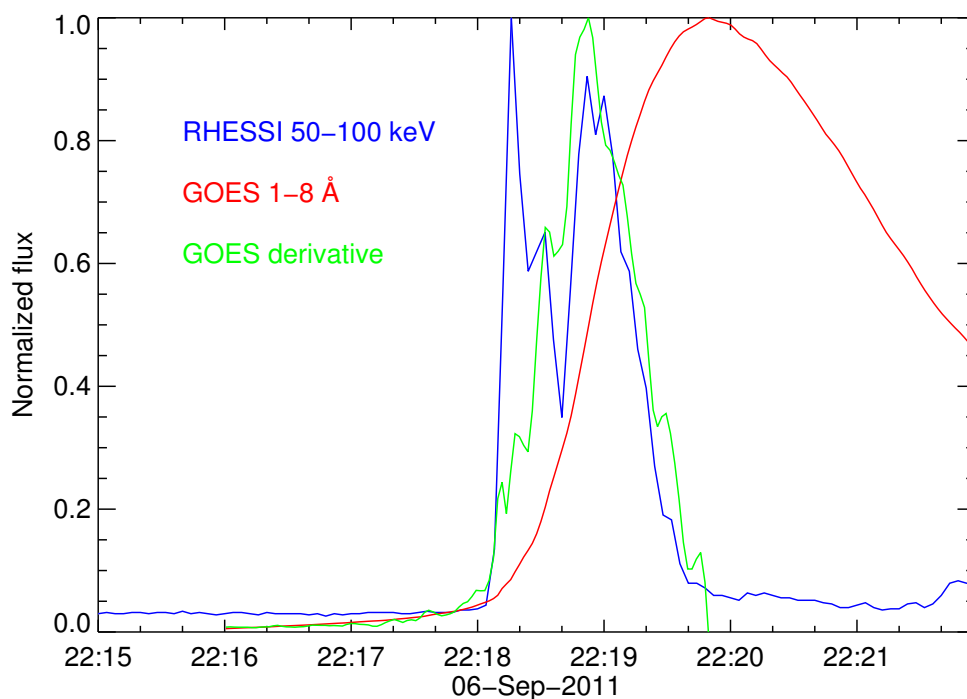


Figure 1.9: Time evolution of *RHESSI* 50 – 100 keV nonthermal emission and *GOES* 1 – 8 Å SXR emission. The derivative of *GOES* flux is overlaid in green, showing the Neupert effect. Even though there is a good agreement between the observed HXR flux and the SXR derivative, there is a discrepancy during the first nonthermal peak.

1.2.2 Flare energy budget and partition

In order to estimate the contribution of solar flares to coronal heating, it is crucial to understand how particles in solar flares are accelerated, what the total energy

budget of a solar flare is and how it can be estimated from the observables. The overall energy budget of flares is one of the key parameters for their classification, together with their peak soft X-ray flux as observed by *GOES*. The *GOES* classification contains the following logarithmic classes: A, B, C, M and X, where A class represents flares with lowest SXR fluxes (10^{-8} Wm^{-2}) and X with highest (10^{-4} Wm^{-2}). However, since solar flares are extremely complicated phenomena, estimating the total energy of a solar flare is not straightforward. Flares emit radiation in all wavelength ranges and across all layers of the solar atmosphere: optical continuum emission comes from the photosphere and the chromosphere, SXR emission from flare loops extends high into the solar corona, nonthermal X-ray radiation comes from interactions of accelerated electrons with chromospheric plasma, radio emission can be explained by synchrotron radiation in cases of strong magnetic fields, etc. Even though often neglected as they are much more difficult to observe, accelerated ions can carry energy similar to the one in the accelerated electrons (e.g., Lin et al. 2003). Furthermore, particles in coronal mass ejections (CMEs) carry additional kinetic and gravitational energy, also resulting from the magnetic energy release. All of these emissions contribute to the overall energy budget and one has to be careful when using data from different wavelength ranges, as it can lead to double-counting. Usually, the thermal peak energy of a solar flare is a good approximation of the total energy budget (or at least a good lower limit), since this emission represents the response of the chromosphere to the energy release and heating. In all cases, the total energy stored in magnetic fields before the flare should be able to explain all types of the observed emission.

Emslie et al. (2012) used observations of 38 large solar flares in order to estimate the energy partition in solar flares between the above mentioned energy contributions. Their main conclusions are:

1. The available energy in magnetic fields is sufficient to power all flare emissions, as well as energy carried in accelerated particles and the CME.
2. Late phase emissions in solar flares are important, as the total radiated energy by SXR plasma exceeds its value at flare peak by a factor of 2.8. Long-lasting SXR and EUV emission in later stages of solar flare evolution was also found in other studies (Woods et al. 2011; Woods 2014; West & Seaton 2015) and will be analyzed further in Chapter 4.
3. The energy in accelerated particles is sufficient to explain all radiated losses. In a more recent article, Warmuth & Mann (2016) find the opposite in some flares from their sample, in particular the less energetic ones. Therefore, they propose a modified model of solar flares, requiring an additional non-beam heating mechanism which provides the rest of the needed energy.
4. Energies carried by accelerated electrons and ions are comparable and they are in the range $10^{30} - 10^{32}$ erg ($10^{23} - 10^{25}$ J) for this sample.

1.2.3 Flare frequency distribution

In order to estimate the contribution of solar flares to coronal heating, we have to estimate their occurrence as a function of their total energy. The total contribution of all flares to the coronal heating is equal to the sum over individual events:

$$C_f = \int_E f(E) \cdot E \cdot dE, \quad (1.2)$$

where C_f is the total flare contribution and $f(E)$ is their frequency distribution depending on the total flare energy E . The observations show that the flare frequency distribution $f(E)$ is well described by a power-law:

$$f(E) = A \cdot E^{-\beta}, \quad (1.3)$$

where A is the normalization factor and β is the power-law index. It has been pointed out (e.g., Hudson 1991) that the critical value of β is 2. For $\beta < 2$, large flares would dominate the total contribution, while for $\beta > 2$ small-scale events would be the dominant contributor of energy. Since the largest solar flares are too rare and too localized to explain steady coronal temperatures, which remain in the \sim MK range even during solar minima, it has been proposed that the events on the smallest scales might be responsible for coronal heating, due to their large numbers. Parker (1988) introduced the term *nanoflares* for these basic magnetic energy releases, with energies estimated to be of the order of 10^{24} erg or less. The caveat is that nanoflares would not originate exclusively in active regions, but would make an *ensemble* across the whole solar disk and make the hot X-ray corona. Furthermore, in this scenario, microflares (intermediate-energetic events between nanoflares and ordinary flares), ordinary flares and active regions would just be superpositions of nanoflares. In order to test this picture, the heliophysics community has put a lot of emphasis on theoretical and observational studies of small-scale events and their role in coronal heating. Figure 1.10 shows a compilation of flare frequency distributions from various EUV, SXR and HXR studies (Shimizu 1995; Parnell & Jupp 2000; Aschwanden et al. 2000; Benz & Krucker 2002; Hannah et al. 2008a). The presented studies are inconclusive regarding the power-law index, with values fluctuating around 2, depending on the assumptions made how to group and classify individual flares (for discussion see Benz & Krucker 2002).

The distributions in Figure 1.10 can be divided in two parts. On the left are distributions of quiet Sun (QS) flares obtained from EUV and SXR observations. Observations of flares in the QS (occurring outside active regions) are important as they represent an intermediate step between ordinary active region flares and nanoflares proposed by Parker. On the right, (H)XR distributions of microflares in active regions are presented. Here, a complete spectroscopic analysis of observed events could be performed, and the studies give information on their basic properties like emission measures (EMs), temperatures and nonthermal fluxes. In Chapter 5, HXR spectroscopy on events below the detection limits of instruments used for the right part of the image, in the energy range $10^{26} - 10^{27}$ ergs, will be

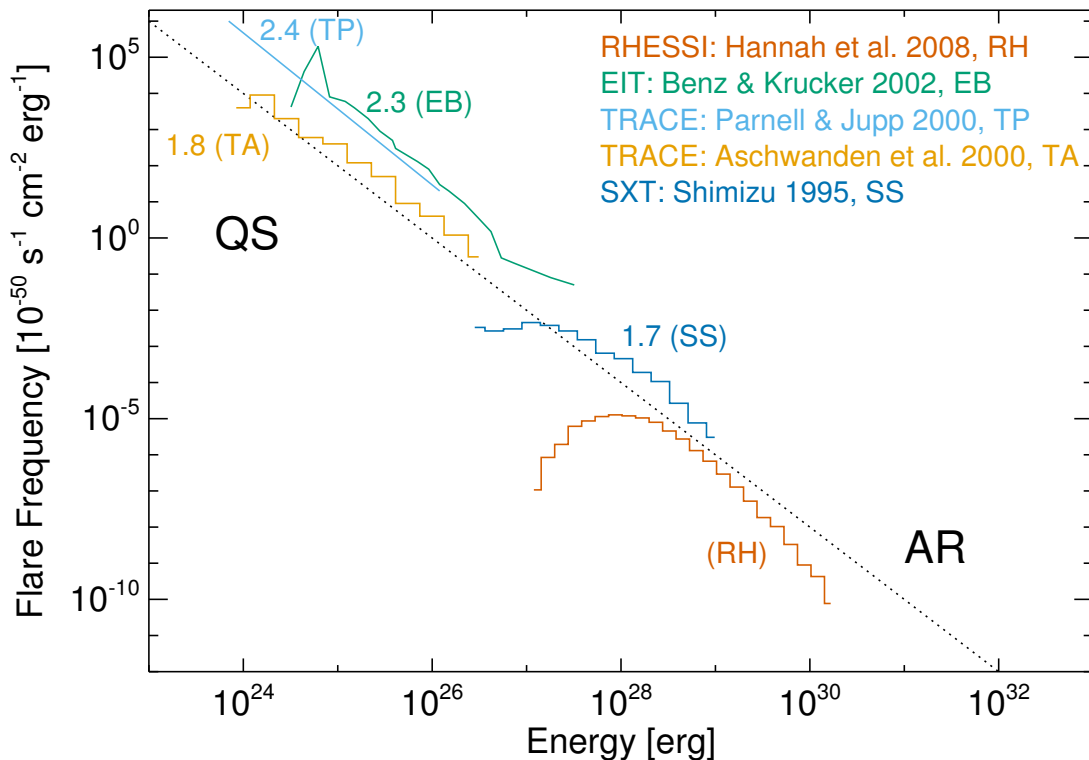


Figure 1.10: Flare frequency distribution as a function of energy. Active region microflares observed in HXRs can be found on the right, while less energetic flares (outside of active regions) observed in SXR and EUV are on the left. Taken from Hannah et al. (2008a) and adapted.

performed. Obtaining spectra in this range is important as this information can be used to scale flare properties down to even lower energies. Temperature, emission measure and density estimates directly from X-ray spectra of events occurring in the QS will be obtained for the first time. The upper limits on their possible nonthermal emission will also be discussed in the context of coronal heating. Direct measurement of nonthermal emission in a QS flare spectrum would represent one of the most important proofs of the Parker's theory of coronal heating.

1.3 Why hard X-rays?

1.3.1 Flare spectra

After considering physical interpretations of flare phenomena, one could ask the question: 'Why are HXR observations of flares important for the understanding of their nature?' This section gives a comprehensive answer to this question, both from a theoretical and, more importantly for this work, an observational point of view.

In a solar flare, particles are accelerated abruptly from sub-keV energies to

tens of keV or even MeVs (e.g., Lin et al. 2003; Hurford et al. 2003). These particles carry a significant fraction of released magnetic energy and, therefore, information about acceleration mechanism(s). Observations of emission by accelerated particles provides the most direct insight into the currently unknown acceleration processes taking place in solar flares and other astrophysical plasma.

In order to understand the X-ray observations that will be presented later, it is important to understand which process(es) produce X-ray emission. As the electrons travel from the corona to the chromosphere, they interact with the ambient plasma and lose their energy. The most efficient energy loss process are Coulomb collisions with the ambient electrons. Because the ambient densities in the corona are rather low, electrons do not lose a lot of energy in this region. Hence, the corona represents a *thin target* for the electrons. In the first-order approximation, this is defined as the medium where energy losses are negligible. In the much denser chromosphere, on the other hand, electrons interact much more often with the ambient plasma. The chromosphere therefore acts as a *thick target* for the accelerated electrons, as they lose all their energy at these heights.

There are three possible mechanisms that could lead to the emission of X-ray photons in solar flares (e.g., Krucker et al. 2008):

1. **Inverse Compton scattering:** Occurs when a (high-energy) charged particle transfers part of its energy to a photon. In a solar case, this would imply interactions between relativistic electrons and SXR photons released during the flare. Studies have shown that this process would require large fluxes of relativistic electrons (e.g., Acton 1964), which is not favored by observations. MacKinnon & Mallik (2010) and Chen & Bastian (2012) argue that inverse Compton scattering might explain observations of few (extreme) high coronal sources, where densities might be too low for significant bremsstrahlung emission. However, there is a general conclusion that inverse Compton scattering is a negligible contributor to the observed X-ray emission in most cases, if not all.
2. **Gyrosynchrotron radiation:** Photons are emitted as a result of the interaction between charged particles and the electromagnetic field. This radiation can also be neglected in the X-ray domain during solar flares as it requires too strong magnetic fields, not supported by observations. It is, however, important in the microwave and radio range (e.g., Bastian et al. 1998).
3. **Free-free bremsstrahlung:** This is the dominant radiation mechanism in the X-ray range during solar flares, produced when a free electron passes by an ion (typically a proton), interacts with its electric field, and emits an X-ray photon as a result. It is schematically shown in Figure 1.11. Even though this radiation represents only a small fraction (in the $10^{-5} - 10^{-4}$ range, e.g., Lin & Hudson 1971; Galloway et al. 2010) of total energy losses (the main being Coulomb collisions with ambient electrons), it is a crucial diagnostic tool to understand acceleration mechanisms in solar flares.

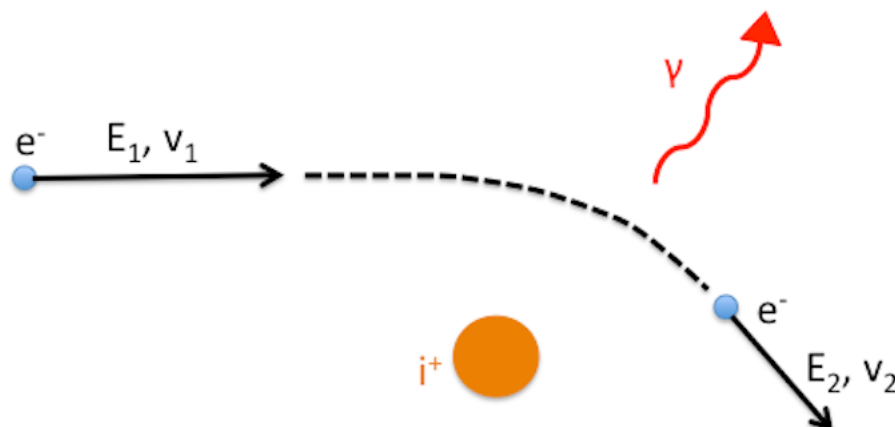


Figure 1.11: Free-free bremsstrahlung radiation is produced when a free electron passes by a nucleus or a single proton. The electron loses a part of its energy in the electric field of an ion, which leads to its deceleration and emission of an X-ray photon.

The observed photon flux in the X-ray range observed at Earth can be expressed with the following formula (Brown 1971):

$$I_{ph} = \frac{1}{4\pi R^2} \int_V \int_E Q_e(E) v(E) F_e(E, \mathbf{x}) F_p(\mathbf{x}) dE d^3\mathbf{x}, \quad [\text{photons cm}^{-2} \text{s}^{-1} \text{keV}^{-1}] \quad (1.4)$$

where R is the Sun–Earth distance, $Q_e(E)$ the electron-proton nonrelativistic cross-section, $v(E)$ the velocity of electrons with energy E , $F_e(E, \mathbf{x})$ the accelerated electron distribution and $F_p(\mathbf{x})$ the ambient proton distribution. In fact, what an instrument observes is the spectrum measured by the detector(s) in an X-ray instrument, usually in units of [counts s^{-1}]. Using the information about the detector effective area and energy binning, this can be transformed to [counts $\text{s}^{-1} \text{cm}^{-2} \text{keV}^{-1}$]. Finally, the count spectrum divided by the detector response gives the physical photon flux given by Equation 1.4. This is also shown in Figure 1.12, where we show both count and photon spectra of the same flare.

The crucial information hidden in the X-ray observations is the link between the observed photon flux and the injected electron distribution in the chromosphere producing the radiation:

$$I_{ph} \sim F_e(E, \mathbf{x}). \quad (1.5)$$

Typically, the observed photon spectrum in the ~ 50 keV range can be described by a power-law:

$$I_{ph} = A_{ph} \cdot E^{-\gamma}. \quad [\text{photons cm}^{-2} \text{s}^{-1} \text{keV}^{-1}] \quad (1.6)$$

Brown (1971) showed that the corresponding power-law distribution of electrons $F_e = A_e \cdot E^{-\delta}$ [electrons $\text{s}^{-1} \text{keV}^{-1}$] can explain this behaviour. For the thick-

target assumption, the relationships between the normalization constants and indices between the observed photon and the corresponding electron distributions are given by the following formulae (e.g., Saint-Hilaire & Benz 2005):

$$A_{ph} = A_e \cdot \frac{\overline{Z^2} \kappa_{BH} B(\delta - 2, 1/2)}{4\pi R^2 K(\delta - 1)(\delta - 2)}, \quad (1.7)$$

$$\gamma_{thick} = \delta - 1, \quad (1.8)$$

where $\overline{Z^2}$ is the average atomic number of the surrounding plasma, $\kappa_{BH} = 7.9 \times 10^{-25} \text{ cm}^2 \text{ keV}$ and $K = 2.6 \times 10^{-18} \text{ cm}^2 \text{ keV}^{-2}$ constants, B the beta function, γ_{thick} the photon power-law index and δ the electron power-law index. Therefore, by measuring the photon spectrum, one can obtain the electron distribution that produced it.

A typical *RHESSI* X-ray spectrum is shown in Figure 1.12, with the event SOL2011-09-06 (X2.1) taken as an example. The observed X-ray emission in the keV energy range is produced either by hot plasma in flare loops (lower energies) or by accelerated electrons hitting the chromosphere (higher energies). These contributions are modelled with a Maxwellian distribution of plasma and a nonthermal power-law tail, and depicted in green and blue in Figure 1.12, respectively. The fitting was performed in the Object Spectral Executive (OSPEX) package¹, the most often tool used for the analysis of *RHESSI* spectra. In order to explain the emission across all energies, a combined fit of a thermal core (Maxwellian distribution) and a broken power-law is usually fitted to solar spectra, shown in red. In some flares, as discussed already, also emission from accelerated ions can be observed at even higher energies, but this is outside the scope of the present work.

1.3.2 Observables

What are the observables one can obtain from flare spectra? That, of course, depends on the function used for spectral fitting. Here, we will discuss the observables from the thermal+thick (power-law) function discussed in the previous section.

The radiation at low X-ray energies is produced by thermalized plasma following the Maxwellian distribution. Its photon spectrum can be described by the following formula:

$$I_{ph}(T) \sim EM \cdot g(T, E), \quad (1.9)$$

where $g(T, E)$ is the function containing the Maxwellian distribution and EM is the emission measure. Therefore, the thermal fit provides two main observables for the (multi)thermal plasma:

1. **Temperature:** spectral fitting provides an estimate of the plasma temperature.

¹ <https://hesperia.gsfc.nasa.gov/ssw/packages/spex/doc/>

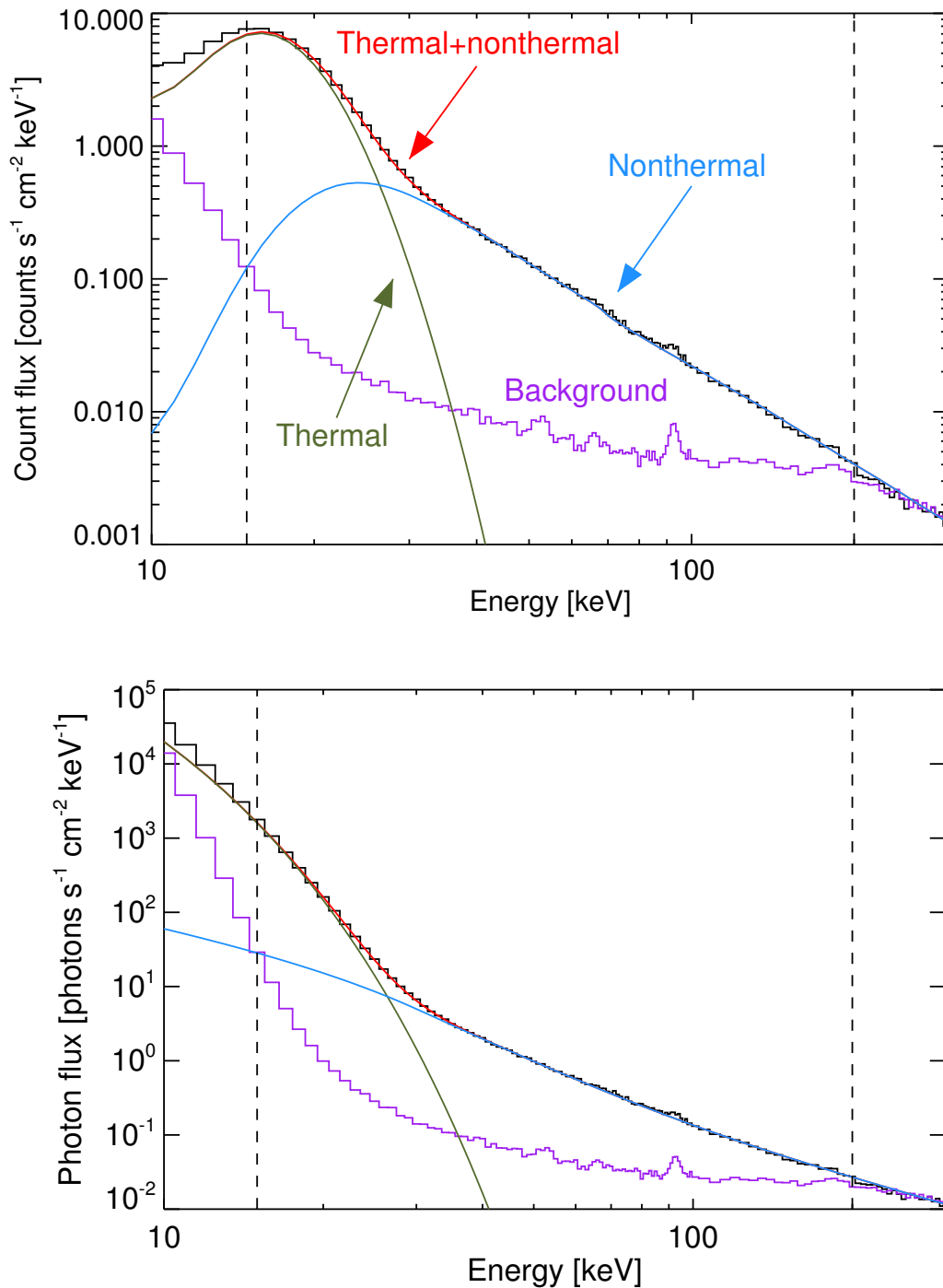


Figure 1.12: X-ray spectrum of the flare SOL2011-09-06 (X2.1). The emission from thermal plasma at ~ 30 MK is shown in green, while the nonthermal emission from accelerated electrons is presented in blue, showing emission even above 100 keV. The fit in the form of a continuous function is shown in red and background counts are depicted in purple, while the dashed lines give the energy boundaries of the fit. The discrepancy at lower energies might originate from an additional thermal component at lower temperatures, or uncertainties in the calibration.

2. **Emission measure:** defined as the product of the electron density squared and the plasma volume, i.e.:

$$EM = \int_V n_e^2 \cdot dV. \quad [\text{cm}^{-3}] \quad (1.10)$$

The EM determines the absolute magnitude of the photon flux: the bigger the EM, the larger the emission from the radiating plasma. In the example above, we made the assumption of a single-temperature plasma. In practice, plasma is likely multithermal, and the EM is a function of temperature. By using observations at different wavelengths and/or from different instruments, one can retrieve the differential emission measure (DEM) distribution as a function of temperature DEM(T) (e.g., Hannah & Kontar 2012; Cheng et al. 2012; Aschwanden et al. 2015). The total EM is calculated by integrating the DEM across all temperatures:

$$EM = \int_T DEM(T) \cdot dT. \quad (1.11)$$

An example of retrieving the DEM from simultaneous AIA and *RHESSI* observations is shown in Figure 1.13 (Battaglia et al. 2015). In this case, two peaks at $\log T = 6.1$ and $\log T = 6.8$ K are observed, suggesting that plasma emits predominantly at these temperatures.

The nonthermal tail of the flare spectrum depends on the injected electron flux and the power-law index:

$$F_{nth}(E) = F_e(E_0) \left(\frac{E}{E_0} \right)^{-\delta}, \quad [\text{electrons s}^{-1} \text{ keV}^{-1}] \quad (1.12)$$

where $F_{nth}(E)$ and $F_e(E_0)$ are electron fluxes at energies E and E_0 (normalization point) and δ is the power-law index. Here we introduced a slightly different version of the same formula for the accelerated electrons spectrum, as it follows the parameters obtained with spectral fitting in OSPEX more precisely. The (thick target) power-law fit provides three main parameters:

1. **Electron flux:** The total integrated electron flux, defined in the units of $[\text{electrons s}^{-1}]$. Using parameters from Equation 1.12, it is equal to

$$F_e^{tot} = \int_E F_{nth}(E) dE. \quad (1.13)$$

2. **Power-law index:** The slope of the electron distribution (nonthermal tail). This parameter is directly related to the efficiency of the acceleration mechanism: harder spectra (with lower indices) represent more efficient particle acceleration and vice versa.

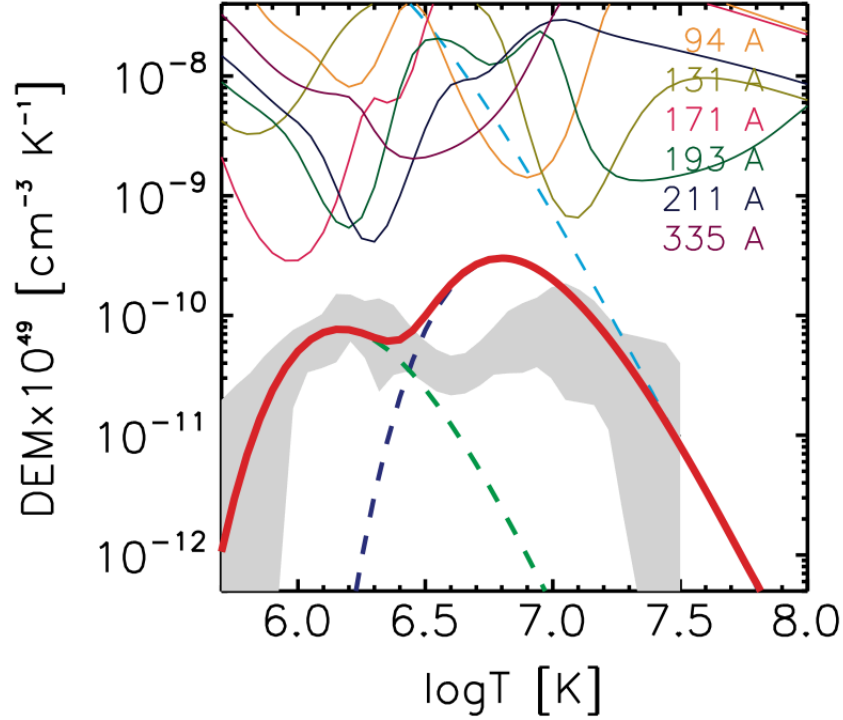


Figure 1.13: The DEM inferred from simultaneous AIA and *RHESSI* observations (red). The grey area shows the DEM inferred from AIA data only. Curves of different colors at the top denote the loci curves of AIA and *RHESSI*, which will be discussed in more detail in Chapter 4. Taken from Battaglia et al. (2015).

3. **Cutoff:** The cutoff energy is defined as the value where the cutoff in the nonthermal distribution is observed/estimated. This is required since the extrapolation of the power-law to lower energies would lead to unphysically large energy carried by the accelerated electrons. Two basic cutoffs/turnovers are discussed in the literature. The first one assumes there is a sharp break, with the nonthermal flux below the cutoff equal to zero. The other is a flat turnover, where the distribution below the turnover energy has a constant value. For more on this topic, we point to the review by Holman et al. (2011).

The above parameters can be used to estimate the nonthermal energy in a solar flare. Choosing the cutoff energy as the normalization point, the total integrated electron flux is given by:

$$\begin{aligned}
 F_e^{tot} &= \int_{E_c}^{\infty} \frac{F_e(E_c)}{E_c^{-\delta}} E^{-\delta} dE \\
 &= \frac{F_e(E_c) E_c}{\delta - 1}.
 \end{aligned}
 \tag{1.14}$$

By inverting the equation above, the relation between the normalization factor

and the integrated electron flux given by the fit is:

$$F_e(E_c) = \frac{F_e^{tot}(\delta - 1)}{E_c}. \quad (1.15)$$

The power of accelerated electrons can be calculated by integrating the nonthermal spectrum and inserting Equation 1.15 into 1.12:

$$\begin{aligned} P_{nth} &= \int_{E_c}^{\infty} F_{nth} E dE \\ &= \int_{E_c}^{\infty} \frac{F_e^{tot}(\delta - 1)}{E_c} \cdot \left(\frac{E}{E_c}\right)^{-\delta} \cdot E dE \\ &= F_e^{tot} E_c \frac{\delta - 1}{\delta - 2}. \end{aligned} \quad (1.16)$$

The total nonthermal energy is then calculated by integrating the power over the flare duration:

$$E_{nth} = \int_t P_{nth} dt. \quad (1.17)$$

Thus, by fitting the nonthermal part of the spectrum (using the thick-target approximation), one can obtain an estimate of the total nonthermal energy in the accelerated electrons. The estimate is heavily dependent on the power-law index and the cutoff/turnover energy. While the power-law index can be measured with good precision directly from the spectrum, estimating the cutoff/turnover energy is more complicated. The difficulty in determining the cutoff/turnover energy lies in the fact that the nonthermal emission at lower energies is masked by the much stronger thermal emission. Taking the spectrum in Figure 1.12 as an example, the cutoff energy can be anywhere below ~ 25 keV. Because the total electron flux F_e^{tot} also depends on the cutoff energy, the dependency of the nonthermal energy on this parameter is stronger than linear: $E_{nth} \sim E_c^{-\delta+2}$. For the observed power-law index of 4.2 in our example, the nonthermal energies for cutoffs of 10 and 25 keV would differ by a factor of $(25/10)^{\delta-2} = 7.5$. For flares with steeper spectra, the uncertainties can be even larger.

In conclusion, X-ray observations provide a simple and efficient tool to estimate flare energetics. However, this estimate is critically dependent on the cutoff energy, as shown in the example above. This is a significant obstacle as the nonthermal emission is masked by its thermal counterpart at low energies, and its direct measurement is extremely difficult. The advancement of focusing optics technologies, discussed in the next sections, might help in resolving this issue. Observations of individual footpoints with focusing optics X-ray instruments in combination with EUV instruments will help to constrain the range of energies of their nonthermal emission. Therefore, more precise estimates of the cutoff energy are expected from these observations.

1.4 X-ray instruments

This section is reserved for the discussion on the solar-dedicated X-ray instruments and imaging techniques used in the X-ray wavelength range. Currently, two basic types of imaging techniques are implemented: indirect methods, based on Fourier formalism, and focusing optics. Fourier-imaging was used in currently the only solar-dedicated X-ray instrument *RHESSI*, and it will also be applied in the *Spectrometer/Telescope for Imaging X-rays (STIX)*. It is based on the image reconstruction either from the time- (*RHESSI*) or space-modulated (*STIX*) photon flux, obtained when photons travel through two superposed sets of almost identical grids. The reasons for its widespread usage in the previous and current instrumentation are angular resolution and sensitivity which can be obtained, within the cost and size constraints (Hurford et al. 2002). In the following section, an introduction to the basic concepts will be given, while a detailed description of image reconstruction procedures for *RHESSI* and *STIX* will be given in Chapter 2. Focusing optics requires technologies which were not developed until recently, and much larger instrument dimensions. However, focusing optics allows even better sensitivity and dynamic range, which is why this approach will be used in the next generation solar-dedicated X-ray telescope: the *Focusing Optics X-ray Solar Imager (FOXSI)*.

1.4.1 *RHESSI, STIX and MiSolFa*

RHESSI has been the most important solar-dedicated X-ray mission since its launch in 2002 (*RHESSI* had its 16th anniversary in February 2018). The original paper about the mission by Lin et al. (2002) has more than 1000 citations, showing its importance for the solar physics community. Its construction and operation is managed in the Principal Investigator (PI, R. Lin 2002–2012 and S. Krucker 2012–present) mode at the University of California, Berkeley. Energetic processes on the Sun, such as solar flares, are the main focus of interest. Both imaging and spectroscopical analysis in the energy range between 3 keV and 17 MeV can be performed, providing images of solar flares even at very high energies above 100 keV with spatial resolution as high as 2.3'' (Hurford et al. 2002).

RHESSI consists of an imager made up of nine rotating modulation collimators shown in Figure 1.14. Each subcollimator contains a pair of identical grids consisting of equally spaced slits (X-ray transparent) and slats (X-ray opaque) and separated by a distance of 1.55 m, much larger than their period (defined by the distance between two consecutive slits/slats). The grids are located in front of nine germanium detectors. Depending on the angular displacement of a flux source with respect to the grids, the transmission of the incoming flux changes, showing a triangular profile. This change in angular displacement of off-axis sources is acquired through the rotation of the spacecraft, with a period of ~ 4 seconds, producing a time-modulated flux. The information about the source can be retrieved through principles of Fourier-imaging, where the amplitude and phase of the modulated flux can be connected to the source map producing it,

using some of the standardised algorithms like back-projection, CLEAN (Högbohm 1974) or maximum-entropy (Gull & Daniell 1978). More details on Fourier-imaging concepts will be given in Chapter 2. Figure 1.15 shows how changes in the source intensity, location and angular displacement affect the modulated flux.

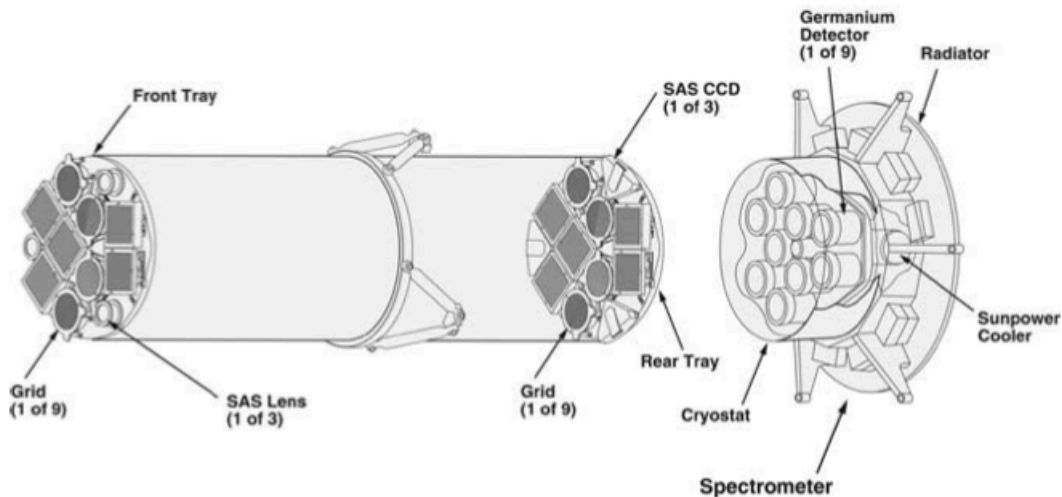


Figure 1.14: *RHESSI* imager with nine rotating subcollimators. Taken from Hurford et al. (2002).

STIX is the next solar-dedicated HXR telescope, planned for launch as one of the ten instruments on the *Solar Orbiter* mission in February 2020 (see Figure 1.16). It is developed by the heliophysics group at FHNW, Switzerland, and it has been the group's core project. *Solar Orbiter* will have a highly elliptical orbit, with its closest point to the Sun of 0.28 AU. The orbit will also be inclined with respect to the Earth-Sun plane in order to make observations of solar poles, which will provide a new view on solar magnetic field configurations and solar activity cycles. Because *STIX* will be in the main focus of Chapter 2, the details of its imaging system can be found there. Here we just note that, unlike *RHESSI*, which modulates the incoming photon flux through a rotating spacecraft, *STIX* imaging is based on spatial-modulations in the form of moiré patterns.

The *Micro Solar-Flare Apparatus (MiSolFa)* (Casadei et al. 2018) is a cube-satellite X-ray imager currently under development at FHNW, Switzerland. It is based on the same principles as *STIX*, but within the cubesat mission constraints. *MiSolFa* is planned for launch into the Earth orbit in 2022, in order to provide contextual HXR observations of solar flares during the next solar maximum. *MiSolFa* has four main scientific goals (Casadei 2016):

1. **Directivity:** Having two cross-calibrated X-ray instruments simultaneously observing the same flare provides a direct observation of the electron beam directivity in solar flares (Casadei et al. 2017). As each instrument observes the same flare from different angles, directivity of the same accelerated electron distribution can be quantified both in the corona and in the chromo-

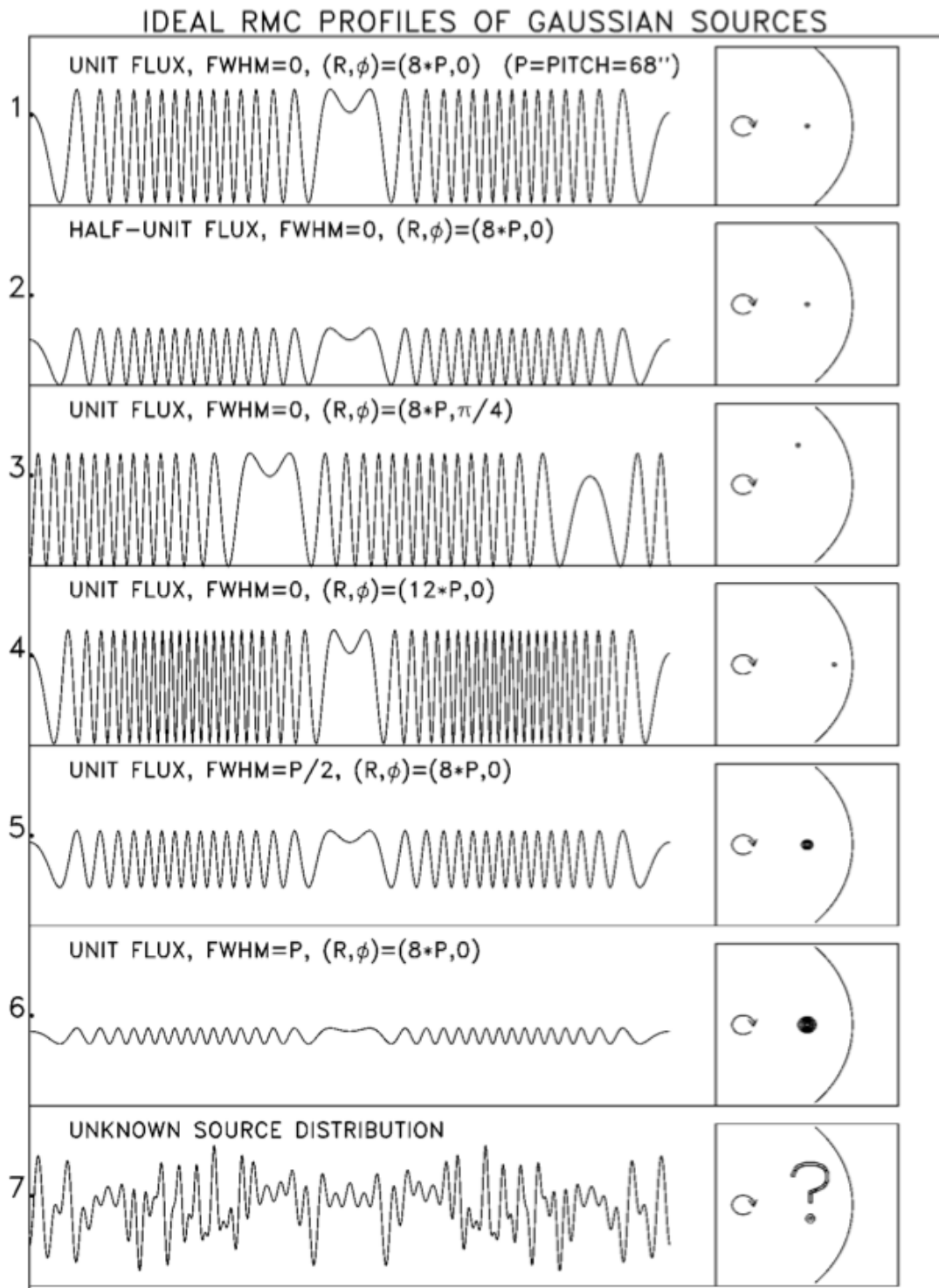


Figure 1.15: *RHESSI* time-modulated profiles in dependence of the source intensity, azimuthal location, off-axis displacement and source size. The final panel shows a modulation from a complex source. Taken from Hurford et al. (2002).

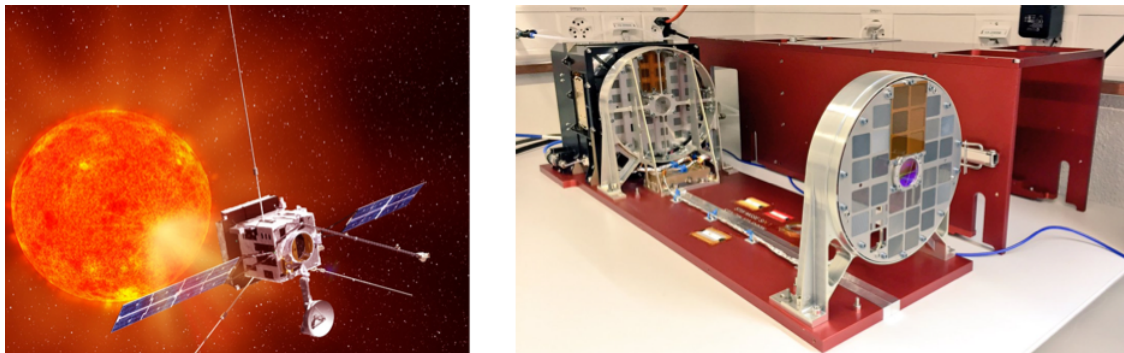


Figure 1.16: *Left: Solar Orbiter.* Taken from https://www.nasa.gov/mission_pages/sunearth/news/ESA-SolarOrbiter.html. *Right: STIX flight model before the delivery in July 2017.*

sphere. The influence of acceleration process and particle transport on the electron distribution anisotropy will be measured.

2. **Coronal-footpoint sources:** Simultaneous observations of a flare with two instruments can be particularly useful when a flare is occulted in the line-of-sight of one instrument. This would lead to independent measurements of coronal and footpoint sources. Many questions about the transport of particles will be resolved this way.
3. **Thermal volumes:** By observing the same plasma volume from different directions, a 3D picture of heated plasma can be acquired. Precise knowledge on the shape of plasma, its temperature and density distribution in space can be obtained, which will also greatly contribute to modelling of solar flares.
4. **Stand-alone observations:** Provide solar flare HXR observations outside *STIX* observing windows, and across other parts of the solar disk (as it has a different viewing direction).

1.4.2 *NuSTAR* and *FOXSI*: Towards focusing optics

NuSTAR is the astronomical HXR observatory operating in the energy range between 3 and 79 keV. Even though its main scientific focus are faint astrophysical sources such as black holes, supernova remnants, and our galaxy, it can be pointed to the Sun (Grefenstette et al. 2016). *NuSTAR*'s main part consists of Wolter-I type X-ray optics containing 133 nested grazing incidence shells which focus HXR photons onto two independent focal plane modules (FPMA and FPMB) with CdZnTe detectors (Harrison et al. 2013). The extendible mast has been used after the launch to obtain the focal length between the optics and the detectors of ~ 10 m. A schematic view of the instrument and a photo of *NuSTAR* detectors can be found in Figure 1.17. The main advantages of using focusing optics when compared to Fourier-imaging methods are reduced background

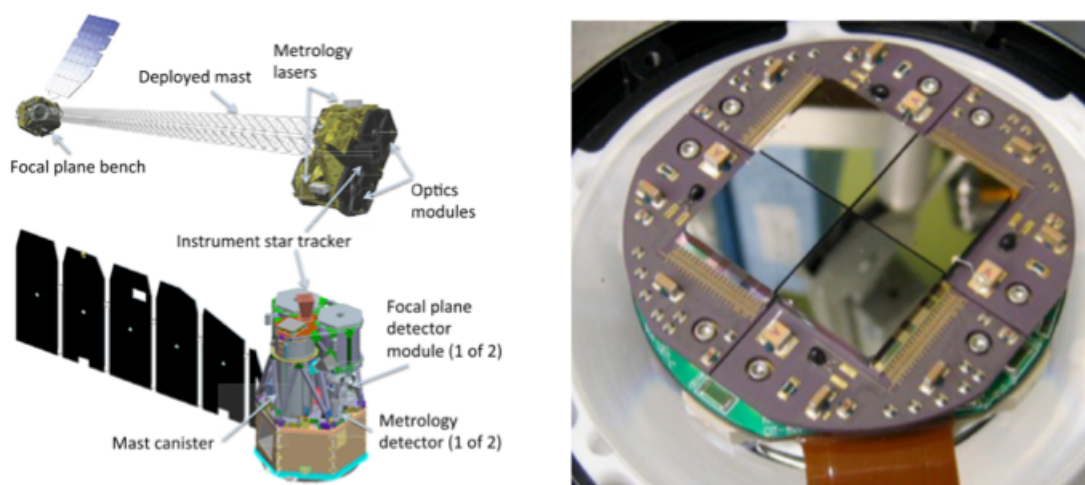


Figure 1.17: Left: *NuSTAR* instrument. Right: CdZnTe detectors forming a (2x2) matrix. Taken from Harrison et al. (2013).

rates, better sensitivity and improved imaging dynamic range, already shown in *NuSTAR* solar observations carried-out so far (Grefenstette et al. 2016; Hannah et al. 2016; Glesener et al. 2017; Wright et al. 2017). However, as *NuSTAR* was not designed for solar purposes, it experiences some difficulties when pointed to the Sun. The first one are ghost-rays, made of photons coming from sources outside the field-of-view (FoV). These photons enter the optics system at a shallow angle and bounce only once off the Wolter-I mirrors before being focused on the detectors. The other one is the relatively low throughput of the *NuSTAR* electronics system, with a maximum read-out of 400 counts per second per telescope. This decreases the instrument's sensitivity for detection of faint, high energy spectral components (nonthermal or hot component). Therefore, a solar-dedicated X-ray instrument, designed optimally for solar observations, is one of the key priorities for future planning.

FOXSI is currently a sounding rocket payload, already successfully launched on three occasions in 2012, 2014 and 2018 (Krucker et al. 2014). The third launch was performed on 2018 September 7², also in parallel to *NuSTAR* observations on September 7–9. *FOXSI* has a spatial resolution of $\sim 9''$ and a factor of five smaller effective area compared to *NuSTAR*. The advantages of its focusing optics system (lower background, improved dynamics range) when compared to Fourier-imaging were already evident in the observations carried-out during the first launch, when it observed a microflare simultaneously with *RHESSI* (see Figure 1.18). *FOXSI* has a higher low-energy threshold (4 keV) than *NuSTAR* (2.5 keV), in order to keep the livetime high for high energy photons, where the faint nonthermal component is hidden. The differences between *FOXSI-2* (second launch performed in 2014) and *NuSTAR* will also be explained in more detail in Chapter 4 on the example of their simultaneous observations of an occulted active region.

² <http://foxsi.umn.edu/>

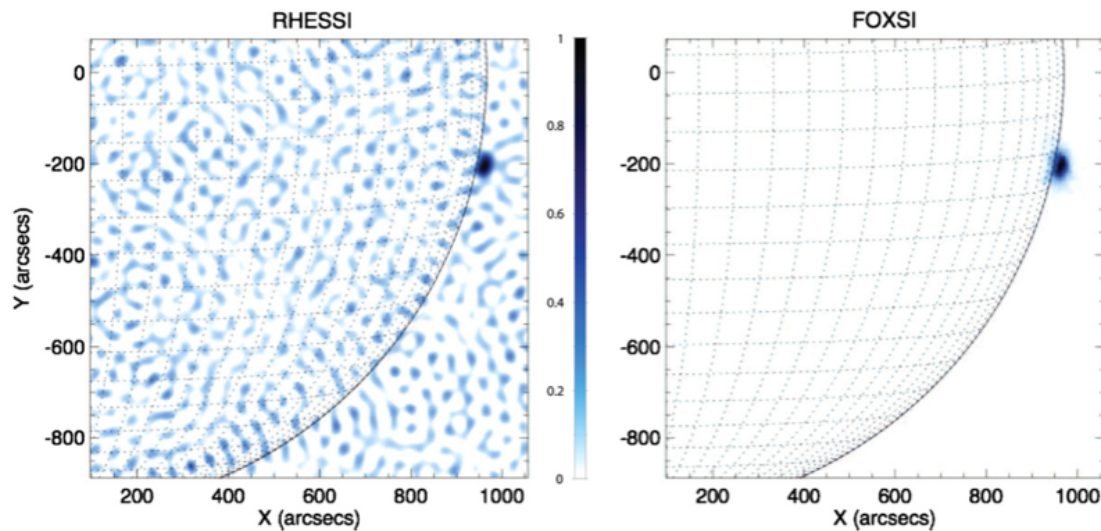


Figure 1.18: Comparison of *RHESSI* (left) and *FOXSI* (right) image of a microflare on 2012 November 2. *RHESSI* reconstruction creates noise in the entire FoV, while an almost noise-free image is obtained with *FOXSI*. Taken from Krucker et al. (2014).

As a final comparison of all instruments, their main properties are presented in Table 1.1. It contains the basic information about the energy range and resolution, imaging technique, field of view, angular and temporal resolution, effective area, launch date, mission lifetime, and orbit of each instrument. The data have been taken from Lin et al. (2002) (*RHESSI*), Harrison et al. (2013) (*NuSTAR*) and internally (*STIX* and *FOXSI*). The reported values for specifications like the energy resolution and effective area are given at a specific energy indicated in the table.

In summary, both Fourier-transform based methods and focusing optics have advantages and limitations. The present time will probably be remembered as the onset of using focusing optics in the X-ray observations of the Sun. However, the author believes that Fourier-imaging will remain important, as it efficiently combines high performance with size and cost constraints of space instruments.

Bibliography

- Acton, L. W. 1964, *Nature*, **204**, 64
- Aschwanden, M. J., Boerner, P., Caspi, A., et al. 2015, *Sol. Phys.*, **290**, 2733
- Aschwanden, M. J., Tarbell, T. D., Nightingale, R. W., et al. 2000, *ApJ*, **535**, 1047
- Avrett, E. H. & Loeser, R. 2008, *ApJS*, **175**, 229
- Babcock, H. W. 1961, *ApJ*, **133**, 572
- Bastian, T. S., Benz, A. O., & Gary, D. E. 1998, *ARA&A*, **36**, 131
- Battaglia, M., Motorina, G., & Kontar, E. P. 2015, *ApJ*, **815**, 73
- Benz, A. O. 2017, *Living Reviews in Solar Physics*, **14**, 2

| Specification | <i>RHESSI</i> | <i>STIX</i> | <i>NuSTAR</i> | <i>FOXSI</i> ^a |
|---|---------------------|---------------------|---------------|---------------------------|
| E range [keV] | 3 – 17000 | 4 – 150 | 2.5 – 79 | 5 – 80 |
| E resolution (FWHM) @ 6 keV [keV] | ~ 1 | 1 | 0.4 | ~ 1 |
| Field of view | full Sun | full Sun | 12' × 12' | 9' × 9' |
| Angular resolution (FWHM) | 2.3'' | 7'' | 18'' | 8'' |
| Effective area @ 20 keV [cm ²] | 30 – 60 | ~ 6 ^b | ~ 800 | ~ 50 |
| Electronic throughput [ct s ⁻¹] | 3 · 10 ⁵ | 6 · 10 ⁵ | 800 | 10 ⁶ |
| Imaging system | mod. fluxes | moiré | foc. optics | foc. optics |
| Launch date | Oct. 2002 | 2020 | Jun. 2012 | 2022 |
| Mission lifetime | 2002–2018 | 2020–? | 2012– | 2022–? ^c |

^a The specifications are given for the satellite version, under the NASA Small Explorer program (SMEX) constraints.

^b Because *STIX* comes much closer to the sun (0.28 AU at the closest point), it gains a factor of $(1/0.28)^2 \sim 13$ in effective area to other instruments in Earth orbit. This is caused by the dependence of the incoming flux on the distance $I_{ph} \sim 1/R^2$.

^c Depending which version (SMEX/MIDEX), or whether the mission is selected for funding.

Table 1.1: Specifications of current and planned X-ray instruments.

- Benz, A. O. & Krucker, S. 2002, *ApJ*, **568**, 413
- Brown, J. C. 1971, *Sol. Phys.*, **18**, 489
- Carrington, R. C. 1859, *MNRAS*, **20**, 13
- Casadei, D. 2016, *STIX-LB-0106-FHNW*
- Casadei, D., Hurford, G. J., Kuhar, M., Lastufka, E., & Torre, G. 2018, In preparation,
- Casadei, D., Jeffrey, N. L. S., & Kontar, E. P. 2017, *A&A*, **606**, A2
- Caspi, A., Krucker, S., & Lin, R. P. 2014, *ApJ*, **781**, 43
- Chen, B. & Bastian, T. S. 2012, *ApJ*, **750**, 35
- Cheng, X., Zhang, J., Saar, S. H., & Ding, M. D. 2012, *ApJ*, **761**, 62
- Cranmer, S. R. & van Ballegoijen, A. A. 2005, *ApJS*, **156**, 265
- Dennis, B. R. & Zarro, D. M. 1993, *Sol. Phys.*, **146**, 177
- Emslie, A. G., Dennis, B. R., Shih, A. Y., et al. 2012, *ApJ*, **759**, 71
- Freedman, R. & Kaufmann, W. J. 2005, *Universe, 7th edition* (W. H. Freeman and Company, New York)
- Galloway, R. K., Helander, P., MacKinnon, A. L., & Brown, J. C. 2010, *A&A*, **520**, A72
- Glesener, L., Krucker, S., Hannah, I. G., et al. 2017, *ApJ*, **845**, 122
- Grefenstette, B. W., Glesener, L., Krucker, S., et al. 2016, *ApJ*, **826**, 20
- Gull, S. F. & Daniell, G. J. 1978, *Nature*, **272**, 686
- Hannah, I. G., Christe, S., Krucker, S., et al. 2008a, *ApJ*, **677**, 704
- Hannah, I. G., Grefenstette, B. W., Smith, D. M., et al. 2016, *ApJL*, **820**, L14
- Hannah, I. G. & Kontar, E. P. 2012, *A&A*, **539**, A146
- Hannah, I. G., Krucker, S., Hudson, H. S., Christe, S., & Lin, R. P. 2008b, *A&A*, **481**, L45

BIBLIOGRAPHY

- Harrison, F. A., Craig, W. W., Christensen, F. E., et al. 2013, *ApJ*, **770**, 103
- Hawley, S. L., Fisher, G. H., Simon, T., et al. 1995, *ApJ*, **453**, 464
- Högbom, J. A. 1974, *A&AS*, **15**, 417
- Holman, G. D., Aschwanden, M. J., Aurass, H., et al. 2011, *Space Sci. Rev.*, **159**, 107
- Hudson, H. S. 1991, *Sol. Phys.*, **133**, 357
- Hurford, G. J., Schmahl, E. J., Schwartz, R. A., et al. 2002, *Sol. Phys.*, **210**, 61
- Hurford, G. J., Schwartz, R. A., Krucker, S., et al. 2003, *ApJL*, **595**, L77
- Klimchuk, J. A. 2006, *Sol. Phys.*, **234**, 41
- Krucker, S., Battaglia, M., Cargill, P. J., et al. 2008, *A&A Rev.*, **16**, 155
- Krucker, S., Christe, S., Glesener, L., et al. 2014, *ApJL*, **793**, L32
- Krucker, S., Hudson, H. S., Glesener, L., et al. 2010, *ApJ*, **714**, 1108
- Lemen, J. R., Title, A. M., Akin, D. J., et al. 2012, *Sol. Phys.*, **275**, 17
- Lin, R. P., Dennis, B. R., Hurford, G. J., et al. 2002, *Sol. Phys.*, **210**, 3
- Lin, R. P. & Hudson, H. S. 1971, *Sol. Phys.*, **17**, 412
- Lin, R. P., Krucker, S., Hurford, G. J., et al. 2003, *ApJL*, **595**, L69
- Livingston, W., Harvey, J. W., Malanushenko, O. V., & Webster, L. 2006, *Sol. Phys.*, **239**, 41
- MacKinnon, A. L. & Mallik, P. C. V. 2010, *A&A*, **510**, A29
- Masuda, S., Kosugi, T., Hara, H., Tsuneta, S., & Ogawara, Y. 1994, *Nature*, **371**, 495
- Maunder, E. W. 1904, *MNRAS*, **64**, 747
- McIntosh, S. W., de Pontieu, B., Carlsson, M., et al. 2011, *Nature*, **475**, 477
- Neupert, W. M. 1968, *ApJL*, **153**, L59
- Parker, E. N. 1955, *ApJ*, **122**, 293
- Parker, E. N. 1988, *ApJ*, **330**, 474
- Parnell, C. E. & Jupp, P. E. 2000, *ApJ*, **529**, 554
- Pesnell, W. D., Thompson, B. J., & Chamberlin, P. C. 2012, *Sol. Phys.*, **275**, 3
- Saint-Hilaire, P. & Benz, A. O. 2005, *A&A*, **435**, 743
- Schou, J., Scherrer, P. H., Bush, R. I., et al. 2012, *Sol. Phys.*, **275**, 229
- Shimizu, T. 1995, *PASJ*, **47**, 251
- Solanki, S. K. 2003, *A&A Rev.*, **11**, 153
- Solanki, S. K. & Schmidt, H. U. 1993, *A&A*, **267**, 287
- Sui, L., Holman, G. D., & Dennis, B. R. 2006, *ApJL*, **645**, L157
- Tomczyk, S., McIntosh, S. W., Keil, S. L., et al. 2007, *Science*, **317**, 1192
- Veronig, A., Vršnak, B., Dennis, B. R., et al. 2002, *A&A*, **392**, 699
- Warmuth, A. & Mann, G. 2016, *A&A*, **588**, A116
- West, M. J. & Seaton, D. B. 2015, *ApJL*, **801**, L6
- Woods, T. N. 2014, *Sol. Phys.*, **289**, 3391
- Woods, T. N., Hock, R., Eparvier, F., et al. 2011, *ApJ*, **739**, 59
- Wright, P. J., Hannah, I. G., Grefenstette, B. W., et al. 2017, *ApJ*, **844**, 132

Chapter 2

STIX imaging concepts and grids calibration

This chapter explains the basics of image reconstruction methods for *RHESSI* and *STIX*. Similarities and differences between the image reconstruction processes of the two instruments are described. The importance of grids and the need for their careful characterization in both instruments is explained. In the second part of the chapter, a detailed description of the *STIX* grids characterization from optical and X-ray measurements is given. More emphasis is given on the method used to extract the grid parameters, while the final results that will be used for actual data analysis during the nominal mission phase starting in later 2021 will be reported in a future publication.

2.1 *RHESSI* and *STIX* imaging systems

2.1.1 Fourier transform

To understand how imaging concepts of *RHESSI* and *STIX* work, it is useful to introduce the basic concepts of Fourier transforms. First, let us denote the spatial coordinate system of the source on a solar image with (x, y) , where x is a vector in that system. The plane of Fourier frequencies that corresponds to the source distribution is denoted with (u, v) , and a vector in this plane with q . The Fourier transform of the source spatial intensity distribution is given by (e.g., Hurford et al. 2002; Giordano et al. 2014):

$$F(u, v) = \int f(\mathbf{x}) e^{i2\pi\mathbf{q}\cdot\mathbf{x}} d\mathbf{x}, \quad (2.1)$$

and it is usually termed *visibility* in radio and X-ray imaging. Therefore, a visibility is basically the value of the Fourier transform of a source distribution in a point in the (u, v) plane, characterized by its amplitude and phase. Different instruments rely on different approaches in determining Fourier components from the collected data. In general, however, a connection between Fourier components and observed fluxes can be determined: $F(u, v) \leftrightarrow N(p, t)$, where $N(p, t)$ is the number of detected photons at pixel p and time t . Each detector in an instrument allows the measurement of the amplitude and phase of one Fourier component at a given time. Here, amplitude tells about the intensity of incoming flux, while phase reveals information on its location. By sampling enough

Fourier components (through having enough detectors), one can determine the source distribution $f(x)$ by performing the inverse Fourier transform on Equation 2.1, over the measured visibilities. It is instructive to note that basically the same principles are also used in radio interferometry, where different antennas measure different Fourier components.

2.1.2 *RHESSI*

In *RHESSI*, measurements of Fourier components are acquired through the time modulation of the incoming flux. To accomplish that, the *RHESSI* imager consists of nine rotating modulating collimators, each consisting of a pair of identical grids (same period p and orientation α) made of X-ray opaque slats and transparent slits¹ and located $L=1.55$ m apart. The periods range from $34 \mu\text{m}$ to 2.75 mm. When the incidence angle of incoming X-rays changes, the transmission of a grid pair changes as well. For the transmission to go from maximum of 50% (in the case of slits and slats of equal width s) to zero, a change in incidence angle of $p/2L$ is needed, shown schematically in Figure 2.1. Changes in incidence angle are obtained through the rotation of the spacecraft, with a period of 4 s, which results in a modulated incoming flux. As the ratio $p/2L$ is very small for all grids, many modulations are obtained during each rotation of the spacecraft.

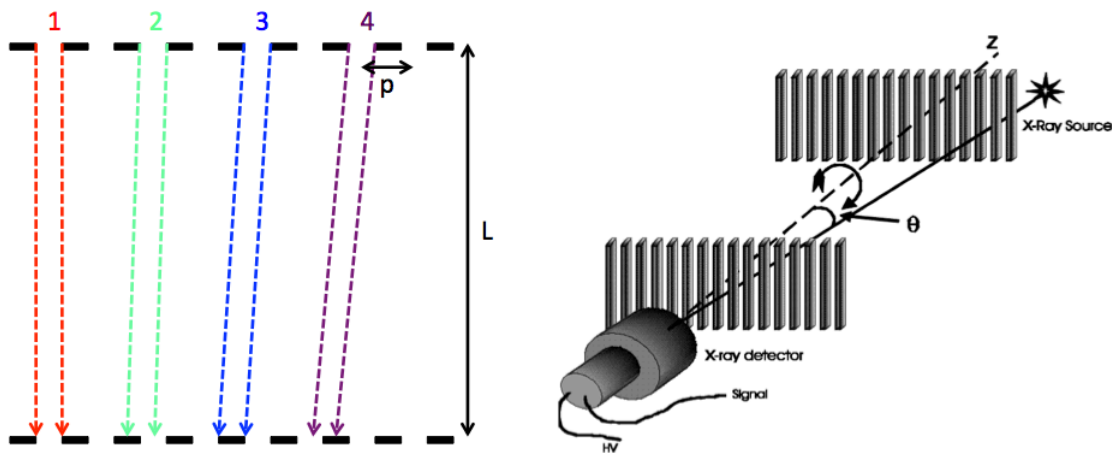


Figure 2.1: Geometry of the *RHESSI* setup. *Left:* Each collimator consists of two pairs of identical grids with periods p and separation $L = 1.55$ m. If the direction of the incoming photon X-ray flux is vertical, the maximum transmission is observed (1). As the incidence angle starts to increase (2), the transmission decreases, as part of the transmitted light gets blocked by the second grid. For an incidence angle of $\sin(\alpha) = p/(2L)$, no transmission is observed. For even larger incidence angles, transmission increases again. *Right:* Time modulation of the signal with *RHESSI* (taken from <https://hesperia.gsfc.nasa.gov/rhessi3/>).

In order to reconstruct the images, pointing and roll angle of the spacecraft

¹ <https://hesperia.gsfc.nasa.gov/rhessi3/mission/spacecraft-instrument/grids/index.html>

have to be known at any time. Roll angle is defined as the instantaneous orientation of grids in the line-of-sight relative to a reference point (the solar north in this example). Another important parameter for image reconstruction is aspect phase, which can be understood as follows. In order to complete one modulation cycle of incoming flux, a change in the incidence angle of $[-p/2L, p/2L]$ is needed (as shown in Figure 2.1). An alternative angle, proportional to the incidence angle, can be introduced, such that it spans the range of $[0, 2\pi]$, or 360 degrees, instead of $[-p/2L, p/2L]$. Aspect phase is actually defined in map coordinates and describes the change in modulation pattern of a source along the direction orthogonal to the grid slits on an image of the Sun.

As the spacecraft rotates, information about detected X-ray flux and spacecraft pointing are stored (the reader can think of this information as a data cube of incoming flux, roll angle and aspect phase). Therefore, each time bin can be represented in the roll/phase plane as one data point (incoming flux would represent the amplitude in the third dimension). In the course of one spacecraft rotation, this plane is sampled at a number of points, shown in the top left panel of Figure 2.2. In order to reconstruct the image, one has to determine visibilities at various stages of spacecraft rotation, or at different roll angle bins. Two (out of many) possible choices of roll bin sizes are shown with green (good) and red (bad). In the top right panel, sampling during multiple rotations is shown, together with one possible choice of roll/phase binning, with 12×12 bins. Once the roll bin size is chosen, a distribution of incoming flux in dependence of aspect phase can be constructed, for each roll bin. This is shown in the bottom panel, for a single roll bin. From each such distribution, the visibility amplitude and phase can be calculated by fitting a sinusoidal function. This can be thought as determining the evolution of amplitude and phase of a collimator in dependence of spacecraft roll angle, or calculating visibilities at different stages of the spacecraft rotation (it is equivalent to sampling the Fourier (u, v) plane on a circle with a radius $1/p$). Even though having a large number of roll bins is beneficial as it allows sampling more Fourier components, each visibility measurement (roll angle bin) should contain at least one modulation cycle, as otherwise incomplete sampling of aspect phases would be obtained. In other words, each roll bin has to be large enough to contain data sampling the whole aspect phase range: $[0, 360]$. When this would not be the case, there would be missing bins in distributions such as shown in the lower panel, and possible (systematic) errors in determining amplitude and phase of visibilities might arise. One problematic choice of roll bin size is shown in red in the top left panel, since it does not contain the full modulation cycle (only the phase range $\sim [100, 200]$ is covered). Of course, a better sampling of roll/phase space is obtained through stacking data from multiple rotations. This increases the statistics in distributions shown in middle panels, and allows more precise estimates of the visibility parameters.

In practice, the visibility amplitude determines the intensity of the transmitted photon flux through the slits, while the phase provides the information on the slit positions on a solar map. This is shown in Figure 2.3 for the flare SOL2011-09-24 (X1.9) and collimator 8. First, an image from a 0.02 s ($1/200$ of a rotation)

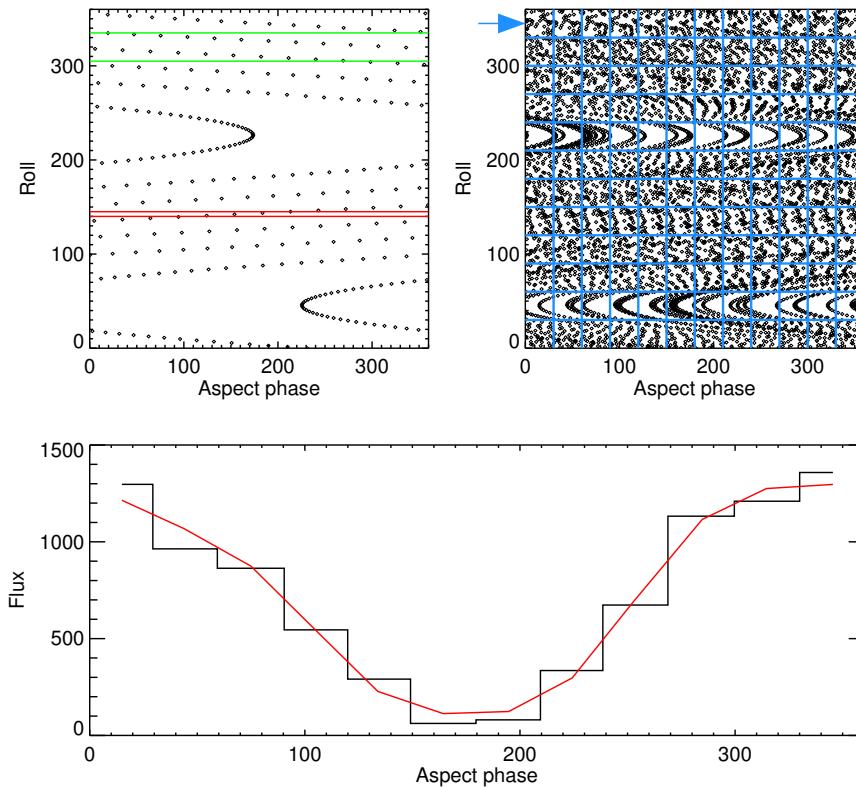


Figure 2.2: Determining visibilities in *RHESSI* image reconstruction process. *Top:* The left panel shows the number of time steps (roll angle/aspect phase pairs) for one full rotation. Green and red represent a good and a bad choice of the roll bin size, respectively. The right panel shows the number of steps for multiple rotations, together with one possible choice of roll/phase binning (blue). *Bottom:* Grouping data into roll angle bins allows determining visibility amplitude and phase by fitting a sinusoidal function to the distribution of counts vs. aspect phase. The shown measurement belongs to the roll bin indicated by the blue arrow in the top right panel.

time bin is created, where the positions of slits on the Sun map can be seen (*a*). Panel *b* shows a map with the integration time of 0.2 s (1/20 of a full rotation), while panel *c* shows the map after 1/10 of a full rotation. As more and more maps are added together, map pixels are populated with more data. This process preferentially populates pixels corresponding to the source location, as shown in panel *d* for 1/4 of a rotation. Also, summing data from many rotations improves the image quality (panels *e* and *f* show the maps obtained by integrating through 1 and 10 *RHESSI* rotations, respectively). This procedure is equal to mapping of the Fourier (u, v) space with points on a circle with the diameter of $1/p$. Adding more detectors improves the image quality even further, as different detectors represent circles with different diameters in the (u, v) plane. This is shown in panels *g-i*, where images using 3, 6, and all 9 detectors are shown.

The above procedure summarizes the most basic algorithm for image recon-

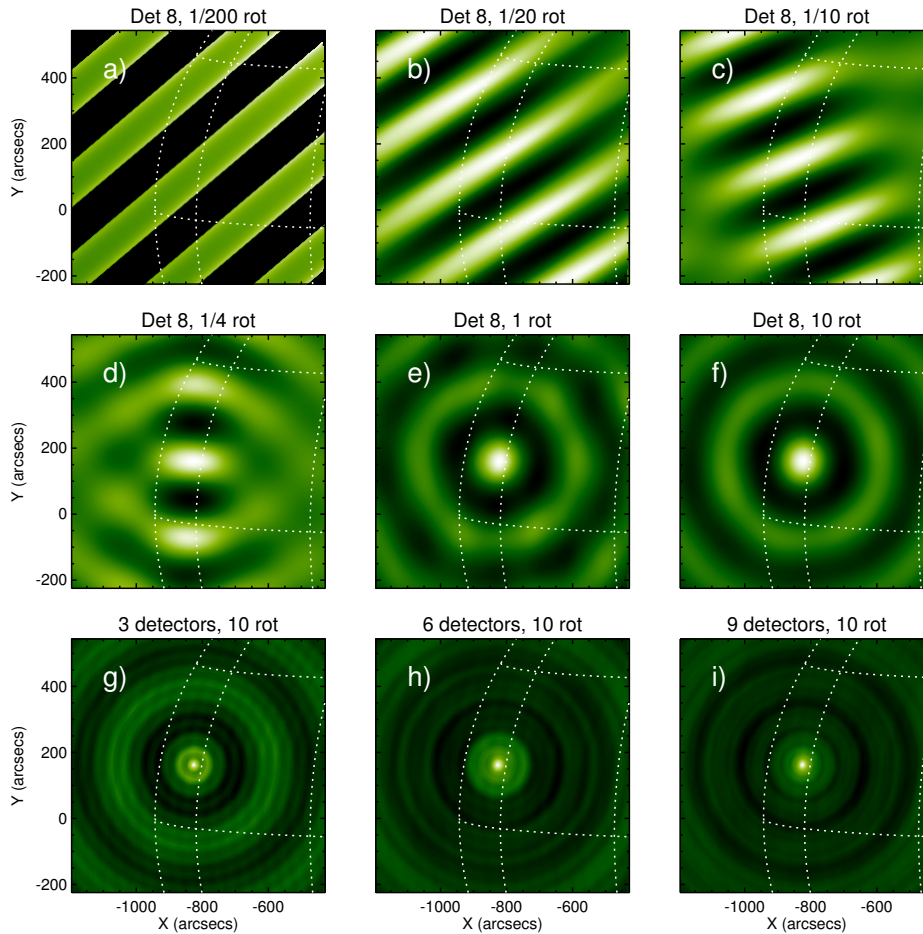


Figure 2.3: Including more rotations and detectors increases the quality of the *RHESSI* image. *RHESSI* image with the integration time of $0.02\text{ s}=1/200$ (a), $0.2\text{ s}=1/20$ (b) and $0.4\text{ s}=1/10$ (c) rotation. Panels d-f show *RHESSI* images after 1/4, 1 and 10 rotations. Bottom panels g-i show how including more grids leads to an even better image quality. The solar limb is shown with the dashed white line.

struction using Fourier analysis: the *back-projection*. Additionally, many other imaging algorithms have been developed and used, both in *RHESSI* imaging, and X-ray/radio astronomy overall (see *RHESSI* book, Lin et al. 2003). Some of these include the CLEAN algorithm (Högbom 1974), maximum entropy methods (Sato et al. 1999), forward-fitting (Aschwanden et al. 2002), pixon (Metcalf et al. 1996), etc. These algorithms can improve the image quality even further; however, this is outside the scope of this chapter.

2.1.3 *STIX*

The next solar-dedicated instrument for solar X-ray observations is *STIX*, one of ten instruments to be launched on-board the *Solar Orbiter* mission, developed by

the European Space Agency (ESA) and scheduled for launch in 2020 (see Figure 1.16). Since having a rotating spacecraft is not a possibility for *STIX*, it uses a somewhat different approach to X-ray imaging. Instead of having rotating pairs of grids, *STIX* reconstructs the image through spatial modulation of the incoming flux: moiré patterns.

Moiré patterns result when two grids of similar periods and orientations are superposed (e.g., Gabrielyan 2007), schematically shown in Figure 2.4, together with the grid geometrical properties like period, slit width and orientation. In this case, moiré pattern runs along the direction highlighted with the schematic sinusoidal function, representing the smoothed intensity of the transmitted light along the direction of the moiré pattern. The average values of orientation and period of a grid pair determine the Fourier component that is measured, while their difference determines the period and orientation of the moiré pattern. By changing slit width, slit orientation, or both, moiré patterns can be obtained along different directions.

Because it is impractical to have detectors sampling the incoming flux in various directions, *STIX* grids have been designed so that all windows create moiré along the same direction, with the moiré period matching the detector width. This sets constraints on the possible values of orientation and period of *STIX* grids. Another constraint was the adequate sampling of the Fourier (u, v) plane, in order to obtain the best quality of images possible. *STIX* has 32 windows in both front and rear segments, 30 grid pairs and 2 windows used for background and flare location estimates (see Figure 2.5). The grids were divided in four segments based on their geometrical properties and the ways they were produced. The coarsest grids are located in the bottom and their numbers are marked with green. Grids with intermediate periods are located to the left (red) and right (purple) to the finest grids (white). The grids have periods ranging from 38 to 1000 μm and orientations ranging from 10° to 170° in steps of 20° (Casadei 2016a). Therefore, there are 3 grid pairs with different orientations having the same period (angular resolution).

A simulation of the transmission profile of two grids, with slightly different orientations and periods, is shown in Figure 2.6. In the upper panel, a superposition of the two grids is shown, creating a moiré modulation along the detector axis, with one period of moiré modulation highlighted with green vertical lines. In *STIX*, as explained above, the grids are designed so that the moiré period is equal to the detector width. The transmitted photon flux is shown with the black triangular distribution in the lower panel. It can be seen that this distribution contains two modulations: the low-frequency (moiré), and the high-frequency (seen through small variations on top of moiré). In practice, however, the high frequency component cannot be sampled, and the detected flux is better represented by the smooth triangular function (Prince et al. 1988) shown in red. This can be approximated, after correcting for detector efficiency, livetime, and transmission, with (Casadei 2014):

$$f(\psi) = k + c \cdot \cos(\psi + \psi_0), \quad (2.2)$$

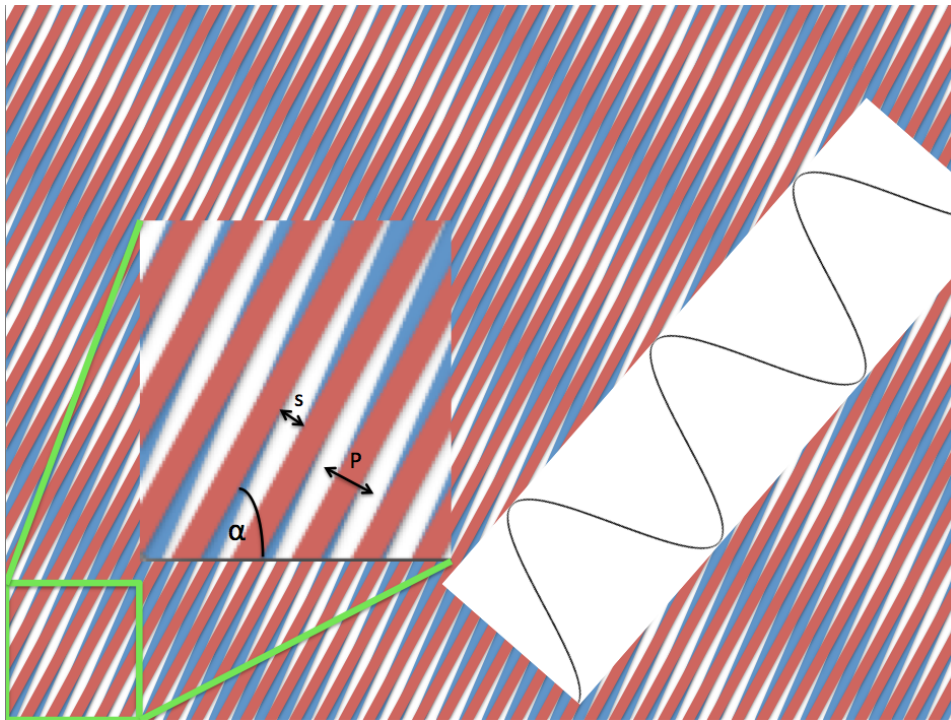


Figure 2.4: Moiré pattern occurs when two grids of slightly different periods and/or orientations are superposed. Slit width, period and orientation angle of one of the grids are shown in the inset. A smoothed transmission profile of the moiré modulation is approximated with a sinusoidal function.

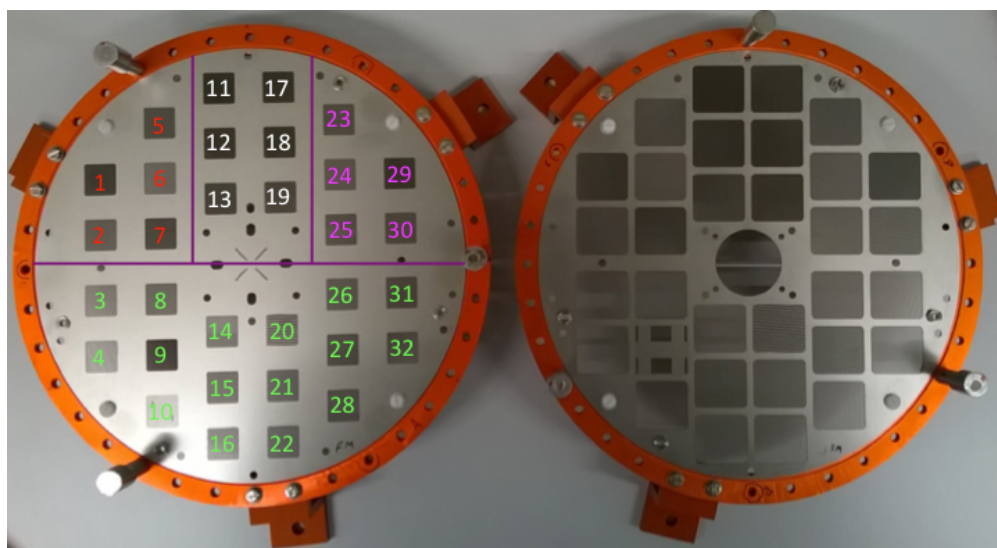


Figure 2.5: *STIX* rear (left) and front (right) grids.

where ψ is the angular variable spanning the spatial range of the detector (transformation goes from physical units in length to 2π in ψ). In this notation, c and ψ_0 are the amplitude and phase of the moiré pattern, respectively. *STIX* detectors have four pixels, sampling the above function in 4 bins. They are highlighted with pale purple, blue, green, and orange in the schematic representation in Figure 2.6. It can be shown (Casadei 2014) that the relationship between the observed fluxes in these 4 pixels uniquely define the amplitude and phase of the moiré modulation:

$$c = \frac{\sqrt{2}}{4} \sqrt{(A - C)^2 + (D - B)^2}, \quad (2.3)$$

$$\psi_0 = \arctan \frac{D - B}{A - C}. \quad (2.4)$$

Again, this is equal to sampling the Fourier (u, v) plane with a single point, or determining a visibility connected to a given collimator. Because *STIX* does not rotate, each collimator samples the (u, v) plane in a single fixed point, and not a complete circle as in *RHESSI*. However, by the design of *STIX* grids, these points are spread out in order to obtain the best coverage as possible, and they are shown in Figure 2.7. Circles sampled by *RHESSI* collimators are also shown for comparison. One can immediately see the differences between the instruments: *RHESSI* samples the (u, v) space in nine circles, while *STIX* does the same in 30 points. The intrinsic difference in sampling the Fourier plane comes from their different approaches to Fourier imaging: while *RHESSI* determines Fourier components through time modulation of the incoming flux, *STIX* modulates the incoming flux spatially through moiré patterns.

As in the case of *RHESSI*, measured (amplitude, phase) pairs at a given time determine the intensity and positions of *STIX* grids on the solar map. By combining information from all grids, a source map can be retrieved. In order for this procedure to work efficiently, i. e., to determine amplitudes and phases of various Fourier components, properties of *STIX* grids have to be determined precisely. The orientation and period of a moiré pattern is critically dependent on geometrical properties of the grid pair producing it. Small changes in the orientation and/or period of a grid can lead to large variations in both the period and direction of the moiré pattern. Therefore, one of the key responsibilities in calibrating the *STIX* imaging system represents the characterization of its grid pairs, in order to account for the effects from possible deviations of grid parameters from their nominal values. This analysis will be the focus of the following sections.

2.2 *STIX* grids calibration

In the following sections, a method for calibration and characterization of the *STIX* grids, including both the optical and X-ray part, is described. It is important to note that the two approaches are complementary and both necessary to obtain all the required parameters. The optical measurements provide details about all the geometrical (surface) properties, except the slit width. On the other

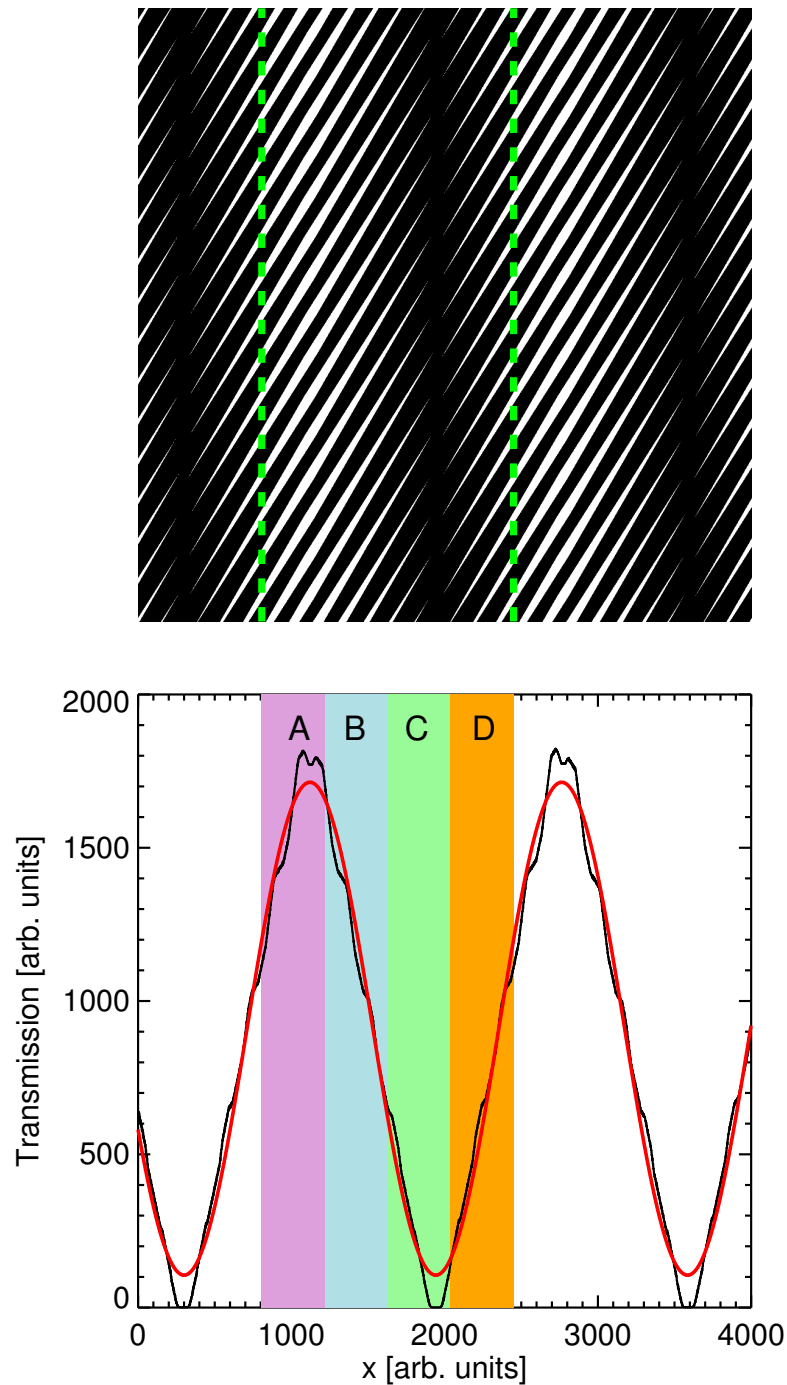


Figure 2.6: *Top:* Two grids with slightly different orientations and periods produce moiré modulation along the x -axis. In *STIX*, grids are designed so that the period of the moiré pattern equals the detector width, highlighted with green vertical lines. *Bottom:* The distribution of the transmitted light shows both the high- and low-frequency components (black). In practice, only the low-frequency component, or moiré, can be detected (red). *STIX* detectors sample the transmitted distribution in four pixels, highlighted with pale purple, blue, green and orange.

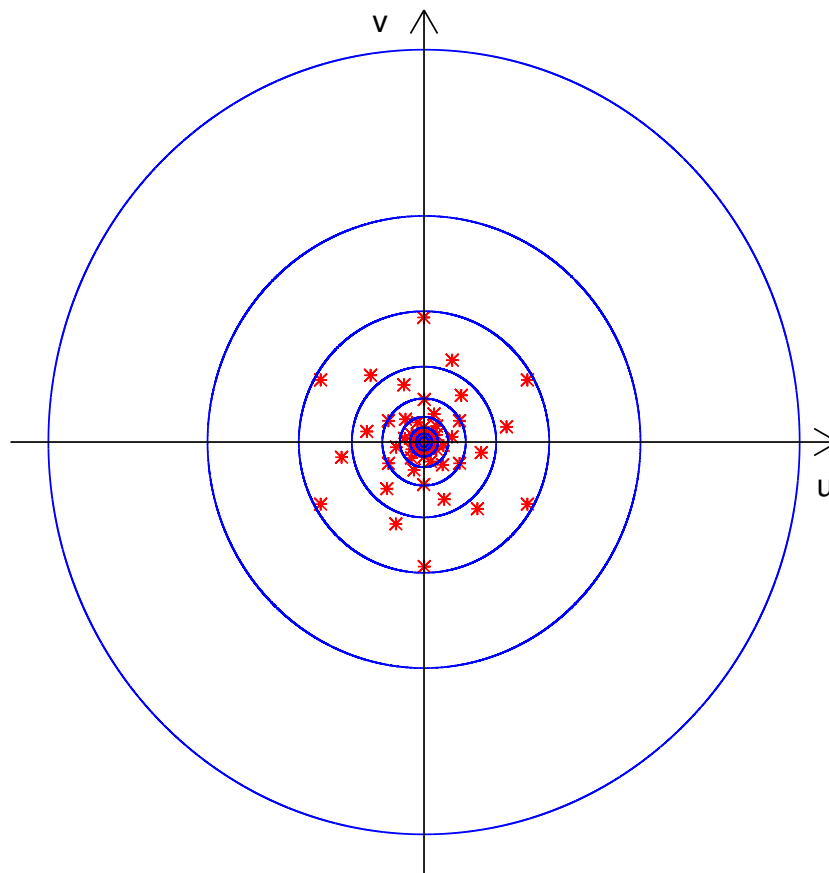


Figure 2.7: Sampling of Fourier components by *STIX* (red) and *RHESSI* (blue) at the same distance from the Sun (1 AU).

hand, through the analysis of X-ray transmission profiles of *STIX* grids in dependence on the incidence angle, the slit width can be obtained within the required tolerances. Since these measurements require detailed knowledge of other grid parameters determined in the optical analysis, the latter is described first.

There are two main steps in both the optical and X-ray characterization of *STIX* grids: obtaining the data and their analysis. Diego Casadei, the *STIX* technical coordinator at FHNW (2012–2018) and a senior scientist at Cosylab (2018–) was in charge of planning the observations and performing them at the clean room (optical) and synchrotron beam facilities (X-ray) at the Paul Scherrer Institute (PSI) in Villigen, Switzerland. The author helped by acquiring the data and developing the data analysis procedures, for both the optical and X-ray part. As already mentioned at the start of the chapter, main emphasis will be given on the method of extracting the grid parameters; final results will be reported in a later publication and the analysis report.

2.2.1 Optical characterization

The optical characterization was performed with a Mitutoyo QuickVision 302 equipment in a clean room facility at PSI. Because window/grid (the terms are used interchangeably throughout the text) sizes are not the same for front and rear segments, different number of images were taken for each. The motivation was to acquire images across the whole window, for both front and rear segments, in order to make as precise estimates of the needed parameters as possible, and to gain detailed information about their possible deviations in different sections of each window. In total, $21 \times 17 = 357$ images of each front window and $14 \times 11 = 154$ images of each rear window were taken; in Figure 2.8 a sequence for a front segment window is shown. The field-of-view was $1.251 \times 0.938 \text{ mm}^2$, with the pixel size of $1.955 \mu\text{m}$. Each image is saved as a data array of 640×480 points, together with the corresponding logbook file, containing the data on coordinates of each image's center and pixel size. This allowed for converting the images from pixels to physical coordinates and combining them into mosaics.

Window 11, Front Grid

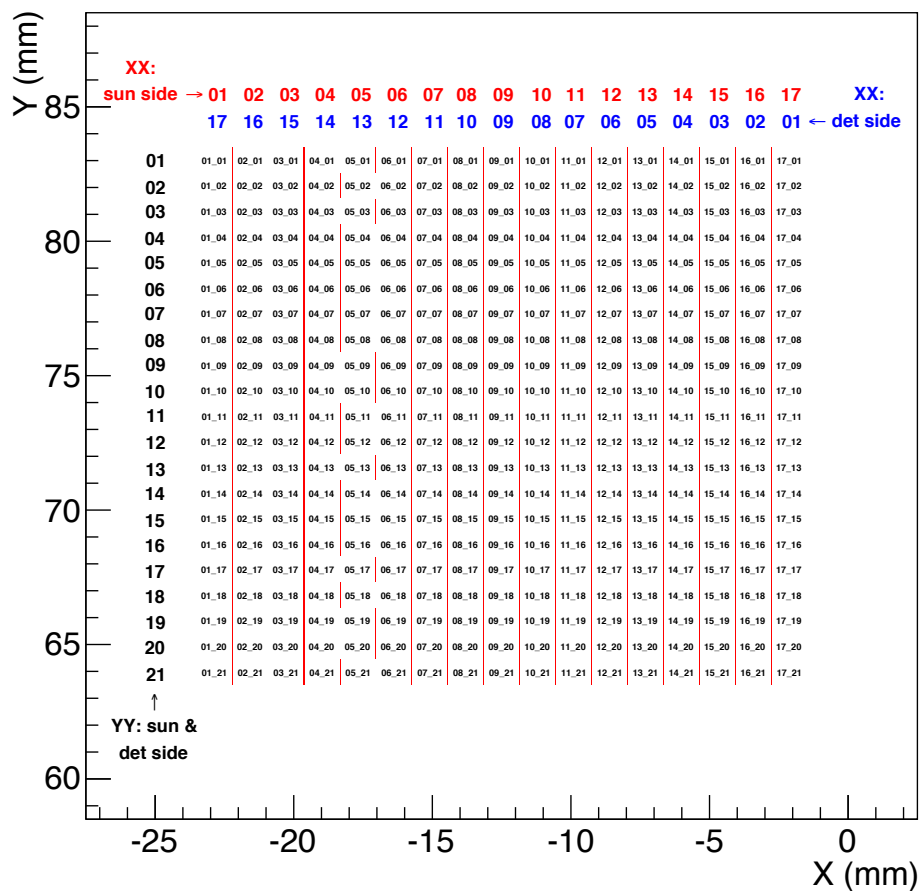


Figure 2.8: Measurement sequence for the front segment. Window 11 is taken as an example.

In the following sections, we describe the optical analysis in more detail. We start with the description of single-image analysis in Section 2.2.1.1. The steps of obtaining the mosaic image from single images are described in Section 2.2.1.2. The procedure of extracting grid parameters from the mosaics is described in Sections 2.2.1.3–2.2.1.6. The analysis is explained on the example of Flight Module (FM) window 8, front grid, or shortly window 8 in the remainder of the chapter.

2.2.1.1 Single image analysis

Figure 2.9 shows the steps of the single-image analysis. The original optical image (panel *a*) with the field-of-view (FoV) of $1.251 \times 0.938 \text{ mm}^2$ shows a small section of window 8, together with the coordinates defined by the fiducial grommets installed on the grid and retrieved from the logbook file. The thin structure running approximately perpendicular to slits is a bridge. Bridges are added to most windows to improve their mechanical stability and robustness against vibrations during the launch and other stresses.

There are a number of parameters to be retrieved from the data, the most important being: orientation, period, slit width (to be determined from the X-ray analysis), phase and bridge width. Additionally, RMS deviation and gradient of slit width across the window need to be determined. All of these parameters affect visibility measurements, either through their effect on amplitude determination, phase determination, or both.

The grid period is defined as the distance between two adjacent slits (or slats, see Figure 2.4). Grid orientation and period can be determined once the locations of rising and falling slit edges are found. We find the edges from intensity profiles of each row/column in a given image. Depending on the orientation angle, we scan through rows/columns in an image such that we maximize the precision in determining edges. For example, if we would scan rows in images of windows with horizontal slits such as window 20, we would not be able to find edge pixels. One intensity profile, for the row depicted by the dashed line in panel *a*, can be found in panel *b* of the same figure. This is a back-illuminated image, so the slit pixels have higher intensities (appear as white) than the slat pixels and bridges (appear as black). We find a rising edge as the first slit pixel which has an intensity larger than the sum of average slat intensity and 10 standard deviations of slat pixels. The factor of 10 was taken as the standard deviation of slat pixels is very small. Similarly, a falling edge is described as the last pixel on the “other side”, with the intensity still above the sum above. Falling and rising pixels are marked in orange and purple in panel *b*. This is repeated for all rows in each image, and all edge pixels are saved. Panel *c* shows the original image with edges found with the above procedure highlighted in purple and orange.

Bridges represent a problem since they add pixels which would compromise the fit quality. To minimize their effect, we rotate all edge pixels by the nominal orientation angle, which results in an image with almost perfectly vertical slits and slats, as shown in panel *d*. The histogram distribution of coordinates projected on the *y*-axis is shown in panel *e*, where a parabolic fit to the distribution is

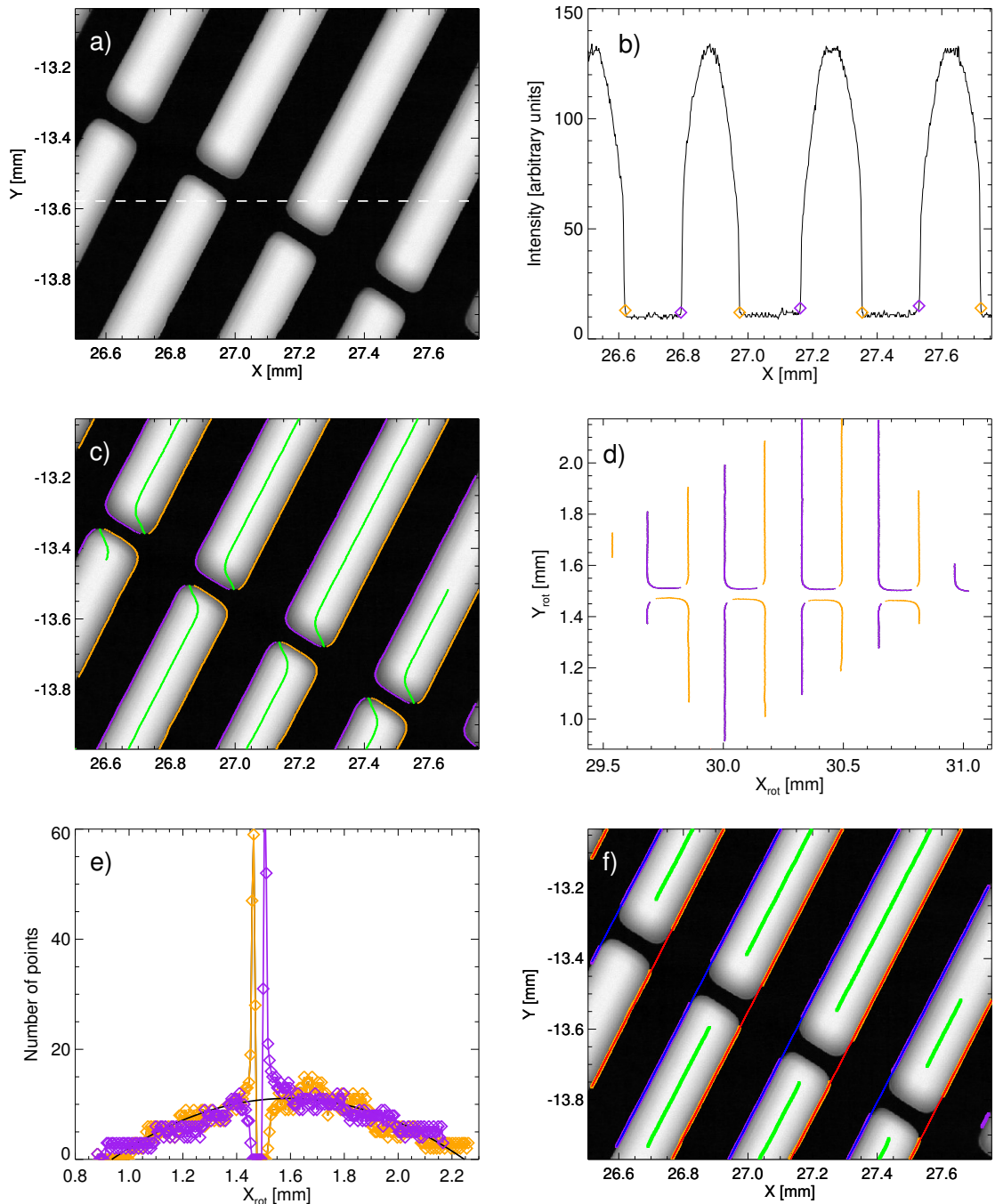


Figure 2.9: Steps of the single-image analysis. *a)* Original image of a part of window 8. *b)* Intensity profile of the row shown by the white dashed line in the previous panel. Edge pixels are shown in purple and orange. *c)* Image with rising and falling edges overplotted in purple and orange, respectively, and slit centers overplotted in green. *d)* Rotated edge-image used for determining bridge location. *e)* Projection of the rotated edge-image on the y -axis. *f)* Original image with edges and slit centers overlaid in orange, purple and green. The bridges are omitted in order to obtain the fits shown in red and blue.

performed. The location of bridge(s) is recognized as the clear peak above the fit, and saved for the future analysis.

We remove pixels affected by the bridge by deleting all edges within 50 pixels around this peak. This corresponds to a region ~ 2 times wider than the actual bridge width (nominal value 50 μm or ~ 25 pixels). We took this value because the above procedure detects the start (or end) of the bridge and not its centre and because bridges are recognised effectively in every image, with a minimum loss of data. Finally, all pixels representing rising (falling) edges are clustered based on their distances from other clusters, and only clusters containing > 20 points are saved. This removes false detections in the majority of cases. We also save pixels corresponding to slit centers, because they are important for determining grid phase in the later analysis. They are shown in green.

The original image with rising/falling edge pixels and slit centers without bridges is shown in panel *f*. These pixels will be used for the subsequent analysis and combined into mosaic images of individual windows.

2.2.1.2 Mosaics

Edge pixels from individual images are combined to make the mosaic of each window. An example of such a mosaic is shown in Figure 2.10 for window 8 (only rising edges are shown). The omitted bridges appear as interruptions perpendicular to the grids.

Once we obtain the mosaic of rising and falling edges, we rotate it by the nominal angle in order to make the edges vertical (same as in the single-image analysis). This allows us to cluster all pixels belonging to the same edge and fit them. The distribution of horizontal coordinates of the rotated mosaic image is shown in Figure 2.11. The clusters of rising and falling edge pixels are shown in red and blue.

2.2.1.3 Orientation angles

Depending on the slit width of the analysed window, there are between ~ 20 and ~ 250 rising/falling edges in a mosaic. The average position of each rising/falling edge cluster is calculated, and only the points within this pixel are considered for the final fits. Even though we reject many points, this approach leads to more precise estimates of orientation angles. This is due to asymmetries between rising and falling edges as the camera moves across the window (same edge appears sharper or blurrier in different images). Additionally, the same edge can sometimes be differently illuminated in images across the mosaic, which also leads to discontinuous points belonging to the same edge. This is why we chose to fit only one bundle of continuous points, in order to get as precise measurement as possible.

The clusters are rotated back by the nominal angle to reconstruct the original mosaic, and continuous points within each bundle are fitted with a straight line. The slope of each line determines the orientation of that edge, and the fitting is repeated for all edges. The distribution of the fitted angles is shown in

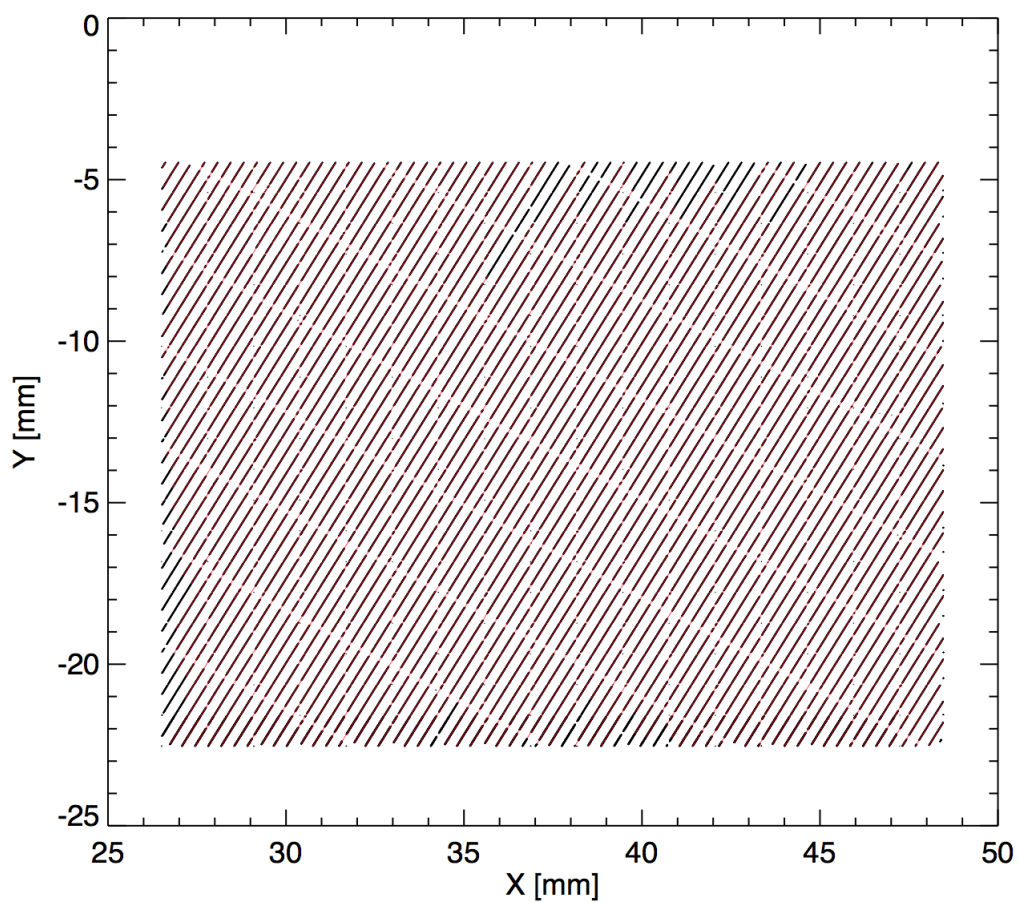


Figure 2.10: Mosaic of FM window 8, front grid.

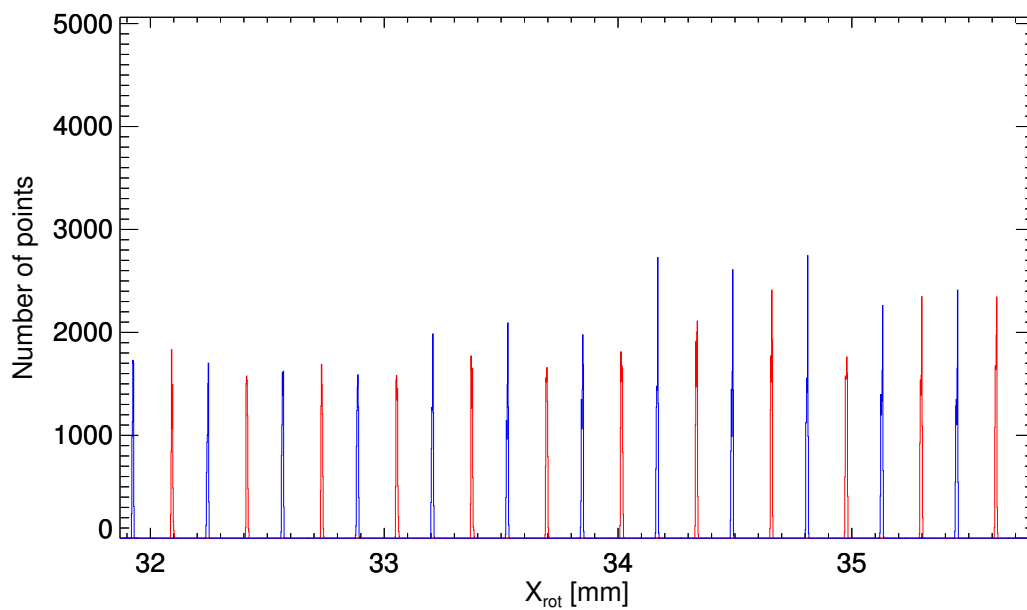


Figure 2.11: Clusters of rising (red) and falling edges (blue) in the rotated image.

Figure 2.12 for rising and falling edges, as well as slit centers, in pink, grey, and yellow, respectively, together with the gaussian fits. The fits give the values of $(150.526 \pm 0.001)^\circ$, $(150.526 \pm 0.002)^\circ$ and $(150.528 \pm 0.002)^\circ$ for the orientation angle of window 8. For reference, the nominal value of the orientation and its tolerance are overlaid with red vertical lines. In the later analysis, we will use the value determined from slit centers as the measured orientation.

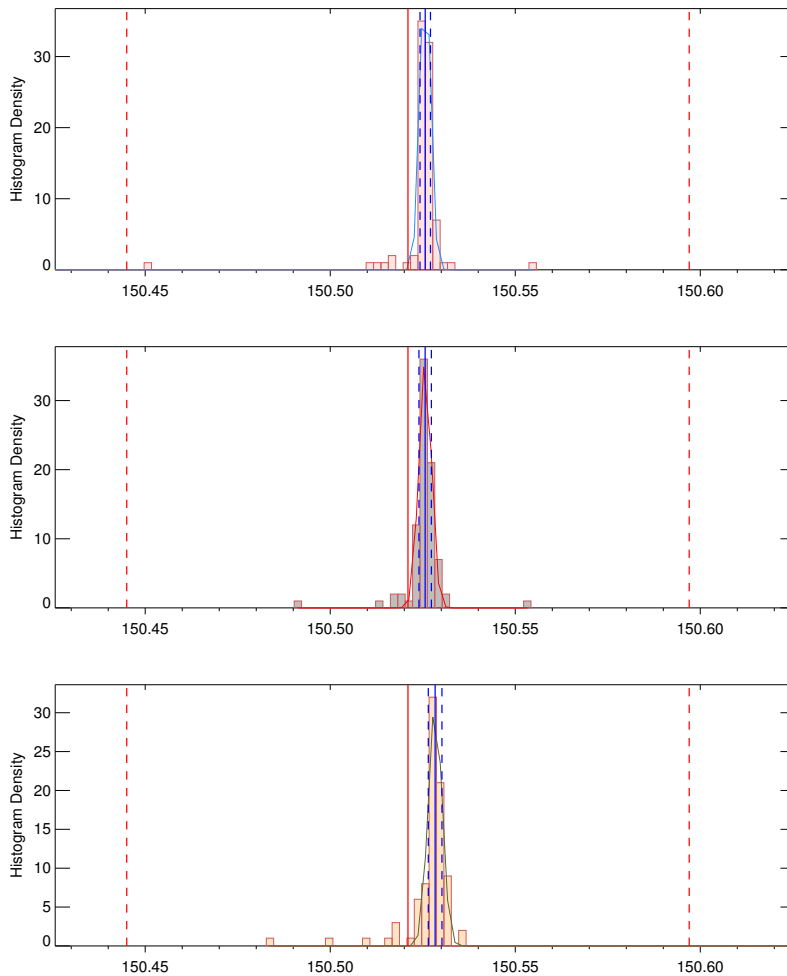


Figure 2.12: Distribution of orientation angles from mosaic fits for rising (top row), falling (middle row) edges, as well as slit centers (bottom row). The gaussian fits are also shown. The nominal value and its tolerance is depicted with red vertical lines.

2.2.1.4 Periods

Periods can be found from distances between clusters in the rotated mosaic image, where we rotate the original mosaic by the fitted value of the orientation, and not the nominal. This produces an image almost identical to Figure 2.11, because the difference between measured and nominal orientation is generally very small. Next, the position of each cluster in the rotated image is found as the po-

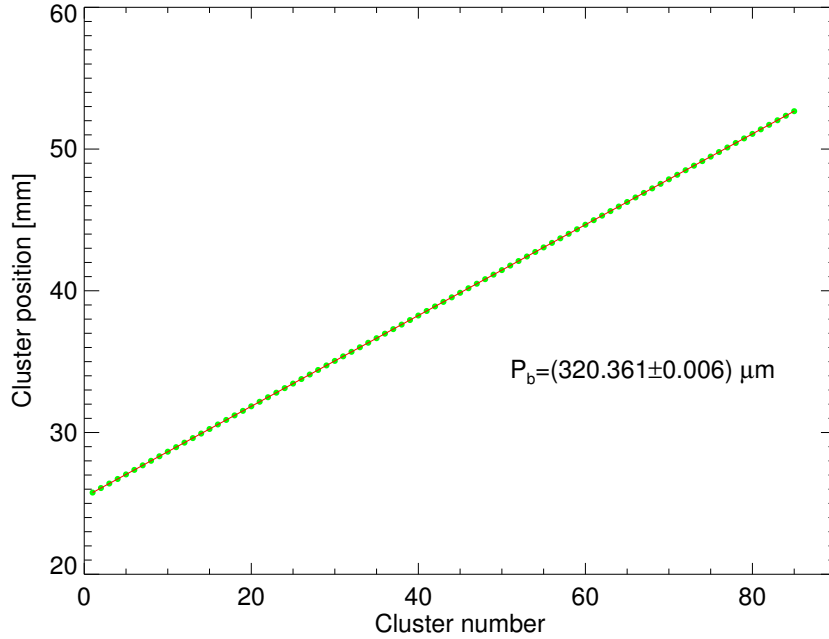


Figure 2.13: Cluster position in the rotated mosaic vs. cluster number. The slope of the fit gives the period. Both clusters of rising and falling edges are shown.

sition of the gaussian peak fitting the distribution of the given cluster. Distances between clusters define the grid period, a value which can be inferred by fitting cluster positions versus their distances in units of the nominal period (called cluster number). Such a plot is presented in Figure 2.13, again taking window 8 as an example. Here, we infer the period from the distances between slit centers and not the edges, since this is the value important for the visibility measurements. The measured period is equal to $(320.361 \pm 0.006) \mu\text{m}$.

2.2.1.5 Phases

The phase of any given grid is determined as follows; see also Figure 2.14. The line of zero phase goes through some reference/zero point at the angle equal to orientation of a given grid (black dashed line passing through the center). In the case of our measurements, zero point is defined as the center of the circular structure holding the grids, in the coordinate system (purple) as defined by the optical equipment. The displacement of one slit center in the bolded window is marked with the orange arrow and denoted with D . The next slit center further away would have the displacement $D + P$; see also a zoomed-in image of the window in the right panel. Therefore, we can uniquely define the grid phase by calculating distances of slit center lines from the origin modulo period. In practice, this value is inferred from rotated mosaics (with slit centers vertical). The position of each cluster is found by fitting the gaussian profile and calculating the peak. The position of each cluster peak modulo grating period gives an estimate of the grating phase. We find the grating phase for the whole window either by fitting the

distribution of the calculated values (in the case of enough clusters in the mosaic, i.e. grids with smaller periods) or by averaging. The phase for this window is equal to $(292.6 \pm 1.3) \mu\text{m}$.

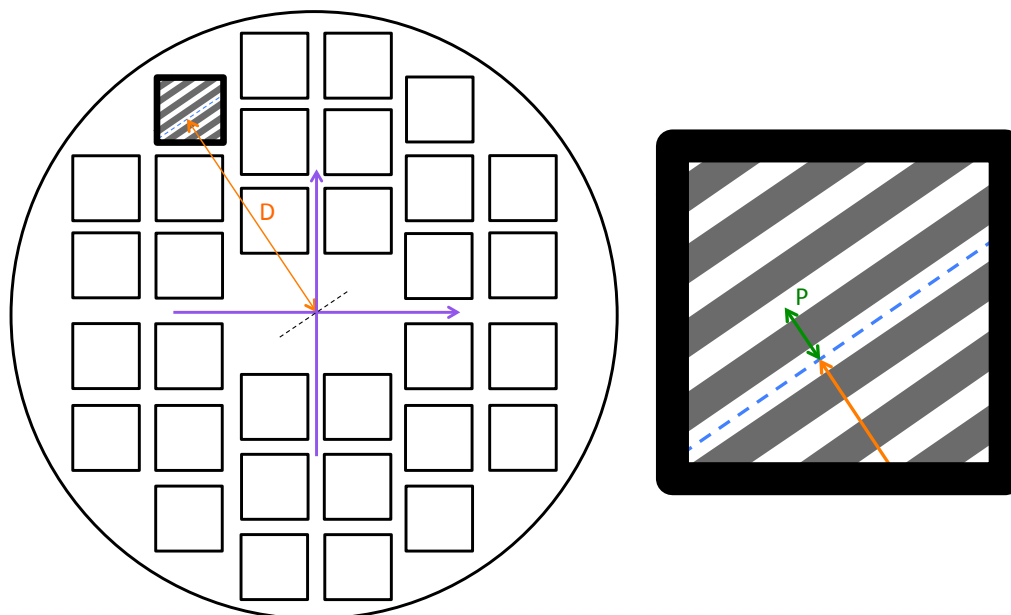


Figure 2.14: *Left:* Circular structure holding the *STIX* grids, together with the coordinate system denoted in purple. Bolded window is taken as a schematic example for phase calculation. Distance of a single slit center to a line passing through a reference point at zero phase is marked in orange and denoted by D . The phase of that slit center is given by D modulo period P . *Right:* Zoomed-in image of the bolded window.

2.2.1.6 Bridges

Bridges are additional tungsten structures added to some grids in order to improve their mechanical stability and reduce the risk of potential damages during the launch. The addition of bridges to the grid structure decreases the total transmission of the grid. This effect is relatively small as the area covered by bridges is small for all windows (there are only 9 bridge structures in the case of window 8, see Figure 2.10). Therefore, the knowledge requirement for this parameter is the least stringent of all parameters discussed so far, as it has a relatively weak influence on visibility measurements.

Bridges are determined in the following way. We determine black and white pixels in an image using the same threshold as before, which leads to the binary image containing only white and black pixels. White pixels represent slits, while dark pixels represent slats and bridges. An example is given in the left panel of Figure 2.15. This image is then rotated to make slits vertical, and all dark pixels are projected on the rotated x -axis. This leads to the distribution such as shown

in the middle panel. The derivative of this distribution is taken to determine positions of edges (red). One should note how the bridges are represented in this distribution; if there were no bridges, the number of dark pixels along the slits should decrease to zero. When this is not the case, it is the indication of the presence of a bridge. Bridge pixels in this distribution are marked with green and overlaid on the original image (right panel). The number of bridge pixels is taken as the total number of dark pixels along the slits. This number is saved for each image, and divided by the total number of pixels in an image ($640 \times 480 = 307200$). The same procedure is repeated for all images in a mosaic, and the total decrease of the transmission due to bridges is taken as the sum of all bridge pixels in all images, divided by the total number of pixels in all images. In this example, the decrease of the total transmission due to bridges is estimated at 0.92%.

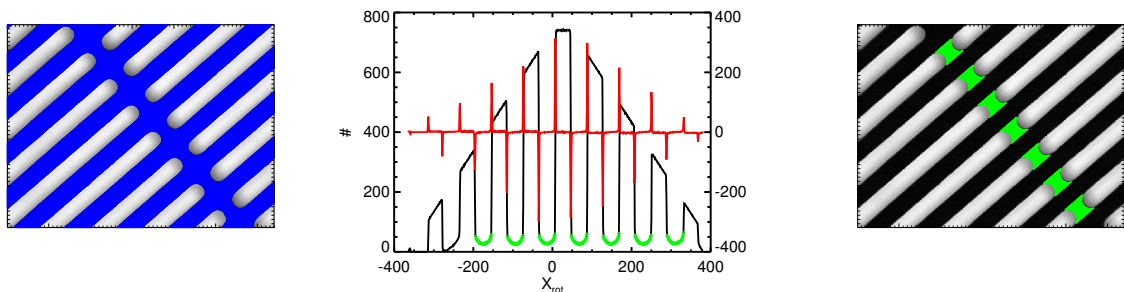


Figure 2.15: Finding bridges in individual optical images of STIX grids. *Left:* Dark pixels are found in the image and marked with blue. *Middle:* The image is rotated, and the number of all dark pixels of the rotated image is projected onto the x -axis. This results in a histogram distribution shown with black. Derivative of this distribution (red) shows locations of edges. Dark points where slats should be (between maxima and minima in derivative space) represent bridges and are overlaid in green. *Right:* Bridge pixels are shown in green in the original image.

2.2.2 X-ray characterization

Even though the optical analysis provides information on geometrical properties like period, orientation etc., X-ray analysis is needed in order to obtain the effective slit width, a missing piece of information lacking in the optical characterization. The main motivation for calculating it from X-ray images lies in the better precision that can be obtained (sharper edges and consistent illumination). Slit width is calculated from the transmission profile of a grid as a function of the incidence/tilt angle. The incidence angle of incoming photons is defined in the plane defined by the normal of the grid plane and the vector orthogonal to the slits. This is crucial for the later analysis of moiré patterns, as the amplitude of the transmission is dependent on the incidence angle. In the case of perfect grids and the slit/slat ratio of 1 (slits and slats of equal widths), the transmission profile as a function of the tilt angle would follow a triangular distribution with maximum intensity of 0.5 and minimum of zero. There are two parameters that affect the

intensity and shape of the triangular profile. The slit/slat ratio determines the transmission intensity, while the slit/(grid thickness) ratio determines the shape of the distribution. Because all grids have approximately the same thickness, coarser grids have broader distributions, as larger incidence angles are required for the transmission to go to zero (the condition is $\sin(\alpha) = s/H$, where s is slit width and H is grid thickness).

The flight model (FM) and flight spare (FS) front and rear *STIX* grids have been tested with the 15 keV synchrotron beam at the TOMCAT² facility at PSI. The measurements for the FM and FS were performed on 2016 February 8 and March 11, respectively (Casadei 2016b). The pixel size was $1.625 \mu\text{m}$. Due to the danger from radiation of the X-ray beam, a robotic setup such as shown in Figure 2.16 was used for positioning and rotating the *STIX* grids during the measurements. The grids were installed on the bar in front of the Faulhaber motor (they are partially transparent on the same figure). The transmitted X-ray beam is recorded by a camera behind this setup.

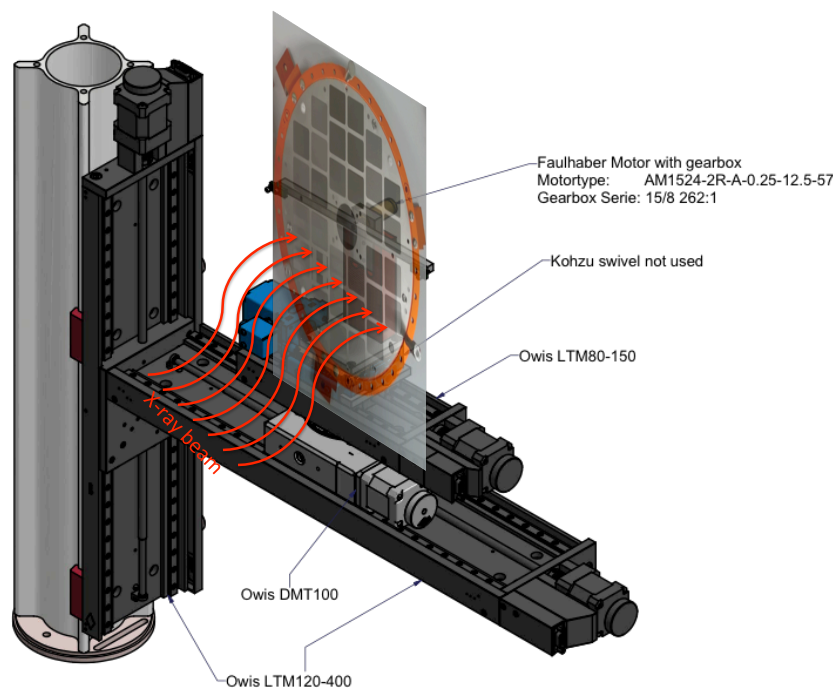


Figure 2.16: TOMCAT setup used for performing X-ray measurements of *STIX* grids.

The automatic window characterization procedure took X-ray images of the five regions shown in Figure 2.17 at the tilt angles about the vertical axis in the range $[-10, 10]^\circ$ (some points are sampled more than once). Even though the important incidence angle range for *STIX* is $[-1, 1]^\circ$, a wider sampling has been used in order to obtain better estimates of slit width and more complete transmission profiles. This resulted in 29 images for each region within the window, giving a total of 145 images for each window. Images, basically 2560×2160 (2D) arrays of transmitted X-ray intensities, were saved as *.tiff* files on a hard disk at the facility

² <https://www.psi.ch/sls/tomcat/>

and distributed to the members of the *STIX* team. These files are used as an input to the X-ray characterization procedure described in the following sections.

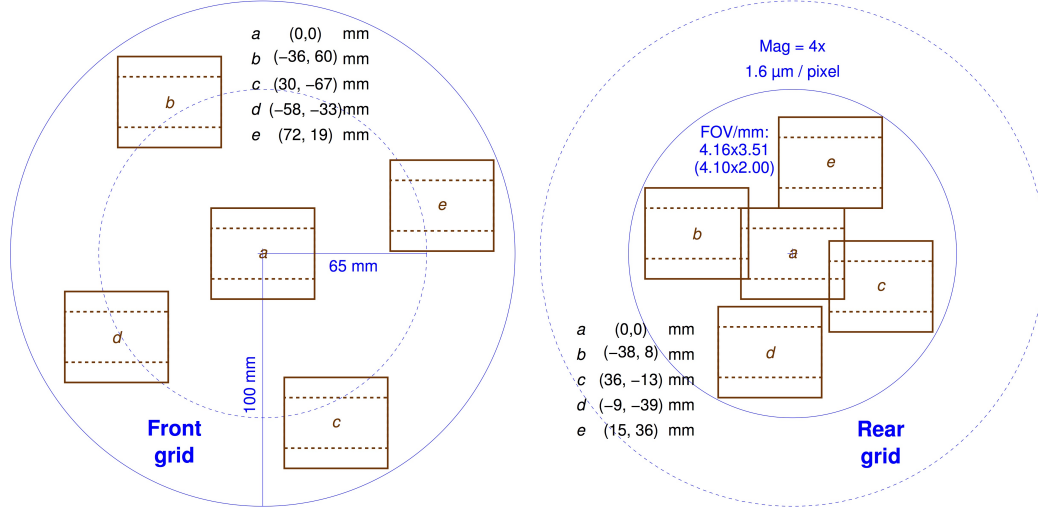


Figure 2.17: Five targeted regions in the case of front (*left*) and rear (*right*) grids.

2.2.2.1 Different approaches in calculating the X-ray transmission

All windows, apart from 11, 12, 13, 17, 18, 19, are built as a single stack of etched tungsten layers. The transmission profiles of finer windows made of two or three layers are more complicated and will be described later. In order to make our analysis as robust as possible and to understand the data, we take into account three possible approaches to calculating the X-ray transmission from images:

1. **Black/White:** In this approach, we calculate the mean intensity of all the pixels in an image. All pixels with intensity above this value are considered as white (with intensity 1) and all pixels with intensity below the mean value as black (with intensity 0). This leads to the binary image, consisting of pixels with intensities 0 or 1, where the transmission is equal to $T = N_w / N_{tot}$. Here, N_w is the total number of white pixels and N_{tot} the total number of pixels in the image.
2. **Brightness corrected:** Here we rely on the dark and bright flat-field images taken at the start of observing runs and use them to make the linear transformation of pixels in the observed images, i.e. $i = (m - b) / (w - b)$, where i is the intensity of a pixel in the 'corrected' image, m is the measured intensity and b and w are intensities of the same pixel in the dark and bright flat-field images. This leads to pixels in 'scaled' images having intensity between 0 and 1. The X-ray transmission in an image is then described by the mean intensity of all pixels.
3. **Duty cycle:** This approach uses a different way for calculating the intensity, such that the total transmission is defined as the ratio of the apparent

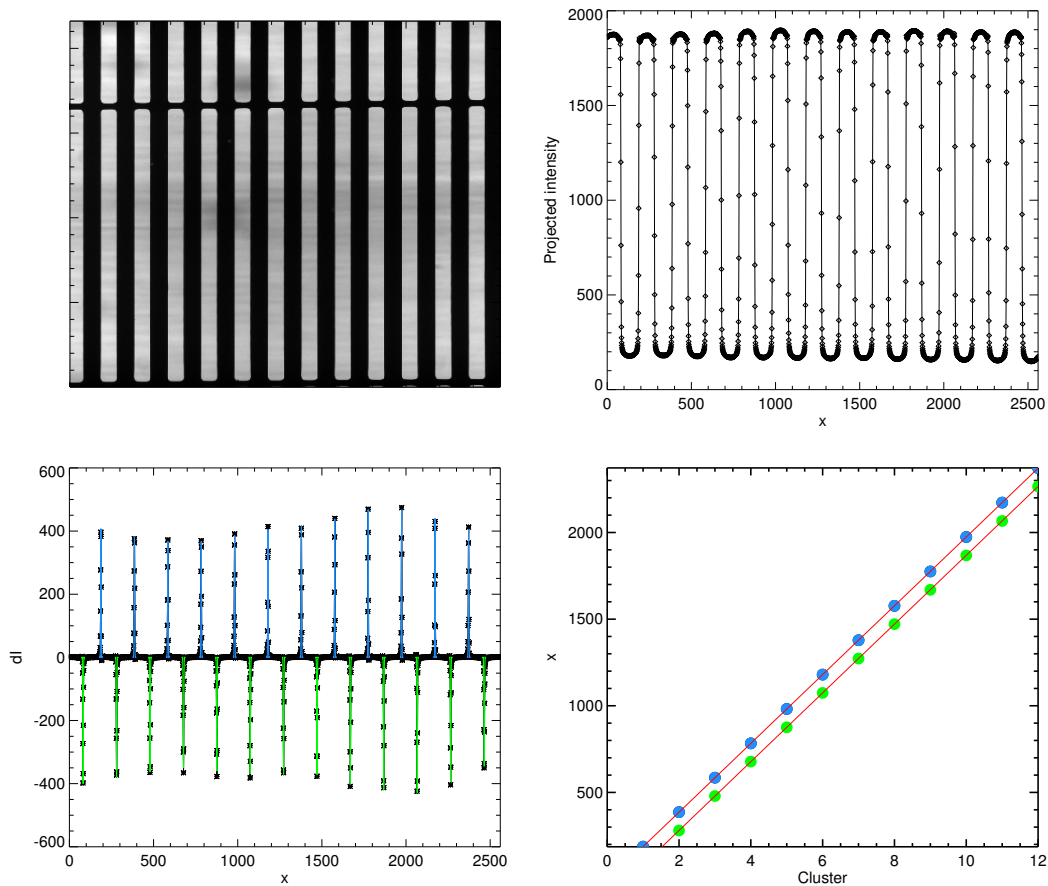


Figure 2.18: Steps of calculating the transmission in the ‘duty cycle’ approach. *Top:* Image of a part of window 8 (left) and the projected intensity on the x -axis (right). *Bottom:* Edges are represented by gaussians of the intensity derivative (left). X-ray period is calculated by fitting the locations of rising (or falling) edges, similar to the optical case (right).

slit width and the period (in pixels) for each angle. In order to obtain slit widths and periods, we calculate the projected intensity of all pixels in an image on the horizontal axis; see top right panel of Figure 2.18. The derivative of this distribution has very sharp peaks at the locations of edges, which can be fitted with gaussian profiles showing highest intensity changes (bottom left). We define the edge position as the maximum of each gaussian distribution. Slit widths are calculated as differences between the consecutive rising and falling edges (defined by positive and negative gaussian peaks), while periods are defined as differences between two consecutive rising (or falling) edges. The slit width is then calculated as the average of all slit widths obtained this way, while the period is determined similarly to the optical case, by fitting each rising (falling) edge position with a straight line, where the slope represents the period (bottom right). Transmission is given by the ratio of the slit width and the period determined this way.

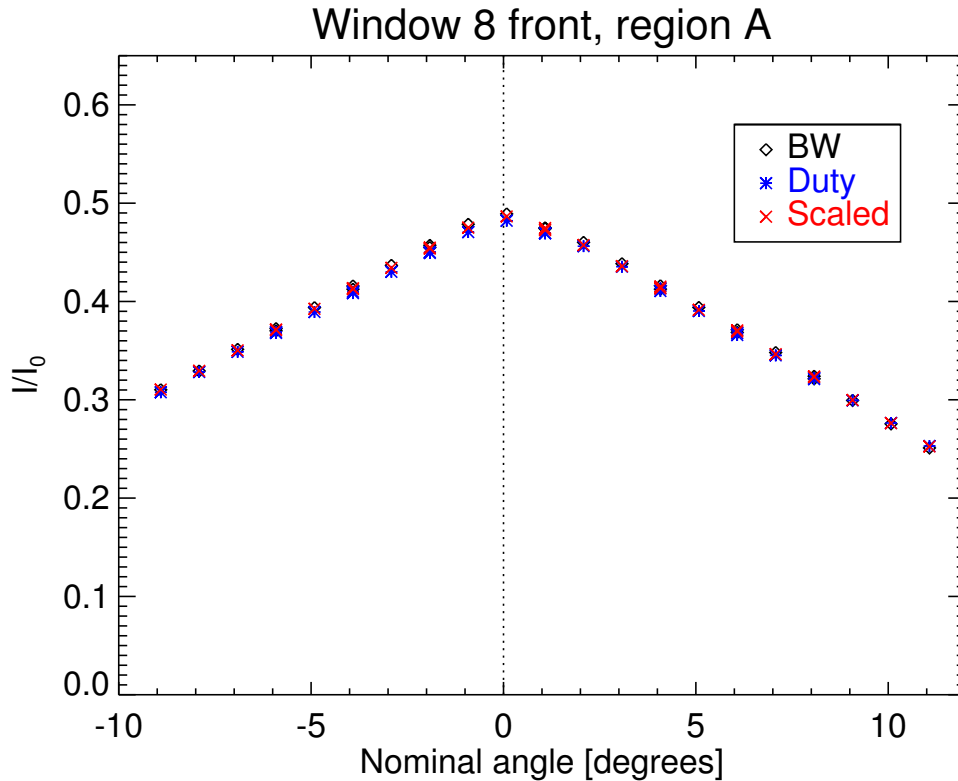


Figure 2.19: Transmission profile of window 8 front for three different approaches.

Transmission profiles of the three approaches are shown Figure 2.19 for comparison. In many cases such as this, all three approaches provide consistent results. However, the calculated transmission can be affected by features within the FoV. We note three possible influences on the transmission in images of different regions/windows:

Bridges: The first one is the presence of bridge(s) in the FoV. Bridges, as discussed before, improve the mechanical stability of grids. However, they affect the total transmission and, if not accounted for, could influence the calculation of slit width from the X-ray measurements. Specifically, bridges would be counted as black pixels in the first two approaches and systematically decrease the brightness (see the left panel of Figure 2.20).

Grid edges: The presence of grid edges within the FoV would also systematically decrease the brightness. During the measurements, the robotic setup performs many rotations and translations in order to target the desired regions in each window, sometimes leading to slight displacements. This can lead to grid edges appearing within the FoV, such as shown in the middle panel of Figure 2.20. This would again lead to overestimating black pixels in the first two approaches, but does not affect the third approach.

FoV: The third influence is important in the case of coarsest grids. The problem is that the $\text{FoV} \approx 4$ mm of our images includes only a very small number of slits/slats for those windows. When the tilt angle changes, different parts of

slits/slats come into the FoV, which also changes the transmission (see the right panel of Figure 2.20). This does not have a large influence for windows where the number of slits/slats within the FoV is large, but it is important in the case of their small numbers. Again, this effect would have influence in approaches 1 and 2, but would not affect the third approach, as it would only lead to one less data point used for averaging.

For all the reasons discussed above, we adopt the third approach for calculating transmission profiles. We note again that all approaches give consistent results in the case of no bridges/edges and for grids with small to moderate periods, but the third approach is more robust for the coarsest grids and in the case when bridges/edges are within the FoV.

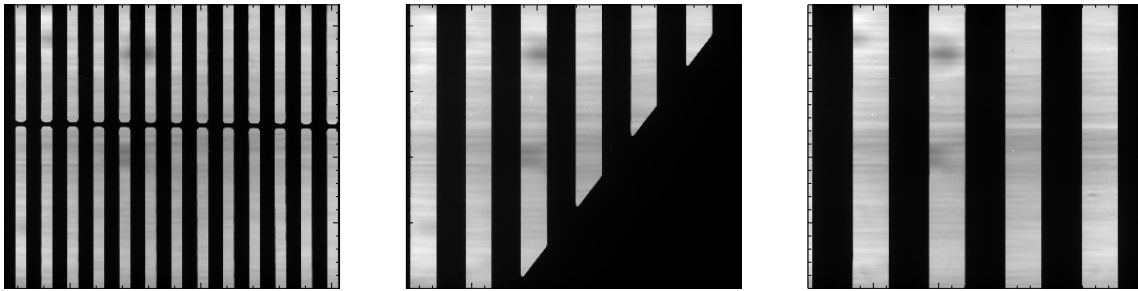


Figure 2.20: Three possible influences on the transmission profile. *Left:* Presence of bridges within the FoV. *Middle:* Presence of an edge within the FoV. *Right:* Slit/slat entering the FoV (important only for coarsest grids).

2.2.2.2 Calibration

We calculated the transmission profiles for all regions within each window as a function of the incidence angle. Such a profile, for all three approaches, is shown in the case of window 8 in Figure 2.19. Even though the nominal step in tilt angle is 1 degree, this is not well calibrated in our robotic setup. Therefore, this section will explain the steps of retrieving the absolute angular calibration of our X-ray measurements. Furthermore, the pixel size calibration will be also performed, using the known values of grid parameters from the optical analysis.

In order to retrieve the absolute calibration from our measurements, we plot the measured period as a function of the incidence angle. Such a profile is shown in Figure 2.21, for all five regions in the window. It shows a cosine profile well described with the formula:

$$P = A \cos(C\alpha - B), \quad (2.5)$$

where P is the observed period, A the maximum period, C the conversion between the nominal and true angular scale, α the angle in nominal degrees and B the origin. The ratio B/C determines the normal direction, where the period is maximal. Fits for all regions are overlaid in purple. We repeat this procedure for all regions and all windows, resulting in $24 \times 5 \times 2 = 240$ fits, where 24

stands for the number of single-layer windows, 5 denotes the number of regions in each window, while 2 represents front and rear grids. The fitting is successful in 227/240, or 95%, of cases. We average the successful fits for each window, resulting in a total of 24 fits for each grid, or 48 in total.

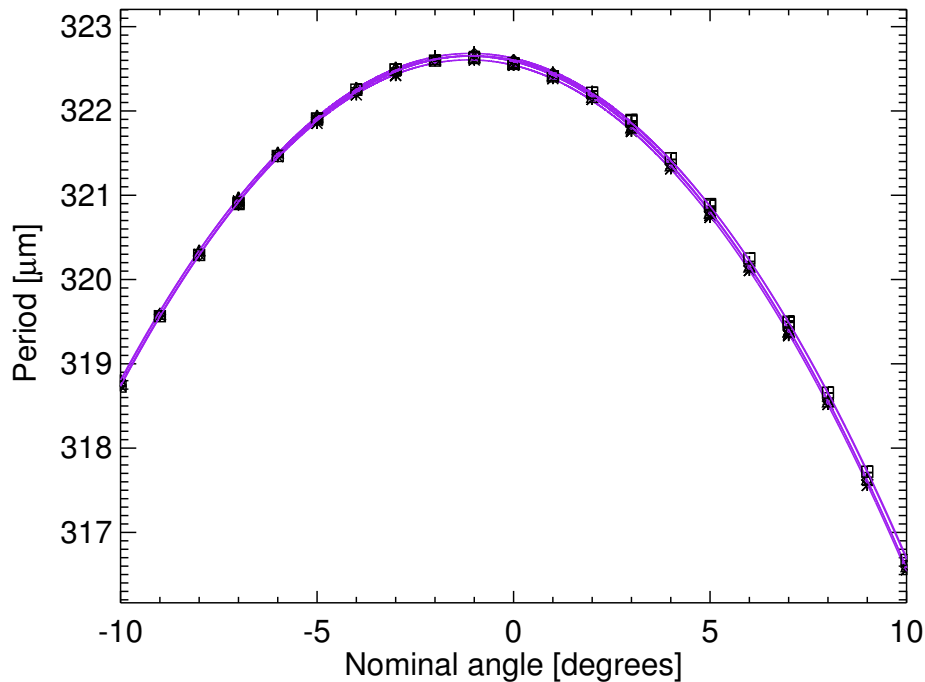


Figure 2.21: The observed period as a function of the tilt angle. The cosine fit is overlaid in purple.

We investigate how different variables of the above fit change as a function of the measurement step. The measurement step represents the order of measurement operations. For example, step 1 was taking flat-field images, step 8 was taking images of window 5, step 53 taking images of window 1, etc. This allows us to extract possible trends of parameters C and B as a function of step number. The top row of Figure 2.22 shows the conversion factor C between the nominal and calibrated angle as a function of the measurement step. There are no clear trends in either front nor rear segment. We conclude that this calibration is independent of the step number, and since the fluctuation is very small, we take the average of all measurements for the later analysis.

By calculating the maximum period A for each window, we can calibrate the pixel size in our X-ray measurements by comparing X-ray periods to their (precisely determined) values from the optical analysis. We plot the ratio of optical and X-ray period for each window as a function of measurement step in middle panels of Figure 2.22 for front and rear segments, respectively. Since we find no trends in front nor rear segment and no significant scatter either, we use the mean value of (0.9928 ± 0.0002) for the later analysis.

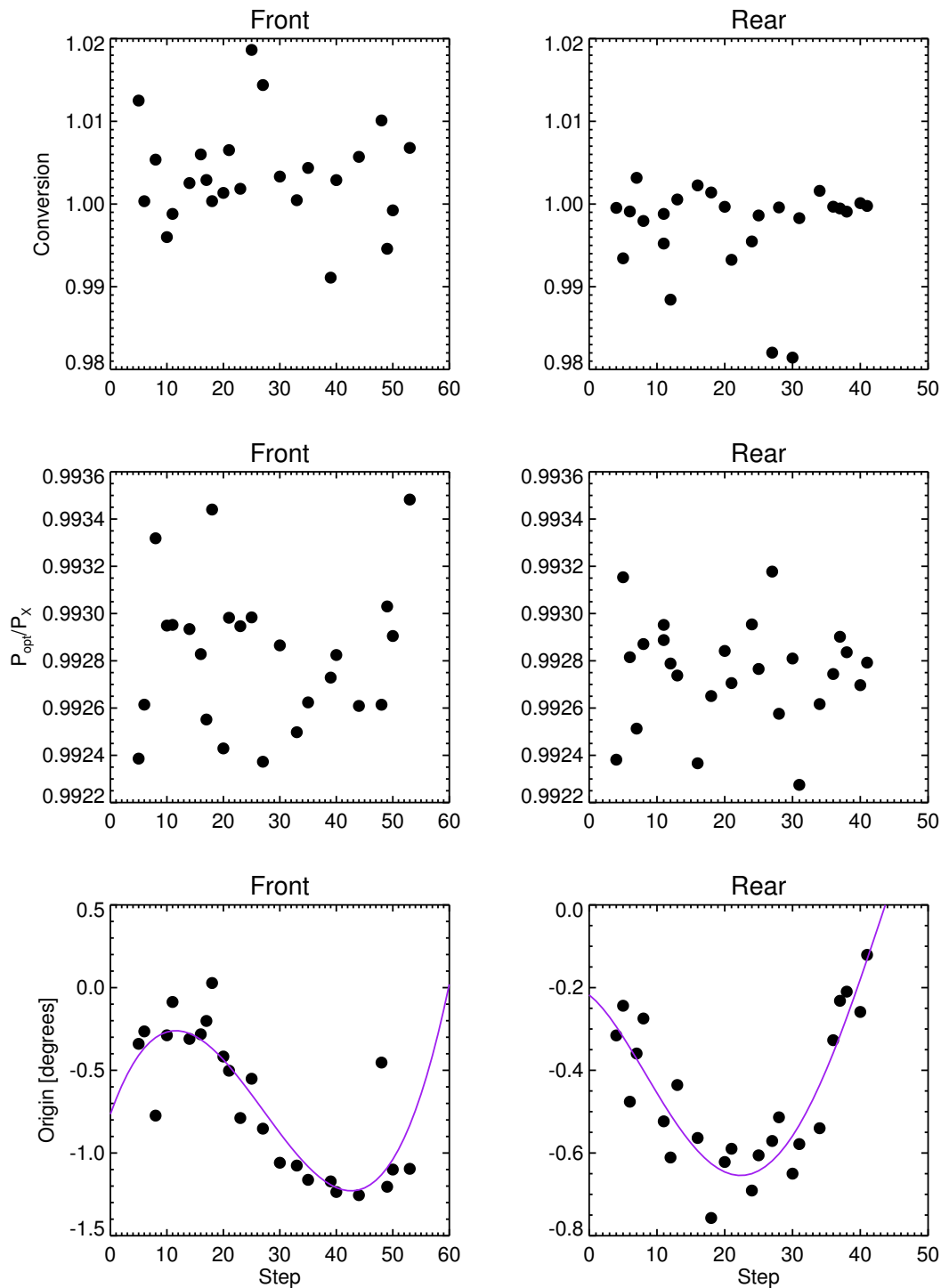


Figure 2.22: Fit parameters vs. measurement step. *Top:* Conversion factor between nominal and actual tilt angle. *Middle:* The ratio of periods from the optical and X-ray analysis determines the pixel scale of the X-ray measurement. *Bottom:* Displacement of origin. The behaviours for the front and rear segments are fitted with third and fourth degree polynomials, respectively.

In contrast to the above parameters, the origin B shows a trend when plotted as a function of the measurement step. It is probably caused by the not too rigid mechanical fixation of the remotely controlled robotic setup. The compromise was to make the fixation rigid enough for the automatic procedure to run without manual adjustments, while being safe (loose) enough for space hardware. The trend is plotted in bottom panels and shows different profiles for front and rear segments. We fit the front segment with the third degree polynomial, while the fourth degree polynomial represents the rear segment better. Because of the different trends, averaging results over all windows would not give reliable results. Therefore, we use the fit-determined values of B for each region separately for the later analysis.

With the above analysis, we obtained a precise pixel calibration and the actual incidence angle in our measurements.

2.2.2.3 Transmission profiles

With the knowledge on spatial and angular calibration of our measurements, we can plot the X-ray transmission as a function of the calibrated tilt angle. This is shown in Figure 2.23 for window 8 and five regions, using the duty cycle approach in calculating the transmission (given by the ratio of the slit width and the period). In the case of geometrical optics and no partial transmission, the transmission profile is defined by a triangular function. In practice, however, the observed transmission profiles show a triangular profile with a smoothed top, with a few percent lower transmission than in the case of a perfect triangle. Therefore, we simulate the grid behaviour with two approaches:

1. **Perfect triangle:** We fit the transmission profile with two independent straight-lines on each side of the maximum transmission.
2. **Smooth triangle:** We fit the continuous function to the measured values, consisting of two straight lines (with initial guesses of their parameters equal to the above approach) plus a parabolic fit to reproduce the smoothing at the top. This continuous function is described by the following formula:

$$f(\alpha) = \begin{cases} a\alpha + b & \alpha \leq \alpha_L \\ c\alpha^2 + d\alpha + g & \alpha_L \leq \alpha \leq \alpha_R \\ h\alpha + l & \alpha \geq \alpha_R \end{cases} \quad (2.6)$$

where α is the incidence angle. By imposing continuity and smoothness criteria on the above function at α_L and α_R , we obtain the following relations between the parameters:

$$\begin{aligned} a &= 2c\alpha_L + d \\ h &= 2c\alpha_R + d \\ g &= c\alpha_L^2 + b \\ l &= c\alpha_L^2 - c\alpha_R^2 + b. \end{aligned} \quad (2.7)$$

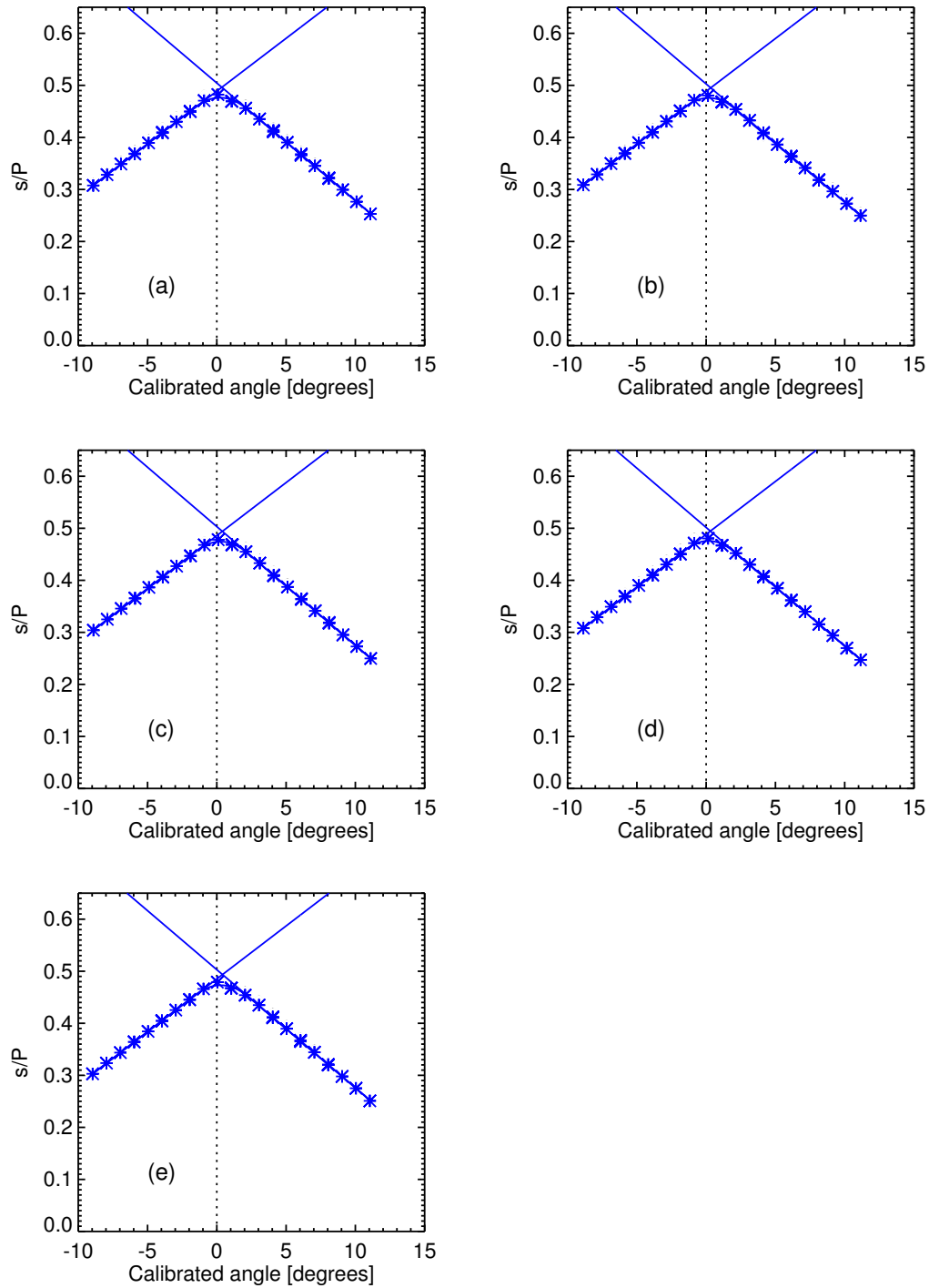


Figure 2.23: Transmission (slit to period ratio) vs. calibrated tilt angle for all regions of window 8.

The above relations reduce the number of free parameters to be obtained from the fits to five. Even though our procedure sometimes overestimates the transmission at the side lobes and thus reduces the number of observations taken into account for fitting, there are always more than 20 points to perform the fitting on, more than enough to precisely determine the above parameters.

We overlay both fits in panels *a-e* of Figure 2.23. It can be seen that they give consistent results, except at the top of the triangle. The following points are important for the later inclusion in *STIX* data analysis software: horizontal and vertical coordinates of the intersect of the two straight line fits, horizontal and vertical coordinates of the vertex of the continuous function and the intersect of the continuous function with the horizontal axis. The vertical coordinates of the intersect and the vertex can be used as the two independent approximations of the slit width, since the slit width is defined as their product with the period (the value can be taken from the optical measurement).

The third approach in calculating the slit width consists of plotting the slit width as a function of the tilt angle. The slit width is given by the product of its value in pixels (inferred from X-ray images) and the pixel- μm calibration constant determined before. The slit width is again described by a triangular distribution. We can fit this distribution with two straight lines, with their intersect providing the third estimate of the actual slit width. This value is equal $(158.8 \pm 0.3) \mu\text{m}$ and it is reported in Table 2.1, where we give estimates of all the parameters for window 8. All measured values in the table are rounded to the first digit of their respective uncertainties. For the comparison, also the nominal values for the grid parameters are given, together with their tolerances. All the measured values fall within the tolerance ranges, with only the slit width being at the edge of this range.

In summary, we have presented a method for extracting important grid parameters from the acquired data. This method is used to infer the parameters for other single-stack windows. This analysis will also be written as a *STIX* report, with all relevant values represented in a final grid parameter table, which will contain the above (and some additional) information for all grids. Furthermore, a publication about the method and *STIX* imaging system is also planned in collaboration with other members of the *STIX* team and before its launch in 2020.

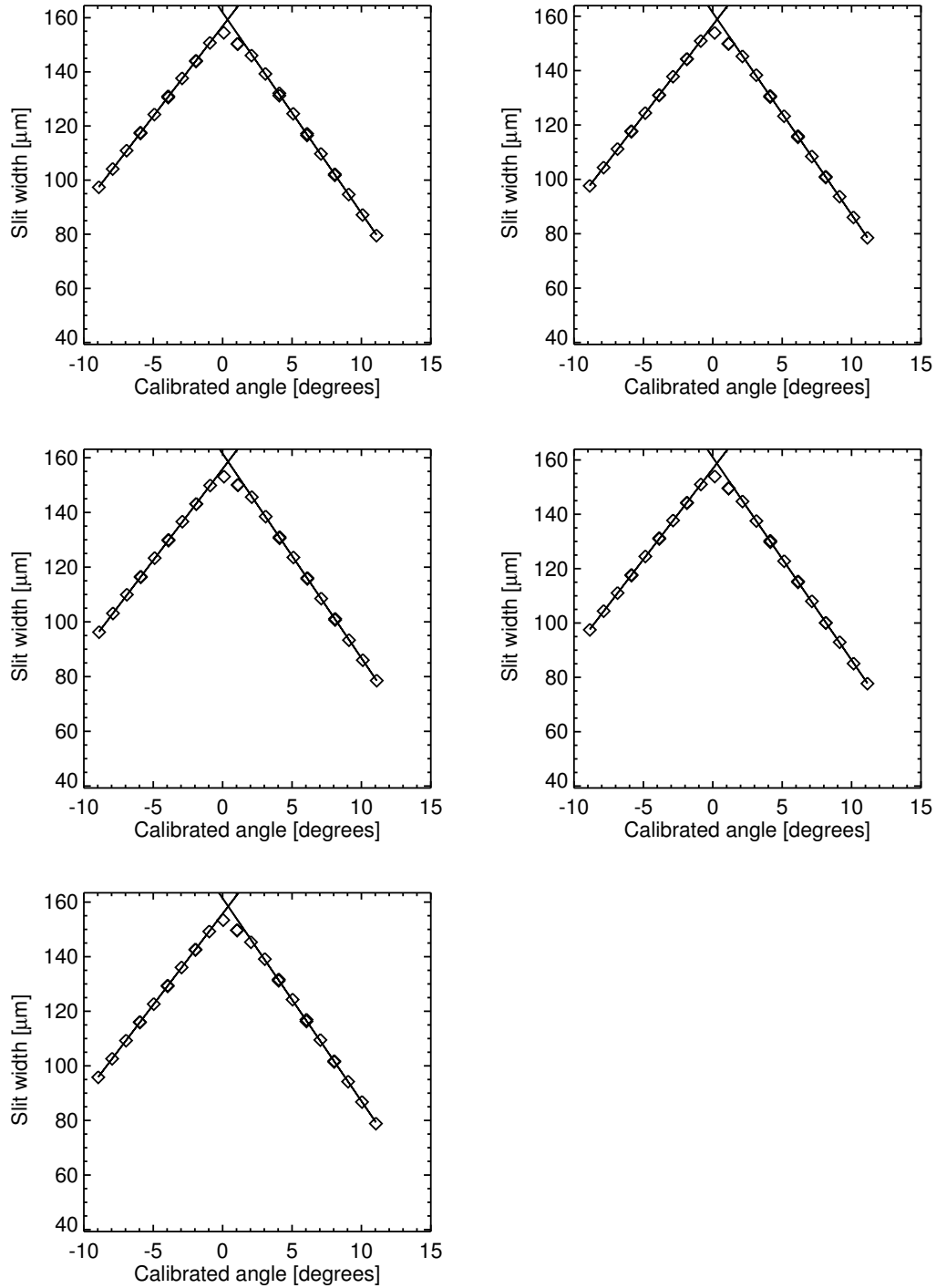


Figure 2.24: Calibrated slit width as a function of the calibrated tilt angle. The intersection gives an estimate of the maximum transmission and, therefore, slit width.

| Parameter | Measured value | Nominal value | Tolerance |
|------------------------|----------------|---------------|-----------|
| Orientation [°] | 150.528(2) | 150.521 | 0.076 |
| Period [μm] | 320.361(6) | 320.259 | 0.43 |
| Phase [μm] | 293(1) | N/A | N/A |
| Bridge effect [%] | 0.92 | N/A | N/A |
| Slit width [μm] | 158.8(3) | 166 | 8 |

Table 2.1: Grid parameters for window 8, front segment.

Bibliography

- Aschwanden, M. J., Schmahl, E., & RHESSI Team. 2002, *Sol. Phys.*, **210**, 193
- Casadei, D. 2014, in *2014 IEEE Nuclear Science Symposium and Medical Imaging Conference (NSS/MIC)*, 1–5
- Casadei, D. 2016a, STIX-LB-0106-FHNW
- Casadei, D. 2016b, STIX-TP-0103-FHNW
- Gabrielyan, E. 2007, *ArXiv Physics e-prints*, **0703098**
- Giordano, S., Pinamonti, N., Piana, M., & Massone, A. M. 2014, *ArXiv e-prints*, **14126825**
- Högbom, J. A. 1974, *A&AS*, **15**, 417
- Hurford, G. J., Schmahl, E. J., Schwartz, R. A., et al. 2002, *Sol. Phys.*, **210**, 61
- Lin, R. P., Dennis, B. R., & Benz, A. O., eds. 2003, *The Reuven Ramaty High-Energy Solar Spectroscopic Imager (RHESSI) - Mission Description and Early Results*
- Metcalf, T. R., Hudson, H. S., Kosugi, T., Puetter, R. C., & Pina, R. K. 1996, *ApJ*, **466**, 585
- Prince, T. A., Hurford, G. J., Hudson, H. S., & Crannell, C. J. 1988, *Sol. Phys.*, **118**, 269
- Sato, J., Kosugi, T., & Makishima, K. 1999, *PASJ*, **51**, 127

BIBLIOGRAPHY

Chapter 3

Correlation of hard X-ray and white light emission in solar flares*

Matej Kuhar^{1,2}, Säm Krucker^{1,3}, Juan Carlos Martínez Oliveros³, Marina Battaglia¹, Lucia Kleint¹, Diego Casadei¹, Hugh S. Hudson^{3,4}

Abstract

A statistical study of the correlation between hard X-ray and white light emission in solar flares is performed in order to search for a link between flare-accelerated electrons and white light formation. We analyze 43 flares spanning *GOES* classes M and X using observations from the *Reuven Ramaty High Energy Solar Spectroscopic Imager* and the Helioseismic and Magnetic Imager. We calculate X-ray fluxes at 30 keV and white light fluxes at 6173 Å summed over the hard X-ray flare ribbons using the HMI integration time of 45 seconds around the peak hard-X ray time. We find a good correlation between hard X-ray fluxes and excess white light fluxes, with a highest correlation coefficient of 0.68 for photons with energy of 30 keV. Assuming the thick target model, a similar correlation is found between the deposited power by flare-accelerated electrons and the white light fluxes. The correlation coefficient is found to be largest for energy deposition by electrons above ~ 50 keV. At higher electron energies the correlation decreases gradually while a rapid decrease is seen if the energy provided by low-energy electrons is added. This suggests that flare-accelerated electrons of energy ~ 50 keV are the main source for white light production.

3.1 Introduction

Solar flares are the most energetic phenomena on the Sun (e.g., Benz 2008). In a solar flare, large numbers of electrons, accelerated in the solar corona, precipitate

* This chapter has been published in *The Astrophysical Journal*, **816**, 6 (2016)

¹ University of Applied Sciences and Arts Northwestern Switzerland, Bahnhofstrasse 6, 5210 Windisch, Switzerland

² Institute for Particle Physics and Astrophysics, ETH Zürich, 8093 Zürich, Switzerland

³ Space Sciences Laboratory, University of California, Berkeley, CA 94720-7450, USA

⁴ School of Physics and Astronomy, University of Glasgow, Glasgow G12 8QQ, UK

to the lower layers of the solar atmosphere, where they deposit their energy in interactions with ambient gas. The energy is emitted over the whole electromagnetic spectrum, from radio waves to γ rays (e.g., Fletcher et al. 2011). Particularly interesting is the radiation in the white light (WL) range (visible continuum) because it contains a significant fraction of the total flare energy. The difficulty in detecting white light flares (WLFs) is that the enhancement in WL emission is relatively faint compared to the pre-flare level, typically ranging from a few percent up to several tens of percent in extreme cases. For more ordinary flares (below M5 GOES class), such a faint enhancement is generally lost in the temporal and spatial intensity fluctuations of the photosphere. For this reason, it was long believed that white light flares (WLFs) are rare and exotic phenomena; however, recent observations suggest that WL emission can be detected in flares as weak as GOES C1.6 (e.g., Hudson et al. 2006).

Many studies (e.g., Hudson 1972; Rust & Hegwer 1975; Chen & Ding 2005; 2006; Xu et al. 2014) have reported a close correlation in space and time between HXR and WL emissions, which is a strong indication of the connection between nonthermal electron beams and WL formation. There are two main mechanisms proposed for explaining the WL emission in solar flares: *direct heating* and *radiative back-warming*. In direct heating, the same electrons that produce HXR emission via bremsstrahlung locally heat and ionize the medium. The WL continuum emission is probably produced by the recombination of hydrogen. Recent studies indeed show WL and HXR sources originating from the same volume (Martínez Oliveros et al. 2012; Battaglia & Kontar 2012; Krucker et al. 2015). The problem of the direct heating model is that there are very few electrons (because of the steepness of the nonthermal electron spectrum) with sufficient energy to penetrate to the lower chromosphere and photosphere, at least in the standard thick-target model of HXR emission. In radiative back-warming, electrons are stopped in the upper chromosphere, where the UV continuum radiation is emitted, which heats the deeper layers and results in enhanced continuum emission (Aboudarham & Henoux 1986; Machado et al. 1989; Metcalf et al. 1990).

Generally, most of the previous studies on WLFs concentrated on individual events. In this paper, we analyze 43 WLFs spanning GOES classes M and X using observations with the *Reuven Ramaty High Energy Solar Spectroscopic Imager* (RHESSI, Lin et al. 2002) and the Helioseismic and Magnetic Imager (HMI, Scherrer et al. 2012) in order to explore the connection between the flare-accelerated electrons and WL formation. The authors are aware of only one statistical study which analyzed the correlation of HXR and WL emission with a comparable number of events (Matthews et al. 2003). Their main results relevant for this study are: 1) All flares above M8 class are WLFs, 2) there is no dependence of WL contrast on spectral index, and 3) there is a weak correlation between the contrast in WL and the deposition rates $> 2 \cdot 10^{28} \text{ erg}^{-1}$, although with a large scatter. For lower energies, there is no obvious trend.

Here we analyze the correlation between the HXR and WL emission in WLFs. In Section 3.2 we provide information about the instruments and data analysis steps of this study. Temporal, spatial and intensity relationships of HXR and

WL fluxes are presented in Section 3.3. Additionally, the correlation between the power deposited by nonthermal electrons and WL fluxes is analyzed. In Section 3.4, we discuss the results and their implications.

3.2 Observations

Two instruments are used for the purposes of this study: HMI and *RHESSI*.

HMI is one of the three instruments onboard the *Solar Dynamics Observatory* (*SDO*, Pesnell et al. 2012). It observes the solar disk in the Fe I absorption line at 617.3 nm with a spatial resolution of $1.0''$ (Scherrer et al. 2012). We use the standard level 1.5 continuum filtergram data, with no limb darkening correction applied and a time cadence of 45 seconds.

RHESSI is an instrument designed for hard X-ray/gamma ray imaging and spectroscopy of solar flares. The best spatial resolution obtainable is $\sim 2.3''$, and the spectral resolution is 1 – 10 keV FWHM in the operating energy range from 3 keV to 17 MeV (Lin et al. 2002). With *RHESSI*, we are able to exactly match the integration time of HMI.

Here we report joint observations of *RHESSI* and HMI of 43 WLFs spanning *GOES* classes M and X and occurring between 2011 and 2014. All flares larger than *GOES* M5 class in the *RHESSI* database are included in this study. Events below M5 class in our sample have at least one of the following properties: occurrence in 2011, which was the year we studied in most detail, occurrence near the limb, or an intense, short duration peak in HXRs (flares with this property often show WL emission). For each flare, we computed the HXR flux at 30 keV, the HXR spectral index, the limb darkening correction factor for WL emission, the WL flux, the WL relative enhancement and the deposited energy by nonthermal electrons above 50 keV. These data, together with the date, *GOES* class, position, and peak time are given in Table 3.1. Steps of our analysis are explained in the following subsections.

3.2.1 Time profiles

First, we plotted the WL lightcurve (calculated by summing the WL emission over the HXR footpoint areas) for a time span of ~ 1.5 hr around peak time, in order to see the evolution of the non-flaring Sun relative to the enhancement of WL emission during solar flares (see left panels in Figure 3.1). For making the images as shown in Figure 3.1 and calculating WL fluxes for later analysis, we subtracted a pre-flare image from the peak image. For each flare, we chose the pre-flare image as the one closest to the average value (of all frames) inside the time range of a few minutes before the flare peak time (using images far from the peak time is not applicable, as the flaring region can evolve substantially on larger time scales). Peak- and pre-flare frames are indicated in Figure 3.1 with

purple arrows. From the non-flaring temporal variation we infer a conservative (upper limit) error estimate as the maximum of this variation around peak time, and we give this value in Table 3.1. Vertical lines indicate the peak time range, for which we plot *GOES*, HXR and WL time profiles (middle panels in Figure 3.1).

We note here that the detection sensitivity for WL emission is significantly enhanced when considering time profiles summed over the flaring region (such as shown in Figure 3.1) in combination with inspecting running difference images by eye.

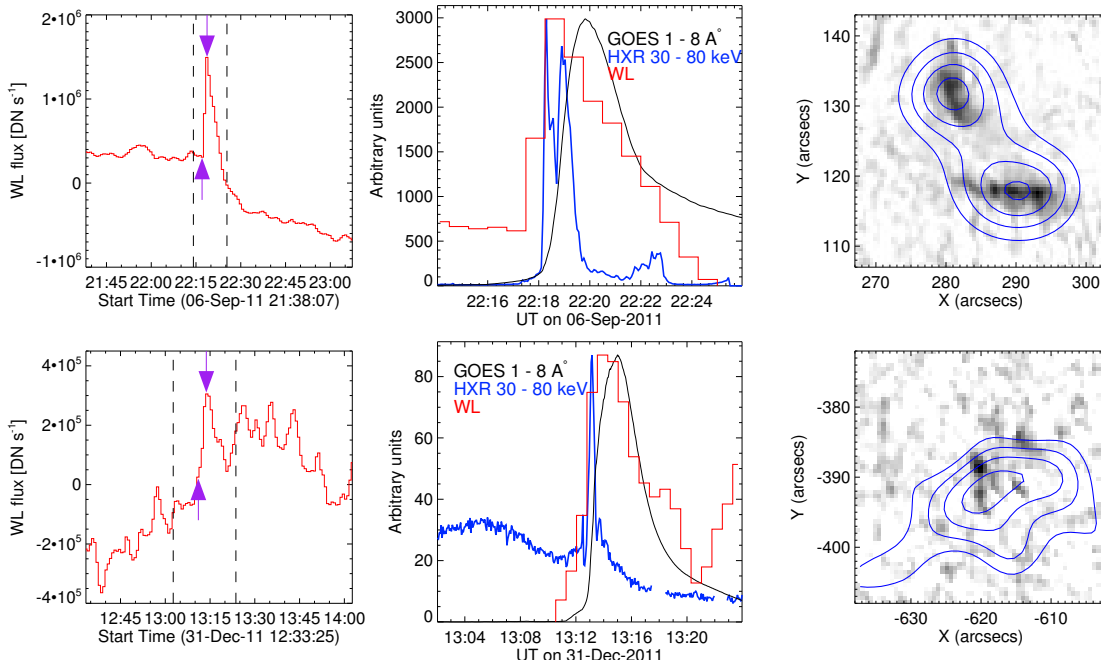


Figure 3.1: Time profiles and images of an intense (SOL2011-09-06 (X2.1)) and a weak (SOL2011-12-31 (M2.4)) event in our sample: Left panels show the WL emission (calculated inside the 30% contour of HXR emission) time profiles for a long time span around the time of peak emission to compare the increase due to the flare relative to the fluctuations of the non-flaring active region. The vertical lines indicate time ranges used in the plots in the central panels, while the purple arrows indicate peak- and pre-flare frames used for the analysis. Central plots show WL flux in red, HXR flux at 30 – 80 keV in blue and *GOES* flux at 1 – 8 Å in black. Right panels show pre-flare subtracted images of events in HMI, with *RHESSI* contours of 30%, 50%, 70% and 90% of the maximum emission in the 30 – 80 keV CLEAN image overlaid in blue.

3.2.2 HXR imaging and WL flux derivation

For each flare we made an image in the HXR range at 30 – 80 keV using detectors 3–6 and the CLEAN algorithm (Hurford et al. 2002), and overlaid it on the WL pre-flare subtracted image. Two examples are shown in the right panels of Figure 3.1. We identified a systematic offset between WL and HXR footpoints. For each flare, we computed polar angles of the maximum HXR and WL emissions, and

the difference between them. The histogram distribution of polar angle differences peaks at 0.25 ± 0.1 degrees. This difference is most noticeable at the solar limb, where it translates to a spatial separation of $\sim 4''$. We speculate that this difference comes from an error in the roll-angle calibration in one of the two instruments. For our study, we overcome this problem by calculating the WL flux inside the 30% contour of maximum HXR emission. This is a large enough area so that most WL enhancement is included, despite the offset in position, for all flares.

3.2.3 HXR spectral fitting

We used the OSPEX package for the calculation of HXR fluxes and spectral indices. We performed spectral fitting above 18 keV with the integration time of 45 seconds around the time of maximum WL emission, in order to match the integration time of HMI. We fitted a thermal + power-law model to the data. Fluxes at higher energies were extrapolated from the fluxes at 30 keV and the spectral indices using the standard formula for HXR power spectrum:

$$F(E) = F(30) \cdot (E/30)^{-\gamma}, \quad (3.1)$$

where $F(E)$ stands for photon flux at energy E , $F(30)$ is the photon flux at 30 keV, and γ is the spectral index. Because of the steepness of the HXR spectrum, there are many more photons with lower energies. The energy of 30 keV is chosen because it is the lowest energy that contains a negligible amount of thermal emission, and still contains large fluxes of nonthermal photons. As we are mainly interested in the spectral slope around 30 keV, we only fit a thermal + single power-law, without a break. If these values are used for the extrapolation to higher energies, it should be considered that hard X-ray flare spectra generally have breaks (e.g., Dulk et al. 1992), and our simplified approach could lead to the overestimation of HXR fluxes at higher energies, in particular above ~ 100 keV. Using the thick target approximation (e.g., Brown 1971), the energy deposition by nonthermal electrons can be derived from the HXR spectral parameters for a given low energy cutoff (e.g., Saint-Hilaire & Benz 2005).

3.3 Results

3.3.1 The data analysis steps for two examples

In Figure 3.1 we present lightcurves and images of two flares, an intense event in which a clear temporal and spatial correlation between WL and HXR fluxes can be seen, and one of the weakest events in our sample. The SOL2011-09-06 (X2.1) event is an example with very good HXR counting statistics and a WL source well above the pre-flare emission. The post-flare WL emission for this event does not recover to the pre-flare value, which appears to be due to the flare-related permanent change in the magnetic field. For the few events with similarly

good statistics, the observations are good enough to compare details of the flare ribbons (e.g., Krucker et al. 2011). However, such a study is not the focus of this statistical work where we try to include a large number of events. On the other hand, the SOL2011-12-31 (M2.4) event has rather poor statistics and a low contrast and the details of the source morphologies cannot be compared. Nevertheless, the WL flux integrated over the HXR source has a local maximum roughly at the expected time (the peak emission in WL for this event is ~ 45 seconds after peak time of HXR emission). Post-flare time profile of this event shows a few additional peaks. Due to its weak WL emission (an order of magnitude weaker than the WL emission of SOL2011-09-06 (X2.1)), these sub-peaks most probably represent just the usual background fluctuations of the active region rather than the subsequent peaks of WL emission due to the flare. We included this event in our sample although with a large error bar at $\sim 80\%$ of the observed value (see Table 3.1).

Figure 3.1 clearly shows that careful examination of lightcurves is essential for determining the appropriate pre-flare image and for imaging the flare-enhanced emission in WL. We also point out co-temporality between HXR and WL emission in the majority of our events, within our 45 second cadence. A higher cadence of a few seconds would be needed for a closer inspection of WL–HXR co-temporality. WL flux shows a longer decay phase for most events, which usually lasts a few minutes. Generally, the good correlation of HXR and WL time profiles, with a longer decay phase in WL, is in agreement with previous observations (e.g., Hudson et al. 1992; Xu et al. 2006; Matthews et al. 2003).

3.3.2 Relation between HXR and WL fluxes

3.3.2.1 The limb darkening correction

Depending on the height of the WL source above the photosphere, we expect to see a limb darkening effect (i.e. stronger absorption for events closer to the limb due to the enhanced column density along the line-of-sight to Earth). For a WL source originating in the photosphere, the classical limb darkening function could be a good approximation. For sources at higher altitudes, the absorption along the line of sight could be significantly less than the photospheric value. Additionally, the roughness (i.e. deviation from spherical symmetry) will further influence the overall limb darkening effect. Hence, a limb-darkening correction is at best an approximation.

In Figure 3.2 we plot the uncorrected WL/HXR flux ratios vs. the radial distance from Sun center of the WL emission. Here we assume that center-to-limb variation in HXR at 30 keV is negligible, which is in agreement with the studies of Datlowe et al. (1977) and Kašparová et al. (2007). Because we do not know if all flares have a constant WL/HXR ratio (some flares might be more efficient in producing WL emission than others), fitting a limb darkening function directly to these values is not applicable. Instead, we use the average ratio of disk flares (radial distance < 700 arcsec) as a reference for events that are not affected by

limb darkening. This value is represented by a horizontal line in the plot. The red curve is the limb darkening function taken from Pierce & Slaughter (1977) for the wavelength closest to 617.3 nm. While no firm conclusions can be made, it can be seen that all flares near the limb (radial distance > 900 arcsec) have substantially smaller WL/HXR ratios than the average. Our conclusion is that applying the limb darkening correction is better than applying no correction at all, even though it is far from perfect.

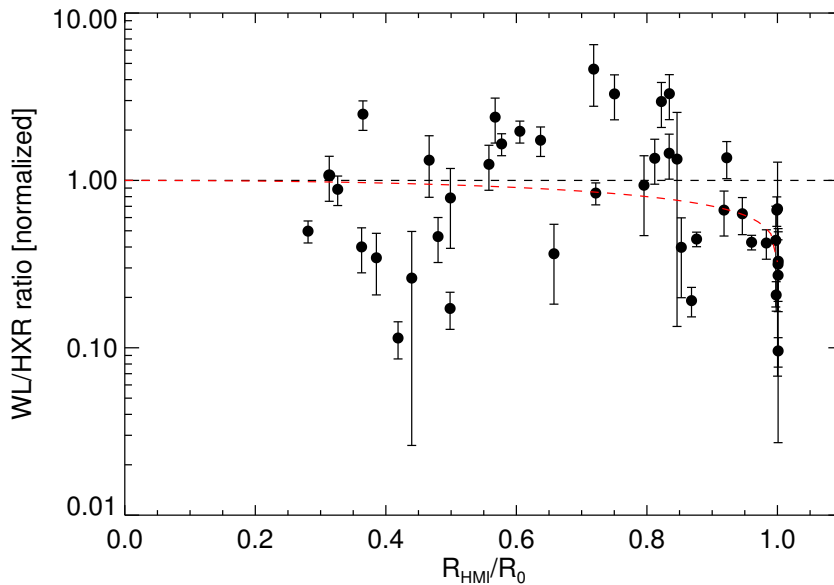


Figure 3.2: Plot of the ratio of WL to HXR fluxes vs. radial distance of WL flare from Sun center. R_{HMI} and R_0 denote the distance of the maximum WL emission from Sun center and Sun’s radius at flaring time, respectively. Ratios of WL and HXR fluxes are normalized to the average ratio for flares with radial distance < 700 arcsec. The photospheric limb darkening function is plotted in red.

3.3.2.2 Fitting of the data and the correlation coefficients

As described in Section 3.2, HXR fluxes were calculated for $E = 30$ keV via spectral fitting, while WL fluxes were calculated inside the 30% *RHESSI* contour from pre-flare subtracted images. When applying spectral fitting, we used different detectors for each flare, depending on the detector state of health that varies during the large time span of 4 years considered in this survey. The HXR flux of each flare is the average of the fluxes given by the ‘healthy’ detectors at the time of the flare. The error bar is estimated as the standard deviation of the HXR fluxes given by these detectors around the average value. Error bars in WL are given by the maximum emission of the fluctuation of the background ~ 15 minutes before a flare occurred. These are conservative (upper limit) values, especially for fainter flares. In Figure 3.3, we present the correlation between HXR and WL

fluxes for two cases: measured WL fluxes, and WL fluxes with the limb darkening correction applied. Since the calculated fluxes span two orders of magnitude, we present our results in a log–log plot.

We use a fit to both sets of values in the form $F_{\text{WL}} = A \cdot (F_{30})^b$, where F_{WL} is white light flux, F_{30} is HXR photon flux at 30 keV, A is a constant, and b is the power law index. Since we a priori do not know the mutual dependence of the WL and HXR fluxes, we use a bisector regression method (Isobe et al. 1990). For the power law index we get the values of $b = (0.77 \pm 0.10)$ and $b = (0.61 \pm 0.07)$ for the observed and limb darkening corrected values, respectively. The correlation coefficient has values of 0.62 and 0.68 at the energy of 30 keV.

Another frequently used parameter for quantifying WL emission in solar flares is the relative enhancement of the WL emission (defined as $\Delta I/I_0 = (I - I_0)/I_0$, I and I_0 being the peak- and pre-flare fluxes, respectively), as it compares the pre-flare photospheric flux to the flare enhancement. In order to study its connection to the HXR emission, we made pre-flare subtracted images and normalized them to the pre-flare images, in order to get the information on the relative enhancement of each individual pixel, for each flare. We chose the brightest pixel in the relative enhancement maps as our estimate of the relative enhancement of the WL emission. Using the average value of relative enhancements over the area of the 30% HXR contour would lead to underestimation of the relative enhancement, since this area contains many non-flaring pixels. Here we note that we only analyzed on-the-disk flares, as otherwise I_0 does not come from the underlying photosphere (these values are also not included in Table 3.1). The plot of maximum relative enhancements vs. HXR fluxes is presented in Figure 3.4. Single pixel values of $\Delta I/I_0$ span the range 0.1 – 0.6. The correlation is weaker than in the former case of absolute enhancements, with the correlation coefficient being 0.36. The correlation is only slightly improved if only the best events from our sample are chosen (red points in the figure), when the correlation coefficient reaches the value of 0.4. Our results slightly favor the absolute enhancement over the relative enhancement as the more relevant quantity for the WL formation; however, further studies must be made in order to test this claim in more detail.

We also analyzed the relation between spectral indices and WL fluxes. As can be seen in Figure 3.5, there is no correlation between the two quantities. This result suggests that the highest energy electrons play a minor role in the production of WL emission, which makes sense from an energetical point of view as the low-energy electrons carry more energy than the high-energy electrons (due to their larger numbers).

3.3.2.3 Above the limb flares

Of particular interest are the three events with emissions above the solar limb reported by Krucker et al. (2015) that are also included in the survey presented here. The HXR and WL emissions for these events occur within one degree of limb passage and the observed radial position therefore directly translates into

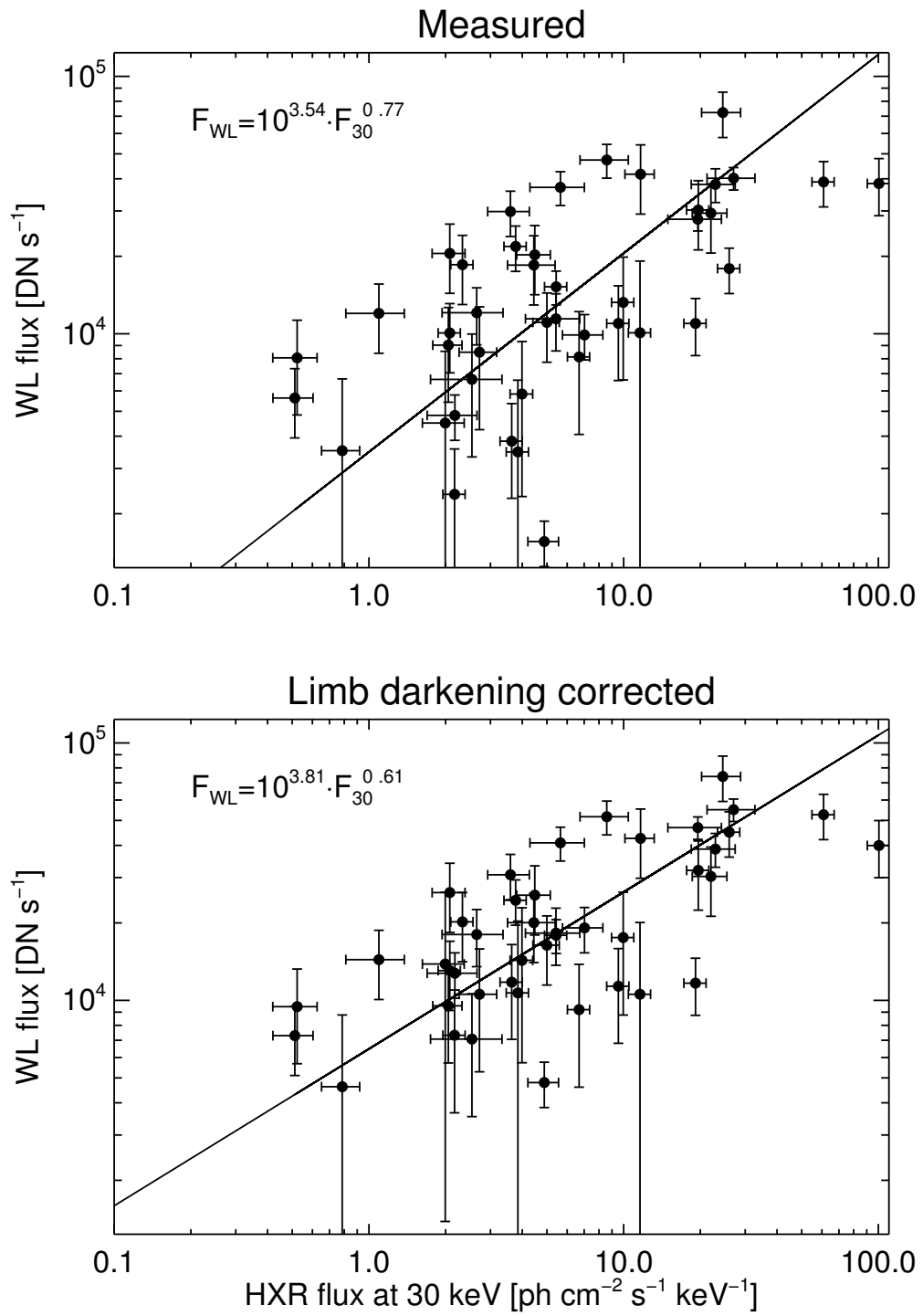


Figure 3.3: *Top:* Correlation between measured WL fluxes and HXR fluxes for 43 events analyzed in our study. *Bottom:* Same as above, but with limb darkening corrected WL fluxes.

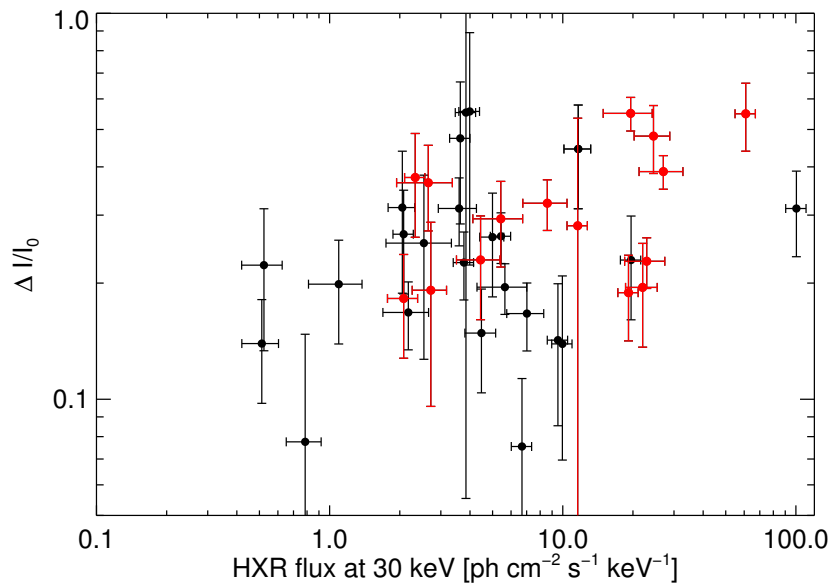


Figure 3.4: Plot of the relative enhancement of the WL emission vs. the HXR flux. The correlation is worse than for the absolute enhancement, with the correlation coefficient of 0.36. Red points denote the best events in the sample, and for this subset the correlation coefficient reaches the value of 0.4.

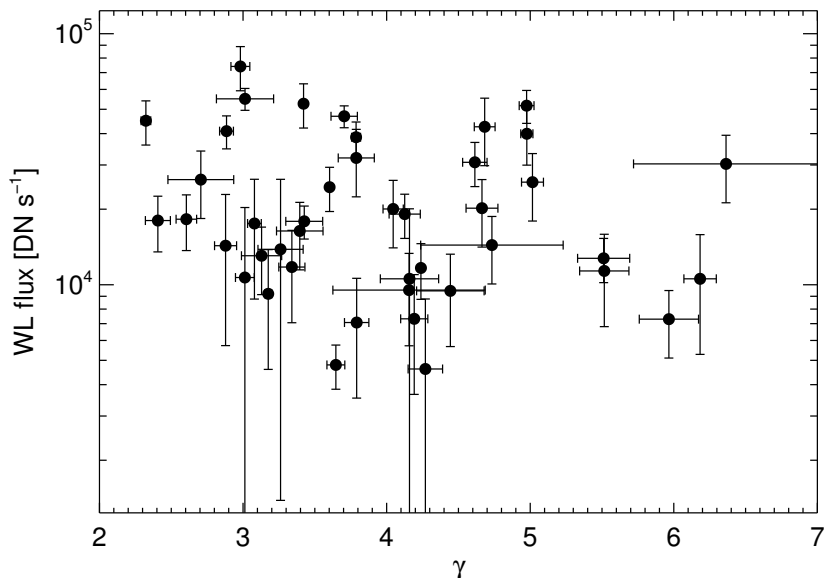


Figure 3.5: Plot of WL fluxes (limb darkening correction applied) vs. the power law indices of HXR spectra for 43 events analyzed in our study. There is no correlation between the two quantities.

actual altitude (within the measurement uncertainties). The observations show co-spatial WL and HXR source peaking at altitudes above the photosphere of around 800 km. The WL to HXR ratios for these events are between 0.095 to 0.328 if normalized to the averaged on-disk ratio. This indicates a strong limb darkening effect, but it additionally could be the case that emission from lower altitudes is completely absorbed and only the top part of the source is observed. Our statistical survey alone cannot distinguish the two explanations. To look into this issue, a detailed theoretical study of the optical depth as a function of height above the photosphere needs to be performed, but this is outside the scope of this observational work.

3.3.3 The correlation between HXR energies and WL fluxes

The correlations presented so far are all with directly observed quantities. From a physical point of view, it is desirable to directly compare the energy input (i.e., energy deposition by nonthermal electrons) vs. energy output (i.e., radiative losses in the optical range). However, such estimates rely on model assumptions. From the HXR spectra we can use the classical thick-target assumption to derive the total energy deposition of flare-accelerated electrons above a given electron energy (e.g., Brown 1971). Since we only have single-frequency WL observations, it is extremely difficult to estimate the total radiative losses in WL. For this work we are therefore limited to use the observed WL fluxes to compare with the energy deposition by nonthermal electrons. Nevertheless, this allows us to find the energy range of electrons that best correlates with the observed WL fluxes. We calculated the deposited power by electrons for cutoff energies ranging from 10 to 100 keV. In Figure 3.6 we present scatter plots for two cutoff energies, 10 and 50 keV, respectively. The best correlation is found for the deposited power by nonthermal electrons above 50 keV, while the correlation decreases rapidly if the power provided by lower energy electrons is added as well. The slopes in the scatter plots of WL flux vs. deposited power are ~ 0.6 in the 40 – 70 keV range, similar to the slopes in the fluxes scatter plots.

Figure 3.7 shows the behavior of the correlation coefficient between WL fluxes and power deposited by nonthermal electrons above different cutoff energies in one case, and between WL fluxes and HXR photon fluxes at different energies in the other case. Both show similar behavior, steep decrease for energies below 30 keV and a gradual decrease towards higher energies. This behavior can be explained within the standard thick-target model as the lowest energy electrons are stopped too high in the solar atmosphere to be responsible for WL production. The total energy carried by the highest energy electrons, on the other hand, cannot account for the overall WL emission. Obvious is also a difference in the peak energy of the two curves, which is at 30 keV for the flux–flux correlation coefficient, and at 50 keV for the power–flux correlation coefficient. This difference is a direct result of the thick-target assumption. As electrons at a given energy produce photons at all lower energies, it is expected that the correlation coefficient peaks at a higher value for the electron energy than for the photon en-

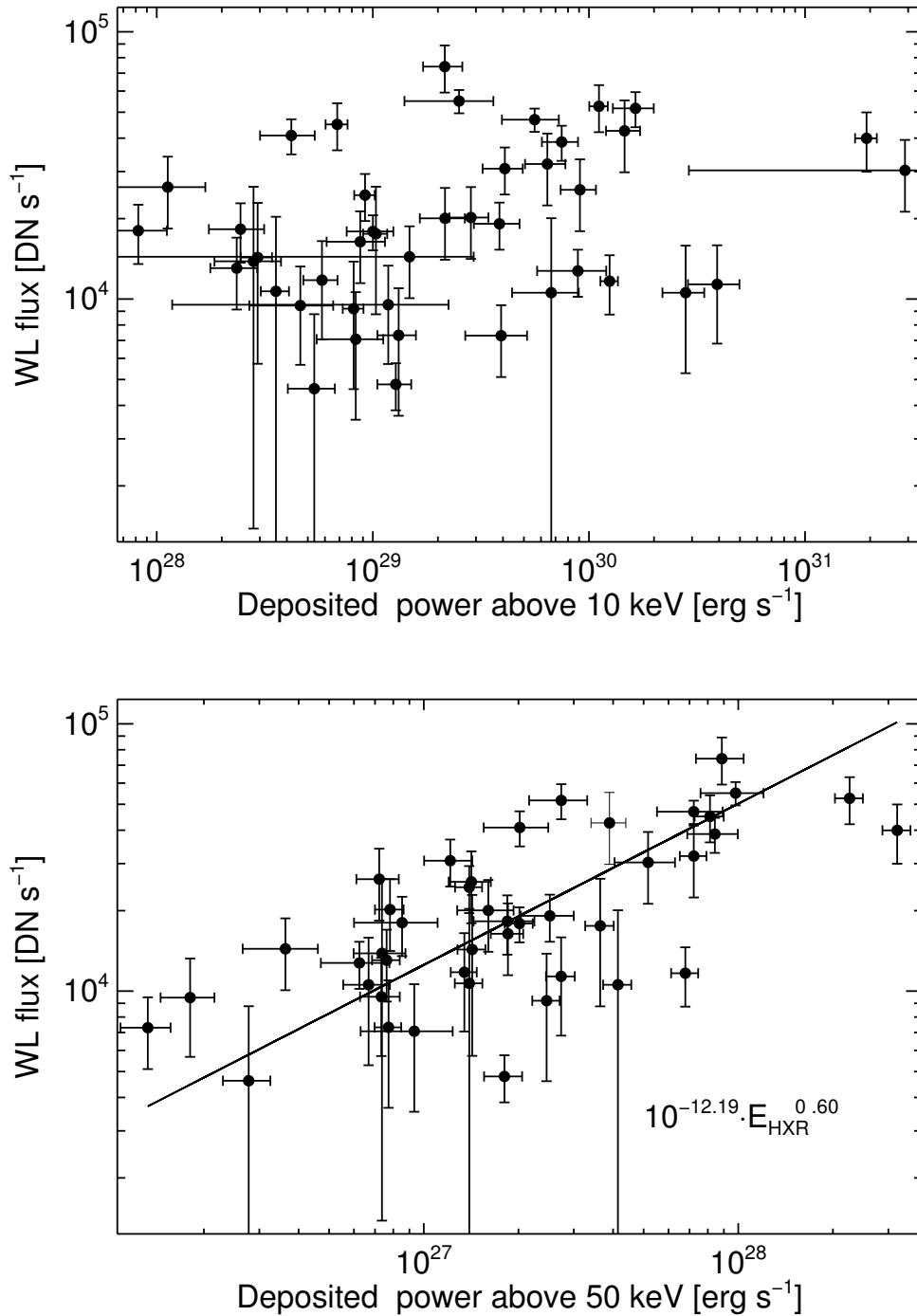


Figure 3.6: *Top:* The limb-darkening-corrected WL flux vs. the power deposited by electrons above 10 keV. Since there is no clear correlation in this case, the fit to the values is not shown. *Bottom:* Same as above, but for electrons above 50 keV.

ergy. The difference we get is in agreement with the study of Saint-Hilaire & Benz (2005), where they calculated the ratio of the turnover energy in the photon spectrum and the cutoff energy in the electron beam distribution to be ~ 0.6 . Hence, electrons with energy of 50 keV typically produce photons of 30 keV, which is in agreement with the curves shown in Figure 3.7.

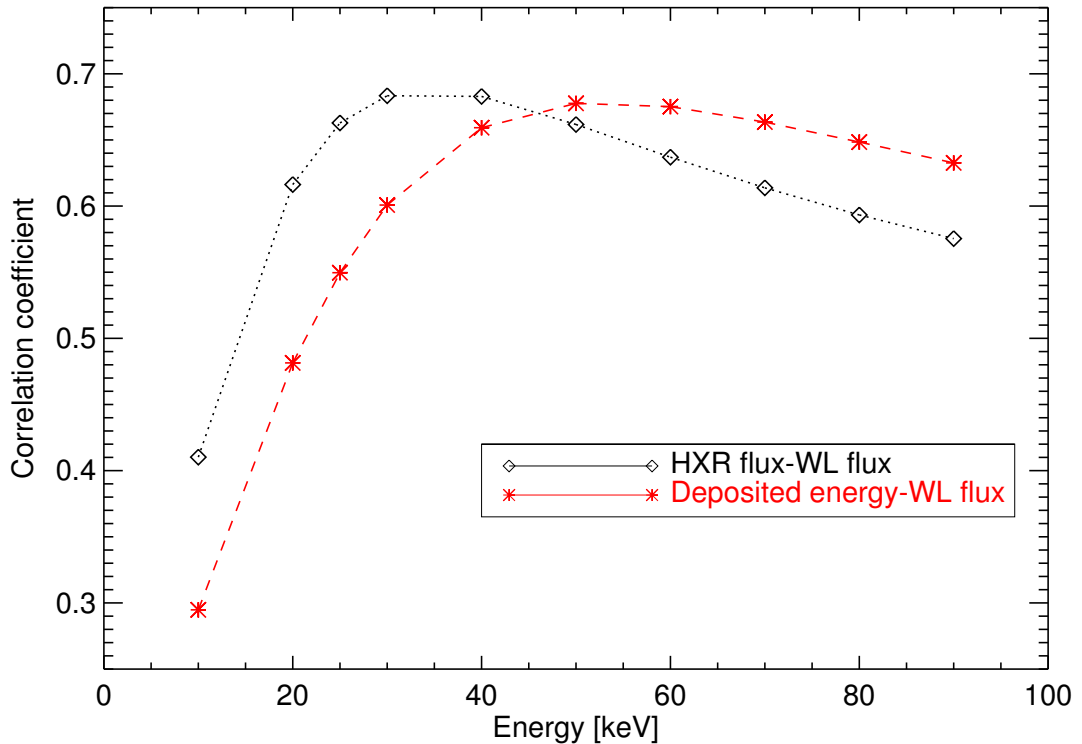


Figure 3.7: Correlation coefficient between the logarithmic values of HXR fluxes at different energies and WL fluxes (diamonds), and between the logarithmic values of the deposited energy by nonthermal HXR electrons above different threshold energies and WL fluxes (stars). The correlation coefficient decreases steeply for energies below 30 keV. It has the maximum for HXR fluxes at 30 keV, and for HXR energies for a cutoff energy around 50 keV.

3.4 Discussion and conclusions

Simultaneous observations of *RHESSI* and HMI for 43 flares spanning *GOES* classes M and X have provided valuable information about the correlations in time, space and intensity of HXR and WL fluxes in solar flares. Most of the previous observations of WL flares have focused on individual events. In this study, we present statistical results with the following conclusions.

Temporal: With the rather low cadence of HMI standard data products used in this study, the conclusions are limited. Nevertheless, the peaks of WL emission are co-temporal with HXR emission for most events, at least within the time

resolution of 45 seconds for WL emission. The WL emission has a longer decay phase, typically lasting a few minutes, as was previously reported (e.g., Hudson et al. 1992; Xu et al. 2006; Matthews et al. 2003).

Occurrence: Our statistical survey does not mandate the existence of HXR flares without WL emission. All large flares (above *GOES* class M5) show WL counterparts. The lack of WL emission in smaller flares is rather due to the difficulties in distinguishing the WL flare signal from the general time variation of the non-flaring regions at optical wavelengths than the actual absence of WL flare emission. As our study does not include microflares (i.e., *GOES* C class and smaller), we cannot state anything regarding this group of events. Nevertheless, WL emission has been reported from C-class flares (Jess et al. 2008) and there are *GOES* A- and B-class flares with relatively intense HXR emissions (order of 0.1 photon/s/cm²/keV, Ishikawa et al. (2011), Ishikawa et al. (2013)) for which WL emission could potentially be detectable.

Intensity: There is a clear correlation between WL and HXR fluxes, although with a large scatter. The correlation is not linear, but better described by a power-law with an index of (0.77 ± 0.10) and (0.61 ± 0.07) for measured and limb darkening corrected WL fluxes, respectively. The absence of a linear correlation is not surprising, as the conversion of HXR flux and WL flux at the HMI wavelength to actual energy input and output does not need to be linear. The correlation coefficient between logarithmic values of WL and HXR fluxes is 0.68 for the energy of 30 keV. The scatter of the observed and limb darkening corrected values is relatively large with extreme values being up to a factor of ~ 7.5 and ~ 2.5 different from the fitted curve for the observed and limb darkening corrected values, respectively. The WL flux correlates best with the HXR flux around 30 keV, with a decrease in the correlation coefficient for lower and higher (nonthermal) photon energies. The correlation coefficient decreases if the relative enhancements are used to describe the WL emission, and it has a value of 0.36 at the energy of 30 keV, suggesting that the pre-flare WL emission is not a key factor in the production of WL emission.

Spectral: There is no correlation between HXR spectral indices in the 30 – 100 keV range and WL fluxes. This suggests that high energy electrons play a minor role in the production of WL emission.

Energy deposition: There is a clear correlation between the deposited power by flare-accelerated electrons and WL fluxes best seen for electron energies in the range 40 – 70 keV, with a maximum correlation coefficient of 0.68 at 50 keV. The correlation coefficient decreases gradually towards higher energies, while a steep decrease is observed for lower energies. This suggests that the lowest energy electrons are not involved in the production of the WL emission. The most likely explanation for this behavior is that low energy electrons accelerated in the corona are stopped too high in the atmosphere to play a role in the WL formation.

Our results are consistent with earlier findings from a similar survey of *Yohkoh* HXR and WL data (Matthews et al. 2003). The correlation in flux, however, is a new result. The existence of a correlation does not contradict the work by

Matthews et al. 2003 and might be due to our larger sample size in combination with the enhanced sensitivity of HMI and *RHESSI* compared to *Yohkoh*. Similarly, the observed HXR spectral indices are much more accurate and the absence of a correlation is now a solid result.

In summary, we conclude that WL and HXR fluxes show a clear correspondence in space, time, and intensity. The newly found correlation between energy deposition and WL flux is a further indication that flare-accelerated electrons are the main contributor to the WL formation. The absence of detectable WL emission in weaker flares is most probably caused by the weak contrast of WL flare emission when compared to non-flaring Sun temporal variations, and it is unlikely that a second class of flares exists without WL emission, at least for larger flares. As smaller flares are expected to also have fainter WL emissions, their detection is even more difficult, making it unlikely to get conclusive observations of flares without WL counterparts.

As a possible explanation for the newly found correlation between energy deposition by >50 keV electrons and WL formation, we would like to put forward the following scenario: If HXR and WL sources are indeed co-spatial for all flares as suggested by observations of a few single events (Martínez Oliveros et al. 2012; Battaglia & Kontar 2012; Krucker et al. 2015), the accelerated electrons above 50 keV produce the WL emission by directly heating dense layers by collisions to moderate temperatures ($\sim 10^4$ K). The low-energy end of the accelerated electrons lose their energy above the WL/HXR source at lower densities producing hot plasma ($\sim 10^7$ K) in the flare ribbons that is radiating at EUV and SXR wavelengths (e.g., Hudson et al. 1994; Graham et al. 2013). Through radiative cooling, the WL source is dissipating the part of the flare energy that was carried by the high energy (> 50 keV) tail of the accelerated electrons. The energy in the low-energy electrons goes into heating of the plasma, part of which then evaporates and produces the main flare loop. An open question is the observation of rather low altitudes of the WL/HXR sources (Martínez Oliveros et al. 2012), which is challenging to explain within the standard thick-target model. In any case, our findings alone do not exclude a back-warming model where the WL source originates from deeper layers than the HXR source.

The next step in the research will be the investigation of the relation between the energy deposited by nonthermal electrons and the energy contained in WL for different threshold HXR energies. This requires coverage of the optical range by observations at several wavelengths, which are only available for a few well-observed events (e.g., Milligan et al. 2014). To test our hypothesis that the low-energy electrons produce hot plasma at higher altitudes, we are planning to analyze *SDO/AIA* data for the sample of events presented here. By applying the newly available de-saturation algorithm for AIA images (Schwartz et al. 2014), we will be able to determine EUV data points for many flares in our current statistics. This will allow us to derive the thermal energy content in the flare ribbon and compare it to the deposited energy by nonthermal electrons.

Further information about possible follow-up studies can be found in Chapter 6.

Table 3.1: List of 43 WL flares.

| Date | GOES class | Position [arcsec] | Peak time [UT] | $F_{50\text{keV}}$ [$\text{ph cm}^{-2} \text{s}^{-1} \text{keV}^{-1}$] | Limb factor | $F_{\text{WL}}(\text{corr.})$ [10^4 DN s^{-1}] | $\Delta I/I_0$ | Spectral index | Deposited power [$10^{27} \text{ erg s}^{-1}$] |
|-------------|------------|-------------------|----------------|--|-------------|--|-----------------|-----------------|--|
| 2011 Feb 15 | X2.2 | [210, -220] | 01:53:42 | 11.6 ± 1.5 | 1.02 | 4.3 ± 1.3 | 0.45 ± 0.13 | 4.68 ± 0.07 | 3.90 ± 0.51 |
| 2011 Feb 18 | M1.4 | [765, -275] | 13:01:57 | 0.51 ± 0.09 | 1.30 | 0.7 ± 0.2 | 0.14 ± 0.04 | 5.97 ± 0.21 | 0.13 ± 0.03 |
| 2011 Feb 18 | M6.6 | [755, -270] | 10:10:57 | 2.07 ± 0.31 | 1.28 | 2.6 ± 0.8 | 0.18 ± 0.05 | 2.71 ± 0.23 | 0.72 ± 0.11 |
| 2011 Feb 24 | M3.5 | [-925, 275] | 07:31:13 | 3.99 ± 0.41 | 2.45 | 1.4 ± 0.9 | 0.11 ± 0.07 | 2.88 ± 0.08 | 1.43 ± 0.15 |
| 2011 Mar 07 | M3.7 | [615, 560] | 20:01:14 | 9.96 ± 0.35 | 1.33 | 1.8 ± 0.9 | 0.14 ± 0.07 | 3.08 ± 0.05 | 3.64 ± 0.39 |
| 2011 Mar 09 | X1.5 | [190, 275] | 23:20:44 | 22.0 ± 3.4 | 1.03 | 3.0 ± 0.9 | 0.19 ± 0.06 | 6.36 ± 0.64 | 5.17 ± 1.18 |
| 2011 Mar 14 | M4.2 | [705, 340] | 19:51:30 | 4.48 ± 0.68 | 1.27 | 2.6 ± 0.8 | 0.15 ± 0.04 | 5.02 ± 0.08 | 1.42 ± 0.20 |
| 2011 Mar 15 | M1.0 | [750, 325] | 00:21:30 | 0.79 ± 0.13 | 1.31 | 0.46 ± 0.42 | 0.08 ± 0.07 | 4.27 ± 0.12 | 0.28 ± 0.05 |
| 2011 Jul 30 | M9.3 | [-525, 170] | 02:08:11 | 8.59 ± 1.84 | 1.09 | 5.2 ± 0.8 | 0.32 ± 0.05 | 4.97 ± 0.05 | 2.74 ± 0.56 |
| 2011 Sep 06 | X2.1 | [280, 130] | 21:18:37 | 24.5 ± 4.3 | 1.02 | 7.4 ± 1.5 | 0.48 ± 0.10 | 2.98 ± 0.07 | 8.87 ± 1.47 |
| 2011 Sep 24 | M5.8 | [-740, 155] | 20:34:20 | 2.72 ± 0.46 | 1.25 | 1.1 ± 0.5 | 0.19 ± 0.10 | 6.18 ± 0.11 | 0.67 ± 0.12 |
| 2011 Sep 24 | X1.9 | [-815, 165] | 09:36:35 | 27.0 ± 5.8 | 1.37 | 5.5 ± 0.6 | 0.39 ± 0.04 | 3.01 ± 0.20 | 9.81 ± 2.17 |
| 2011 Sep 26 | M4.0 | [-520, 120] | 05:06:35 | 4.44 ± 0.94 | 1.08 | 2.0 ± 0.6 | 0.23 ± 0.07 | 4.05 ± 0.07 | 1.60 ± 0.33 |
| 2011 Dec 26 | M2.3 | [635, 325] | 20:16:55 | 0.52 ± 0.10 | 1.17 | 0.95 ± 0.38 | 0.22 ± 0.09 | 4.44 ± 0.23 | 0.18 ± 0.04 |
| 2011 Dec 31 | M2.4 | [-620, -395] | 13:13:10 | 1.09 ± 0.28 | 1.20 | 1.4 ± 0.4 | 0.20 ± 0.06 | 4.73 ± 0.50 | 0.36 ± 0.10 |
| 2012 Mar 09 | M6.3 | [50, 380] | 03:40:15 | 9.53 ± 0.95 | 1.03 | 1.1 ± 0.5 | 0.14 ± 0.06 | 5.52 ± 0.17 | 2.73 ± 0.30 |
| 2012 May 10 | M5.7 | [-385, 255] | 04:16:23 | 19.63 ± 0.86 | 1.06 | 3.2 ± 1.0 | 0.23 ± 0.07 | 3.78 ± 0.13 | 7.22 ± 0.76 |
| 2012 Jun 03 | M3.3 | [-565, 275] | 17:53:10 | 6.68 ± 0.67 | 1.13 | 0.92 ± 0.46 | 0.8 ± 0.4 | 3.18 ± 0.02 | 2.46 ± 0.25 |
| 2012 Jul 04 | M5.3 | [290, -340] | 09:54:40 | 2.05 ± 0.27 | 1.05 | 0.95 ± 0.38 | 0.31 ± 0.13 | 4.16 ± 0.53 | 0.73 ± 0.10 |
| 2012 Jul 05 | M4.7 | [415, -335] | 03:35:10 | 2.33 ± 0.23 | 1.09 | 2.0 ± 0.6 | 0.38 ± 0.11 | 4.66 ± 0.11 | 0.78 ± 0.08 |
| 2012 Jul 05 | M6.1 | [500, -340] | 11:44:10 | 3.77 ± 0.38 | 1.12 | 2.4 ± 0.5 | 0.23 ± 0.05 | 3.60 ± 0.02 | 1.40 ± 0.15 |
| 2012 Jul 06 | M2.9 | [590, -330] | 01:38:55 | 5.43 ± 0.54 | 1.18 | 1.8 ± 0.3 | 0.26 ± 0.04 | 3.43 ± 0.13 | 2.01 ± 0.20 |
| 2012 Jul 19 | M7.7 | [925, -200] | 05:21:40 | 2.17 ± 0.22 | 3.08 | 0.73 ± 0.37 | — | 4.19 ± 0.09 | 0.77 ± 0.07 |
| 2012 Aug 06 | M1.6 | [-915, -230] | 04:35:54 | 1.99 ± 0.37 | 3.08 | 1.4 ± 1.2 | 0.42 ± 0.38 | 3.26 ± 0.16 | 0.74 ± 0.14 |
| 2012 Oct 23 | X1.8 | [-800, -260] | 03:15:30 | 60.9 ± 6.1 | 1.35 | 5.3 ± 1.1 | 0.55 ± 0.11 | 3.42 ± 0.01 | 22.59 ± 2.38 |
| 2012 Nov 20 | M1.7 | [950, 200] | 12:39:26 | 3.84 ± 0.38 | 3.08 | 1.1 ± 1.0 | — | 3.01 ± 0.07 | 1.40 ± 0.15 |

| Date | GOES class | Position [arcsec] | Peak time [UT] | $F_{30\text{keV}}$ [$\text{ph cm}^{-2} \text{s}^{-1} \text{keV}^{-1}$] | Limb factor | $F_{\text{WL}}(\text{corr.})$ [10^4 DN s^{-1}] | $\Delta I/I_0$ | Spectral index | Deposited power [$10^{27} \text{ erg s}^{-1}$] |
|-------------|------------|-------------------|----------------|--|-------------|--|-----------------|-----------------|--|
| 2013 May 13 | X1.7 | [-930, 200] | 02:09:37 | 4.88 ± 0.67 | 3.08 | 0.48 ± 0.10 | — | 3.65 ± 0.06 | 1.80 ± 0.25 |
| 2013 May 13 | X2.8 | [-925, 180] | 16:03:37 | 26.0 ± 2.6 | 2.51 | 4.5 ± 0.9 | 0.55 ± 0.11 | 2.32 ± 0.03 | 8.13 ± 0.81 |
| 2013 May 15 | X1.2 | [-850, 200] | 01:41:53 | 5.00 ± 0.59 | 1.48 | 1.6 ± 0.5 | 0.26 ± 0.08 | 3.39 ± 0.16 | 1.85 ± 0.23 |
| 2013 Oct 25 | X1.7 | [-910, -160] | 07:58:14 | 19.6 ± 4.6 | 1.68 | 4.7 ± 0.5 | 0.55 ± 0.06 | 3.70 ± 0.09 | 7.22 ± 1.59 |
| 2013 Oct 28 | M5.1 | [-440, -195] | 15:10:59 | 2.54 ± 0.79 | 1.06 | 0.71 ± 0.35 | 0.25 ± 0.13 | 3.79 ± 0.08 | 0.93 ± 0.30 |
| 2013 Oct 28 | X1.0 | [910, 40] | 01:59:44 | 5.42 ± 1.31 | 1.60 | 1.8 ± 0.5 | 0.29 ± 0.07 | 2.61 ± 0.07 | 1.84 ± 0.42 |
| 2013 Nov 10 | X1.1 | [230, -285] | 05:13:12 | 3.59 ± 0.67 | 1.03 | 3.1 ± 0.6 | 0.31 ± 0.06 | 4.61 ± 0.09 | 1.21 ± 0.22 |
| 2014 Jan 07 | X1.2 | [-220, -170] | 10:11:39 | 22.9 ± 4.5 | 1.02 | 3.9 ± 0.6 | 0.23 ± 0.03 | 3.79 ± 0.03 | 8.43 ± 1.76 |
| 2014 Jan 27 | M4.9 | [-940, -260] | 22:09:24 | 2.17 ± 0.48 | 2.64 | 1.3 ± 0.3 | 0.17 ± 0.03 | 5.51 ± 0.18 | 0.62 ± 0.13 |
| 2014 Feb 07 | M1.9 | [765, 265] | 10:28:10 | 2.08 ± 0.09 | 1.30 | 1.3 ± 0.4 | 0.27 ± 0.08 | 3.13 ± 0.14 | 0.76 ± 0.08 |
| 2014 Mar 12 | M9.3 | [910, 270] | 22:31:59 | 7.02 ± 1.27 | 1.93 | 1.9 ± 0.4 | 0.17 ± 0.03 | 4.13 ± 0.11 | 2.52 ± 0.44 |
| 2014 Mar 29 | X1.0 | [515, 265] | 17:46:16 | 5.65 ± 1.36 | 1.10 | 4.1 ± 0.6 | 0.20 ± 0.03 | 2.88 ± 0.05 | 2.02 ± 0.44 |
| 2014 Jun 11 | X2.2 | [-820, -305] | 09:05:10 | 2.65 ± 0.71 | 1.49 | 1.8 ± 0.5 | 0.36 ± 0.09 | 2.41 ± 0.09 | 0.85 ± 0.24 |
| 2014 Oct 16 | M4.3 | [-935, -225] | 13:02:00 | 3.63 ± 0.36 | 3.08 | 1.2 ± 0.5 | 0.47 ± 0.19 | 3.34 ± 0.09 | 1.35 ± 0.13 |
| 2014 Oct 22 | M8.7 | [-390, -295] | 01:38:45 | 19.1 ± 1.9 | 1.06 | 1.2 ± 0.3 | 0.19 ± 0.05 | 4.24 ± 0.01 | 6.79 ± 0.65 |
| 2014 Oct 22 | X1.1 | [-170, -320] | 14:06:30 | 100.5 ± 4.4 | 1.04 | 4.0 ± 1.0 | 0.31 ± 0.08 | 4.98 ± 0.04 | 32.01 ± 3.23 |
| 2014 Oct 24 | M4.0 | [80, -410] | 07:40:59 | 11.6 ± 1.2 | 1.05 | 1.1 ± 1.0 | 0.28 ± 0.25 | 4.16 ± 0.20 | 4.14 ± 0.42 |

Bibliography

- Aboudarham, J. & Henoux, J. C. 1986, *A&A*, **156**, 73
- Battaglia, M. & Kontar, E. P. 2012, *ApJ*, **760**, 142
- Benz, A. O. 2008, *Living Reviews in Solar Physics*, **5**, 1
- Brown, J. C. 1971, *Sol. Phys.*, **18**, 489
- Chen, Q. R. & Ding, M. D. 2005, *ApJ*, **618**, 537
- Chen, Q. R. & Ding, M. D. 2006, *ApJ*, **641**, 1217
- Datlowe, D. W., O'Dell, S. L., Peterson, L. E., & Elcan, M. J. 1977, *ApJ*, **212**, 561
- Dulk, G. A., Kiplinger, A. L., & Winglee, R. M. 1992, *ApJ*, **389**, 756
- Fletcher, L., Dennis, B. R., Hudson, H. S., et al. 2011, *Space Sci. Rev.*, **159**, 19
- Graham, D. R., Hannah, I. G., Fletcher, L., & Milligan, R. O. 2013, *ApJ*, **767**, 83
- Hudson, H. S. 1972, *Sol. Phys.*, **24**, 414
- Hudson, H. S., Acton, L. W., Hirayama, T., & Uchida, Y. 1992, *PASJ*, **44**, L77
- Hudson, H. S., Strong, K. T., Dennis, B. R., et al. 1994, *ApJL*, **422**, L25
- Hudson, H. S., Wolfson, C. J., & Metcalf, T. R. 2006, *Sol. Phys.*, **234**, 79
- Hurford, G. J., Schmahl, E. J., Schwartz, R. A., et al. 2002, *Sol. Phys.*, **210**, 61
- Ishikawa, S., Krucker, S., Ohno, M., et al. 2011, *AGU Fall Meeting Abstracts*, , SH41A1908
- Ishikawa, S.-n., Krucker, S., Ohno, M., & Lin, R. P. 2013, *ApJ*, **765**, 143
- Isobe, T., Feigelson, E. D., Akritas, M. G., & Babu, G. J. 1990, *ApJ*, **364**, 104
- Jess, D. B., Mathioudakis, M., Crockett, P. J., & Keenan, F. P. 2008, *ApJL*, **688**, L119
- Kašparová, J., Kontar, E. P., & Brown, J. C. 2007, *A&A*, **466**, 705
- Krucker, S., Hudson, H. S., Jeffrey, N. L. S., et al. 2011, *ApJ*, **739**, 96
- Krucker, S., Saint-Hilaire, P., Hudson, H. S., et al. 2015, *ApJ*, **802**, 19
- Lin, R. P., Dennis, B. R., Hurford, G. J., et al. 2002, *Sol. Phys.*, **210**, 3
- Machado, M. E., Emslie, A. G., & Avrett, E. H. 1989, *Sol. Phys.*, **124**, 303
- Martínez Oliveros, J.-C., Hudson, H. S., Hurford, G. J., et al. 2012, *ApJL*, **753**, L26
- Matthews, S. A., van Driel-Gesztelyi, L., Hudson, H. S., & Nitta, N. V. 2003, *A&A*, **409**, 1107
- Metcalf, T. R., Canfield, R. C., & Saba, J. L. R. 1990, *ApJ*, **365**, 391
- Milligan, R. O., Kerr, G. S., Dennis, B. R., et al. 2014, *ApJ*, **793**, 70
- Pesnell, W. D., Thompson, B. J., & Chamberlin, P. C. 2012, *Sol. Phys.*, **275**, 3
- Pierce, A. K. & Slaughter, C. D. 1977, *Sol. Phys.*, **51**, 25
- Rust, D. M. & Hegwer, F. 1975, *Sol. Phys.*, **40**, 141
- Saint-Hilaire, P. & Benz, A. O. 2005, *A&A*, **435**, 743
- Scherrer, P. H., Schou, J., Bush, R. I., et al. 2012, *Sol. Phys.*, **275**, 207
- Schwartz, R. A., Torre, G., & Piana, M. 2014, *ApJL*, **793**, L23

BIBLIOGRAPHY

Xu, Y., Cao, W., Liu, C., et al. 2006, *ApJ*, **641**, 1210

Xu, Y., Jing, J., Wang, S., & Wang, H. 2014, *ApJ*, **787**, 7

BIBLIOGRAPHY

Chapter 4

Evidence of significant energy input in the late phase of a solar flare from *NuSTAR* X-ray observations*

Matej Kuhar^{1,2}, Säm Krucker^{1,3}, Iain G. Hannah⁴, Lindsay Glesener⁵, Pascal Saint-Hilaire³, Brian W. Grefenstette⁶, Hugh S. Hudson^{3,4}, Stephen M. White⁷, David M. Smith⁸, Andrew J. Marsh⁸, Paul J. Wright⁴, Steven E. Boggs³, Finn E. Christensen⁹, William W. Craig^{3,10}, Charles J. Hailey¹¹, Fiona A. Harrison⁶, Daniel Stern¹², William W. Zhang¹³

Abstract

We present observations of the occulted active region AR 12222 during the third *Nuclear Spectroscopic Telescope ARray* (*NuSTAR*) solar campaign on 2014 December 11, with concurrent *Solar Dynamics Observatory/Atmospheric Imaging Assembly* (*SDO/AIA*) and the *Focusing Optics X-ray Solar Imager* (*FOXSI-2*) sounding rocket observations. The active region produced a medium size solar flare one

* This chapter has been published in *The Astrophysical Journal*, **835**, 6 (2017)

¹ University of Applied Sciences and Arts Northwestern Switzerland, Bahnhofstrasse 6, 5210 Windisch, Switzerland

² Institute for Particle Physics and Astrophysics, ETH Zürich, 8093 Zürich, Switzerland

³ Space Sciences Laboratory, University of California, Berkeley, CA 94720-7450, USA

⁴ SUPA School of Physics & Astronomy, University of Glasgow, Glasgow G12 8QQ, UK

⁵ School of Physics and Astronomy, University of Minnesota - Twin Cities, Minneapolis, MN 55455, USA

⁶ Cahill Center for Astrophysics, 1216 E. California Blvd, California Institute of Technology, Pasadena, CA 91125, USA

⁷ Air Force Research Laboratory, Albuquerque, NM, USA

⁸ Physics Department and Santa Cruz Institute for Particle Physics, University of California, Santa Cruz, 1156 High Street, Santa Cruz, CA 95064, USA

⁹ DTU Space, National Space Institute, Technical University of Denmark, Elektrovej 327, DK-2800 Lyngby, Denmark

¹⁰ Lawrence Livermore National Laboratory, Livermore, CA 94550, USA

¹¹ Columbia Astrophysics Laboratory, Columbia University, New York, NY 10027, USA

¹² Jet Propulsion Laboratory, California Institute of Technology, 4800 Oak Grove Drive, Pasadena, CA 91109, USA

¹³ NASA Goddard Space Flight Center, Greenbelt, MD 20771, USA

day before the observations, at ~ 18 UT on 2014 December 10, with the flare loops still visible at the time of *NuSTAR* observations. The time evolution of the source emission in the *SDO/AIA* 335Å channel reveals the characteristics of an extreme-ultraviolet late phase event, caused by the continuous formation of new flare loops that arch higher and higher in the solar corona. The spectral fitting of *NuSTAR* observations yields an isothermal source, with temperature 3.8 – 4.6 MK, emission measure $0.3 - 1.8 \times 10^{46} \text{ cm}^{-3}$, and density estimated at $2.5 - 6.0 \times 10^8 \text{ cm}^{-3}$. The observed *AIA* fluxes are consistent with the derived *NuSTAR* temperature range, favoring temperature values in the range 4.0 – 4.3 MK. By examining the flare loops' cooling times and energy content, we estimate that at least 12 sets of flare loops were formed and subsequently cooled between the onset of the flare and *NuSTAR* observations, with their total thermal energy content an order of magnitude larger than the energy content at flare peak time. This indicates that the standard approach of using only the flare peak time to derive the total thermal energy content of a flare can lead to a large underestimation of its value.

4.1 Introduction

The *Nuclear Spectroscopic Telescope ARray* (*NuSTAR*) is a focusing hard-X ray (HXR) telescope operating in the energy range from 3 to 79 keV (Harrison et al. 2013). While primarily designed to observe far, faint astrophysical sources such as active galactic nuclei (AGN), black holes and supernova remnants, it is also capable of observing the Sun. With its focusing optics system, it can directly observe HXRs from previously undetected sources on the Sun due to its ten-times higher effective area and orders of magnitude reduced background when compared to state-of-the-art solar HXR instruments such as the *Reuven Ramaty High Energy Solar Spectroscopic Imager* (*RHESSI*, Lin et al. 2002). However, because it is optimized for observations of astrophysical objects, *NuSTAR* experiences some technical challenges when observing the Sun; these include *ghost-rays* and low throughput of its electronics. Ghost-rays are unfocused, single-bounced photons (in contrast to properly focused photons which reflect twice off the Wolter-I mirrors) coming from sources outside the field-of-view (Madsen et al. 2015). The throughput of *NuSTAR*'s focal plane detector electronics, with a maximum of 400 counts per second per telescope, can effectively diminish the hard X-ray sensitivity in the presence of extremely bright sources (Grefenstette et al. 2016), making detections of fainter spectral components (such as a nonthermal component) difficult.

Despite these challenges, *NuSTAR* has begun to provide critical new observations of faint X-ray sources on the Sun (Hannah et al. 2016), giving us new insights into the coronal heating problem and particle energization in solar flares. In that respect, occulted active regions are priority targets in the planning of *NuSTAR* observations. With the brightest emission from the footpoints and low corona hidden, *NuSTAR* can search for faint coronal signature of heated material and parti-

cle acceleration. In order to maximize *NuSTAR* livetime and minimize ghost-rays during these observations, they should be carried out during low-activity periods (preferably with no other active sources on disk).

In this chapter, we analyze the occulted active region AR 12222, which produced a C5.9 *Geostationary Operational Environmental Satellite (GOES)* class flare ~ 24 hr before *NuSTAR* observations. AR 12222 was observed in the third *NuSTAR* solar campaign on 2014 December 11. The active region was also observed by the *Solar TERrestrial RELations Observatory (STEREO)*, the Atmospheric Imaging Assembly on the *Solar Dynamics Observatory (SDO/AIA)* and the second launch of the *Focusing Optics X-ray Solar Imager (FOXSI-2)* sounding rocket. The goal of this chapter is to analyze the time evolution of the X-ray and extreme-ultraviolet (EUV) emission of the observed source above the solar limb in the context of the flare evolution scenario proposed by Woods et al. (2011) and Woods (2014). In these papers, the authors argue that flares may have four distinct phases in their evolution: (1) impulsive phase (best seen in HXRs), (2) gradual phase seen in SXR/EUV from the flare loops, (3) coronal dimming, best seen in the 171 Å line and (4) an EUV-late phase, best seen as a second peak in the 335 Å line few (up to 6) hours after the flare onset. The explanation of the EUV late-phase emission lies in the formation of subsequent flare loops, overlying the original flare loops, which result from the reconnection of magnetic fields higher than those that reconnected during the flare’s impulsive phase. Similar observations of “giant post-flare loops” and “giant arches” can be found in MacCombie & Rust (1979), Švestka et al. (1982), Švestka (1984), Švestka et al. (1995), Fárník et al. (1996), Parenti et al. (2010) and West & Seaton (2015), among others; a theoretical model of the subsequent magnetic reconnections (and its successful description of the flare SOL1973-07-29T13) is given in Kopp & Poletto (1984). More recently, Liu et al. (2013) proposed that the subsequent loop system(s) is produced by magnetic reconnection of the overlying active region’s magnetic field lines and the loop arcade produced by the flare, adding more complexity to the theoretical description of these events.

This chapter is structured as follows. In Section 4.2 we give an overview of *NuSTAR*, *SDO/AIA*, *STEREO* and *FOXSI-2* observations of AR 12222. We present the results of *NuSTAR* spectroscopy in Section 4.3, together with the comparison of *NuSTAR* derived parameters with observations in other wavelengths. The discussion of the results, as well as possible future studies, is presented in Section 4.4.

4.2 Observations

The data presented in this chapter come from the third set of solar observations with *NuSTAR*, which were carried out on 2014 December 11. The observations consisted of observations of the north pole region (quiet Sun observations) and the solar limb (from 18:39:00 to 19:04:00 UT) that are discussed here.

The target for the limb pointing and of this study is the active region AR 12222,

located ~ 35 degrees behind the south-west solar limb at the time of the *NuSTAR* observations. AR 12222 produced a *GOES* C5.9 flare one day before the *NuSTAR* observations, at 18 UT on 2014 December 10. Figure 4.1 presents the time evolution of the *GOES* flux, the 7 *SDO/AIA* EUV channels and the AIA-derived Fe XVI and Fe XVIII fluxes from flare onset until more than a day later. The *NuSTAR* observing period is indicated with vertical dashed lines. Smaller spikes in the *GOES* curve between the flare and *NuSTAR* observations represent various fainter flares coming from other active regions (AR 12233, AR 12230, AR 12235) on the solar disk. Due to the high occultation, the estimate of the *GOES* class as given above of the flare SOL2014-12-10T18 is a severe lower limit of the actual *GOES* class. The *STEREO* satellites can generally be used to give a prediction of the actual *GOES* class as they view the Sun from a different angle (Nitta et al. 2013). Even though *STEREO A* was at the right location at an angle of $\sim 175^\circ$ with respect to the Earth, it was not observing during the main and gradual phases of the flare; therefore, we cannot give an accurate *GOES* class estimate for this flare.

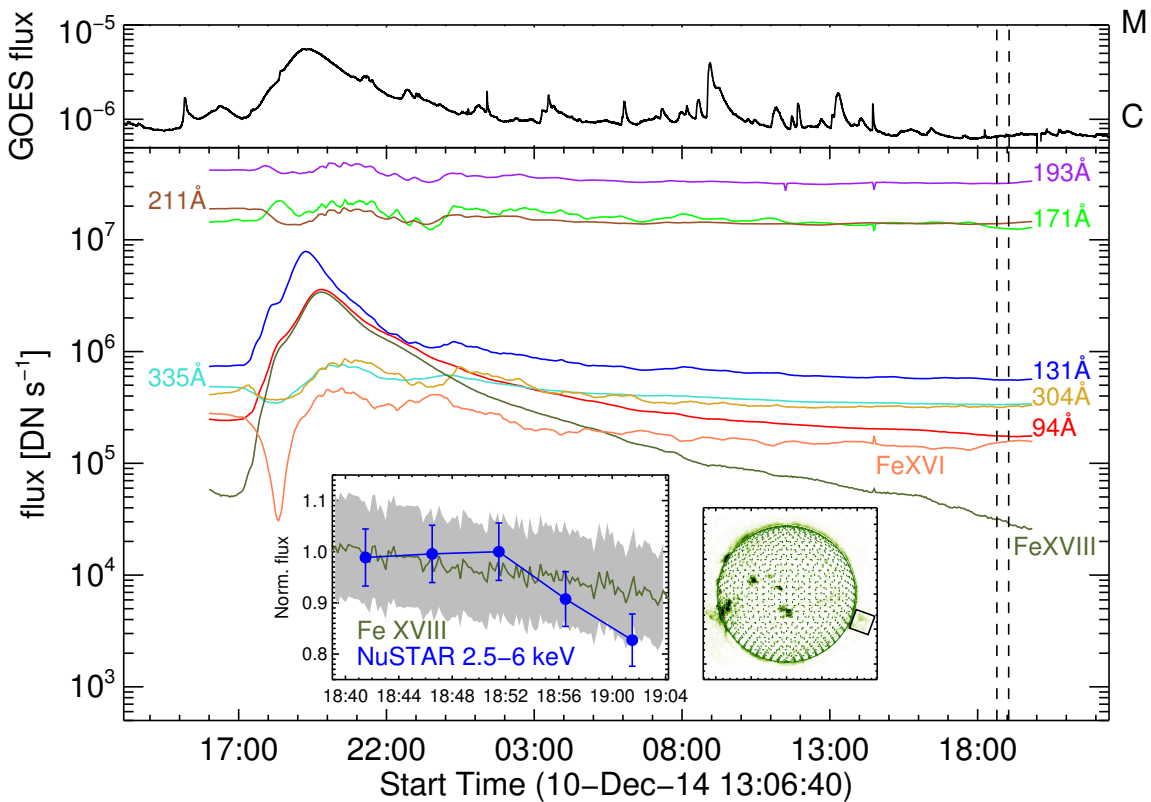


Figure 4.1: Time profiles of *GOES*, 7 EUV channels of *SDO/AIA*, Fe XVI, Fe XVIII and *NuSTAR* FPMB fluxes from the flaring area above the west limb as marked by the black box in the Fe XVIII map in the inset. Vertical dashed lines represent the time range of *NuSTAR* observations of the occulted active region AR 12222. The inner plot shows the normalized Fe XVIII (olive line) and *NuSTAR* fluxes (blue dots) during the observations. The grey shaded area represents an assumed uncertainty of 10% in the Fe XVIII flux.

The time evolution of fluxes in different AIA channels reveals two main char-

acteristics of an EUV late-phase event, as described in Woods et al. (2011) and Woods (2014): a second (in this case weaker) peak in the 335 Å line a few hours after the flare, and coronal dimming in the 171 Å line with the local minimum ~ 5 hr after the flare. As previously noted (e.g., Stewart et al. 1974; Rust & Hildner 1976; Hudson et al. 1998; Zarro et al. 1999; Howard & Harrison 2004; McIntosh et al. 2007), there is a strong correlation between coronal dimming and coronal mass ejection (CME) events; indeed, a strong CME with the velocity of $\sim 1000 \text{ km s}^{-1}$ was associated with this nominally C-class flare².

The olive curve in Figure 4.1 presents the time evolution of the Fe XVIII line flux. An estimate of the emission in the Fe XVIII line can be constructed from the 94 Å line, by subtracting the lower temperature responses from the 171 Å, 193 Å and/or 211 Å channels (see Del Zanna 2013; Reale et al. 2011; Testa & Reale 2012; Warren et al. 2012). In obtaining the Fe XVIII flux, we followed the approach of Del Zanna (2013), using the formula

$$F(\text{Fe XVIII}) \approx F(94\text{\AA}) - F(211\text{\AA})/120 - F(171\text{\AA})/450, \quad (4.1)$$

where $F(\text{Fe XVIII})$ is the Fe XVIII flux, $F(94 \text{ \AA})$, $F(211 \text{ \AA})$ and $F(171 \text{ \AA})$ are the fluxes in the 94 Å, 211 Å and 171 Å channels, respectively. The Fe XVIII line has a strong response in the temperature range from ~ 3 to ~ 10 MK, with the peak around 6.5 MK. The Fe XVIII time evolution shows a strong peak due to the flare, with a long decay phase lasting past the *NuSTAR* observations.

Similar to the Fe XVIII line, a lower-temperature Fe XVI line can be constructed from the 335 Å and 171 Å lines (Del Zanna 2013):

$$F(\text{Fe XVI}) \approx F(335\text{\AA}) - F(171\text{\AA})/70. \quad (4.2)$$

Similar to Fe XVIII, the above formula is just an approximation of the Fe XVI flux. The Fe XVI line has a temperature response of similar shape to the Fe XVIII line, with its peak at a lower temperature of ~ 2.5 MK. The time evolution of the Fe XVI flux is also shown in Figure 4.1. It is characterized by a strong dip followed by the initial rise, soon after which a decrease is observed, due to the fact that the flare becomes weaker. After ~ 8 UT on 2014 December 11, the time evolution of Fe XVI flux is determined by fore- and background emission along the line-of-sight, making the post-flare loops no longer observable in this line.

The evolution of 5-minute integrated *NuSTAR* fluxes (blue dots) and Fe XVIII fluxes (olive line) is given in the inset of Figure 4.1. The *NuSTAR* and Fe XVIII time evolutions show similar behaviour, with the (slow) decay rate of the two agreeing within the error bars and the only difference being the steeper decay of *NuSTAR* flux towards the end of the observation, which is likely due to the presence of the chip gap. The *NuSTAR* focal plane consists of a 2×2 array of CdZnTe detectors, which are divided into quadrants by a chip gap (Harrison et al. 2013). As the telescope pointing drifted slowly during the observations, the gap covered part of the area used for calculating the flux. Therefore, it is probable that the steeper

² Data taken from the LASCO CME Catalog: http://cdaw.gsfc.nasa.gov/CME_list/.

decay of the *NuSTAR* emission towards the end of the observation is not due to solar variability, but rather a consequence of the telescope drift. This might also have some effect on the determination of the temperature and emission measure of the source, which will be discussed in the following sections.

Due to the slow decay of Fe XVIII emission, we were able to make Fe XVIII images even at the time of *NuSTAR* observations one day after the flare onset (see Figure 4.2). The upper row presents the Fe XVIII maps of the flare onset, the post-flare loops 6 hr after the flare, and the remaining features 20 hr after the flare. Left and central panels in the bottom row present 25-minute integrated *NuSTAR* images above 2 keV from focal plane modules A (FPMA) and B (FPMB). Dashed lines denote the area covered by the gap during the observations that is further enlarged due to the drift of the telescope. As the drift was dominantly along the x -direction (45 arcsecs in total) and negligible in the y -direction, the area affected by the gap is much larger in the x -direction. The region of interest for the analysis that will be presented in the next section, with an area of $50'' \times 50'' = 2500''^2$, is marked by the white box. The last image in the bottom right corner is the 25-minute integrated (same time range as *NuSTAR*) Fe XVIII map of the source together with the 30%, 50%, 70% and 90% contours of *NuSTAR* emission in blue. As the uncertainty in *NuSTAR* absolute pointing accuracy is relatively large (see Hannah et al. 2016, Grefenstette et al. 2016), the *NuSTAR* image was shifted by $-100''$ and $25''$ in the x and y directions, respectively, in order to match the Fe XVIII source location. *NuSTAR* and Fe XVIII maps show the same sources, such as the top parts of the coronal loops, and the high emission source above them (MacCombie & Rust 1979).

In Figure 4.3 we present the *STEREO-A* image of the active region AR 12222 an hour before the *NuSTAR* observation. The green line shows the solar limb as viewed from the Earth, while the red line is a projection of the line-of-sight from the Earth to the *NuSTAR* source, passing right above AR 12222 located at $\sim[-730'', -330'']$ in the *STEREO-A* 195 Å image. The *NuSTAR* source is not evident in this image as the 195 Å channel is sensitive mainly to lower temperatures. From *STEREO* images, it is possible to calculate the height of the flare loops, defined as the distance between AR 12222 and the mid-point of the line that minimizes the distance between the Earth-Sun line of sight and the radial extension above the active region. We estimate this height to be $\sim 300''$. If we assume the height of the initially formed loops at the flare onset to be $50''$ (as there are no *STEREO* observations of this active region immediately after the flare, we assume this height as a common value for ordinary flares), this yields a radial velocity of $\sim 2 \text{ km s}^{-1}$ when averaged over the whole day. This is similar to typical speeds of rising flare loops very late in an event (e.g., MacCombie & Rust 1979; Gallagher et al. 2002), giving further evidence that the *NuSTAR* source is indeed associated with the flare that occurred a day earlier.

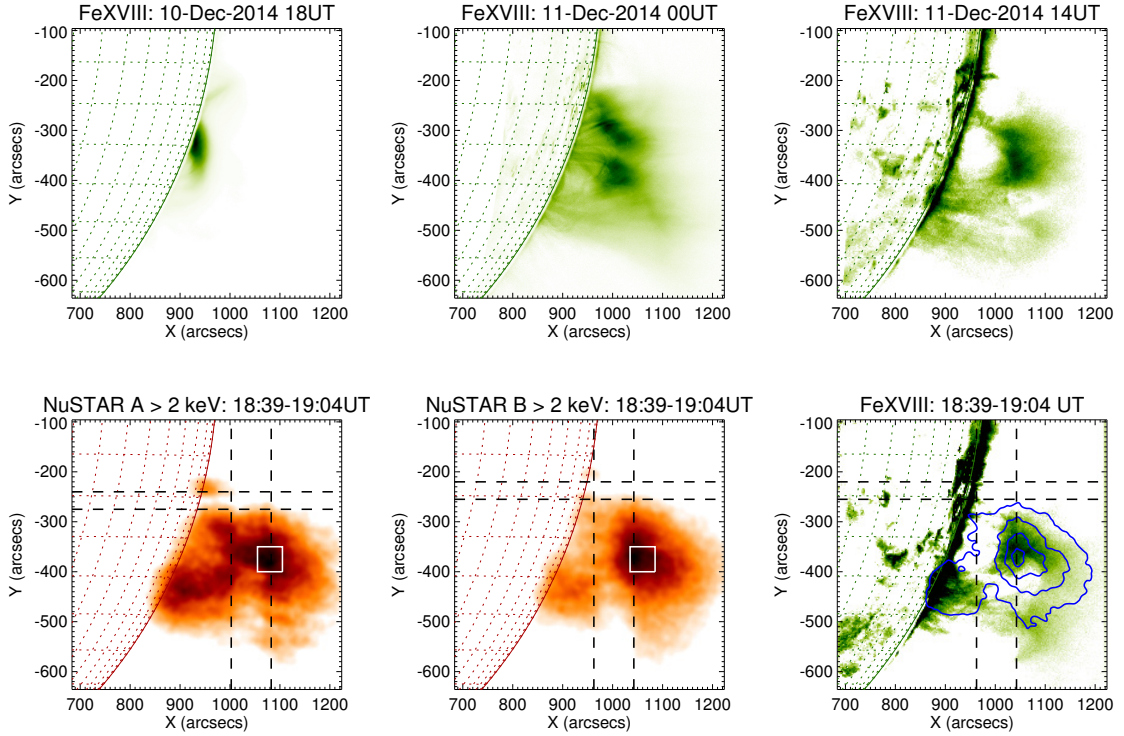


Figure 4.2: Upper row: Fe XVIII maps of the flare onset (left panel), post-flare loops 6 hours after the flare (central panel), and the remaining loops 20 hours after the flare (right panel). Bottom row: 25-minute integrated *NuSTAR* FPMA (left panel) and FPMB (central panel) and AIA Fe XVIII (right panel) maps; the latter includes the 30%, 50%, 70% and 90% *NuSTAR* contours in blue. Dashed lines denote the area affected by the *NuSTAR* chip gap during this observation. The white box is the region chosen for the spectral analysis.

4.3 Analysis of the high coronal source

4.3.1 Spectral fitting

We fitted the *NuSTAR* count spectrum inside the region of interest from Figure 4.2 separately for FPMA and FPMB, following the approach of Hannah et al. 2016, using SolarSoft/OSPEX³. The counts were binned with 0.2 keV energy resolution, while the integration time was 25 minutes (full *NuSTAR* observing time of the active region). As the livetime was around 1% during the whole observation period, this is roughly equal to 15 seconds of exposure at full livetime. In order to investigate the influence of the adopted energy range on the fitted temperature and emission measure, we fitted CHIANTI 7.1 isothermal models (Dere et al. 1997; Landi et al. 2013) to our data for different energy ranges: 2.5–5.2, 3.0–5.2, 3.5–5.2, 4.0–5.2 keV. These fits are presented in Figure 4.4. The lower limit of 2.5 keV was chosen as the lowest energy for which the calibration is still completely

³ <http://hesperia.gsfc.nasa.gov/ssw/packages/spex/doc/>.

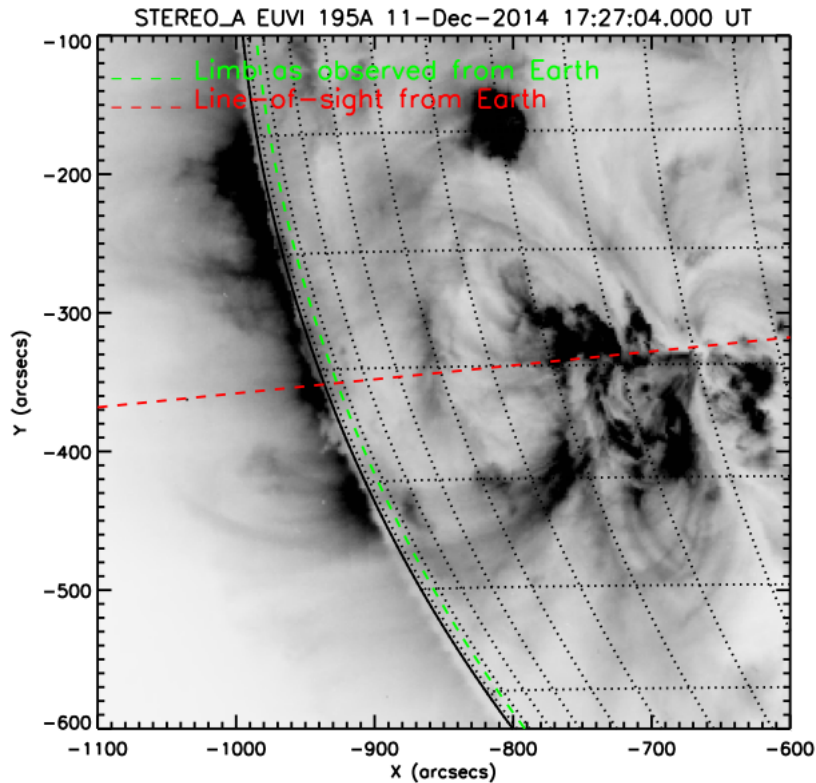


Figure 4.3: *STEREO-A* 195 Å image of active region AR 12222 an hour before the *NuSTAR* observations. The green line presents the solar limb as viewed from the Earth, while the red line is the line-of-sight from the Earth through the *NuSTAR* source.

understood and reliable (Grefenstette et al. 2016), while the upper limit of 5.2 keV was chosen as the highest energy with a significant number of counts (> 3 counts per bin). Both focal plane modules give consistent results, with temperature 3.8 – 4.6 MK and emission measure $0.3 \times 10^{46} \text{ cm}^{-3} - 1.8 \times 10^{46} \text{ cm}^{-3}$, depending on the lower limit of the energy range used in the fitting. The temperature gets higher and the emission measure gets lower as we go to higher energies. The 67% confidence ranges of temperature and emission measure were calculated using the standard Monte Carlo procedure in OSPEX and are given in Table 4.1 together with the best-fit values. A point to note is that our region of interest is located very close to the gap between the detectors, which leads to fewer counts, especially in later phases of the integration interval. The reason for this is the slow drift of the spacecraft pointing with time, resulting in covering a part of the region of interest by the chip gap. The missing counts could lead to an underestimation of the emission measure, but do not change the value of the determined temperature (as it is determined by the slope in the counts spectrum). A single temperature component is enough to fit the observations, similar to the results of Hannah et al. (2016). We determine the density of the source to be (assuming a volume of $50 \times 50 \times 50''^3$) in the range $2.5 - 6.0 \times 10^8 \text{ cm}^{-3}$ (roughly 10 – 100 times the density of the quiet Sun corona at this height; see e.g., Withbroe 1988), suggesting

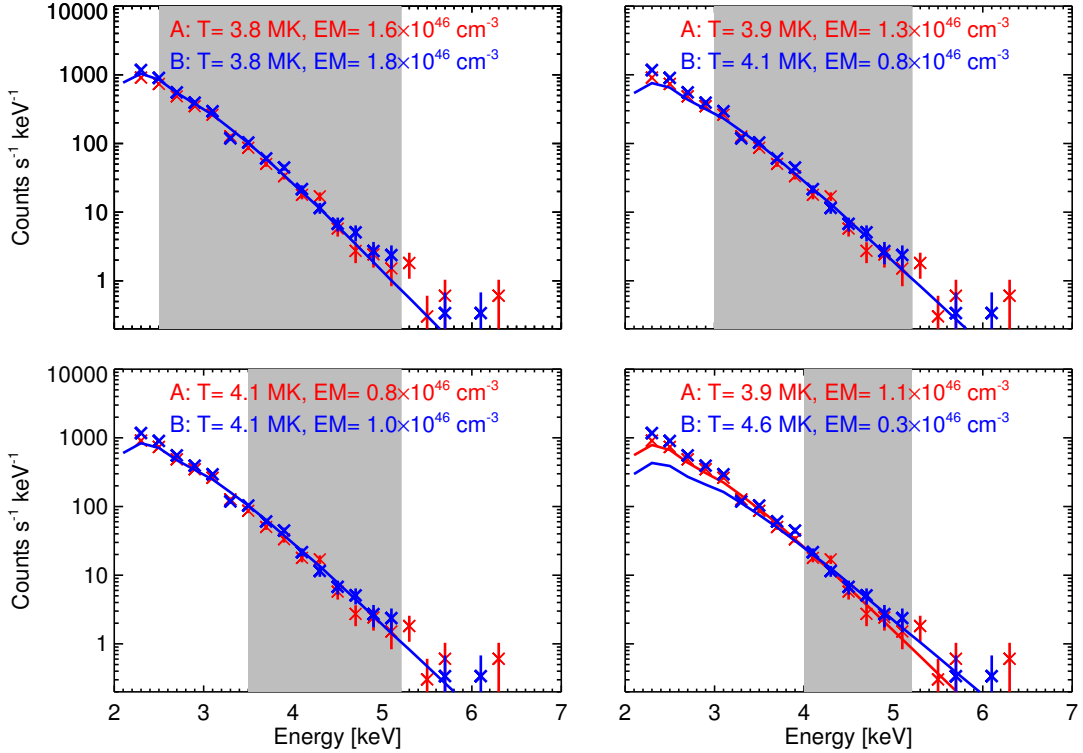


Figure 4.4: *NuSTAR* count spectra for FPMA (red) and FPMB (blue) integrated over the whole observation time range (18 : 39 – 19 : 04), together with isothermal fits for different energy ranges: 2.5 – 5.2 keV (*upper left*), 3.0 – 5.2 keV (*upper right*), 3.5 – 5.2 keV (*lower left*) and 4.0 – 5.2 keV (*lower right*). Energy ranges for spectral fitting are shown with grey shaded areas. The best-fit values of temperature and emission measure for individual focal plane modules can be found on the top of each graph.

the density of late-phase loops to be significantly higher than that of the quiet Sun corona.

4.3.2 Comparison of *NuSTAR* to *SDO/AIA*

4.3.2.1 Comparison to Fe XVIII

In order to investigate the extent of the agreement between *NuSTAR* and Fe XVIII sources, we compare the Fe XVIII loci curve with the *NuSTAR* loci curves in different energy channels. For reference, the results of *NuSTAR* spectral fitting from the previous section for both focal plane modules are presented in Figure 4.5 with different symbols for different energy ranges, together with the Fe XVIII and *NuSTAR* loci curves. The Fe XVIII loci curve is extracted from the temperature response functions (Boerner et al. 2014) and the observed fluxes using the following formula

$$EM = \frac{F \cdot S}{R(T)}, \quad (4.3)$$

| FPMA | | | | |
|--------------------------------|------------------------|------------------------|------------------------|------------------------|
| Energy range [keV] | 2.5 – 5.2 | 3.0 – 5.2 | 3.5 – 5.2 | 4.0 – 5.2 |
| T [MK] | $3.77^{+0.04}_{-0.04}$ | $3.86^{+0.09}_{-0.09}$ | $4.05^{+0.18}_{-0.16}$ | $3.94^{+0.43}_{-0.44}$ |
| EM [10^{46}cm^{-3}] | $1.60^{+0.14}_{-0.12}$ | $1.30^{+0.28}_{-0.23}$ | $0.82^{+0.36}_{-0.25}$ | $1.11^{+3.18}_{-0.72}$ |
| FPMB | | | | |
| Energy range [keV] | 2.5 – 5.2 | 3.0 – 5.2 | 3.5 – 5.2 | 4.0 – 5.2 |
| T [MK] | $3.79^{+0.04}_{-0.05}$ | $4.12^{+0.10}_{-0.10}$ | $4.06^{+0.16}_{-0.16}$ | $4.57^{+0.62}_{-0.45}$ |
| EM [10^{46}cm^{-3}] | $1.75^{+0.15}_{-0.12}$ | $0.84^{+0.17}_{-0.15}$ | $0.99^{+0.44}_{-0.28}$ | $0.30^{+0.77}_{-0.20}$ |

Table 4.1: Best-fit values of temperature and emission measure and their 67% confidence ranges.

where EM is the emission measure [cm^{-3}], F is the flux [$\text{DN s}^{-1}\text{pix}^{-1}$], S is the area of the region [cm^2] and $R(T)$ is the temperature response function of the Fe XVIII line [$\text{DN cm}^5 \text{s}^{-1} \text{pix}^{-1}$]. The *NuSTAR* loci curves are extracted in a similar way from the *NuSTAR* temperature response function, determined by folding the generated photon spectra for different temperatures through the *NuSTAR* response matrix. The good agreement of our results is best seen in the inset of Figure 4.5, where we plot the loci curves and the determined $EM - T$ pairs on linear scale. The intersection of the Fe XVIII loci curve with the *NuSTAR* loci curves in the temperature range 4.0 – 4.3 MK is consistent with the $EM - T$ pairs shown in Figure 4.4, except for the fit including the lowest energies. A part of these low energy counts might originate from cooler post-flare loops, which will be discussed in more detail in the next sections.

4.3.2.2 Comparison to other AIA channels

It is also possible to investigate the results of *NuSTAR* fitting to other AIA channels by calculating the expected count rates in different AIA channels from the source with the emission measure and temperature as given by *NuSTAR*, and compare them to the observed fluxes in AIA maps. The difficulty of this comparison is that the fraction of the cold background emission (in the temperature range below ~ 3 MK) in these channels is unknown and unremovable. This is not an issue for the derived Fe XVIII channel, which is not sensitive to this cooler plasma. The expected AIA fluxes are calculated by inverting Equation 4.3. This is a *NuSTAR*-predicted AIA flux coming from the *NuSTAR* source alone, without any additional contribution from the cooler plasma. The comparison between *NuSTAR*-predicted and observed fluxes is presented in Figure 4.6. The circles are the predicted fluxes for *NuSTAR* spectral fitting in the range 2.5 – 5.2 keV, and the stars for 4.0 – 5.2 keV. We use the fitted values of FPMB in both ranges, as

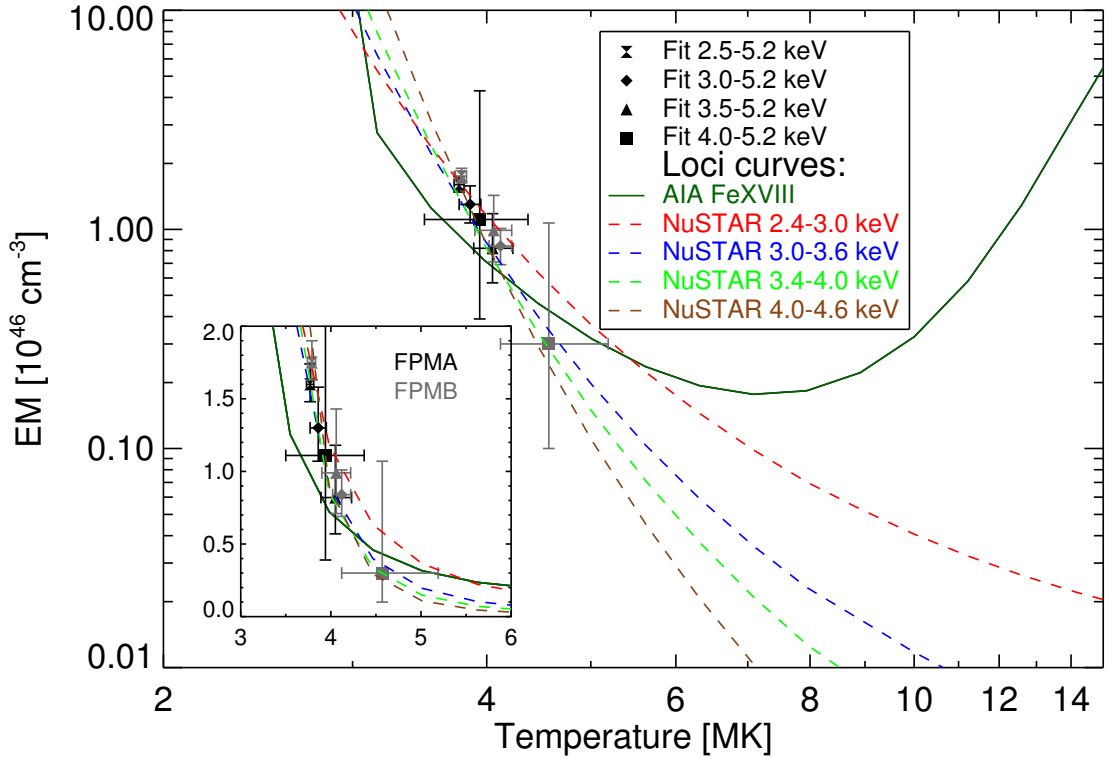


Figure 4.5: Comparison of Fe XVIII and *NuSTAR* loci curves. Temperatures and emission measures from the fits in different energy ranges are marked by symbols with corresponding confidence ranges in black (FPMA) and grey (FPMB). The inset represents the magnification of the given plot in the temperature range 3 – 6 MK, on a linear scale.

they represent the two extreme $T - EM$ fits. The full and dashed lines represent 1%, 5%, 10%, 50% and 100% ratios of *NuSTAR*-predicted and observed fluxes in different AIA channels. The area where the predicted AIA flux from the *NuSTAR* source is larger than the total observed flux is shown with the red lines. If the *NuSTAR*-predicted flux for a given AIA channel is close to the observed flux (e.g., region between 50% and 100% lines in the plot), the emission in that AIA channel is dominated by the same plasma that *NuSTAR* observes. Unsurprisingly, this is best achieved for the 94 Å channel and, consequently, the Fe XVIII channel. For the first $T - EM$ fit, the *NuSTAR*-predicted flux for the Fe XVIII channel is greater than the observed flux. This result indicates that a single temperature fit is not enough to fit the observations at the lowest energies, as some of the low-energy counts are produced by a lower temperature plasma. The ratio for the Fe XVIII channel for the fit at higher energies (second $T - EM$ fit) lies in the range between 50% and 100%, while the 335 Å channel and its derived Fe XVI channel have ratios in the range 5 – 10 %. These results are in agreement with the fact that the Fe XVIII source showed the same spatial features as the *NuSTAR* source, while we were not able to detect the Fe XVI source. Cooler lines at 171 Å, 211 Å and 193 Å have ratios of *NuSTAR*-predicted fluxes to the observed fluxes at a percent level,

which is expected as these lines are sensitive to plasma cooler than *NuSTAR* can observe.

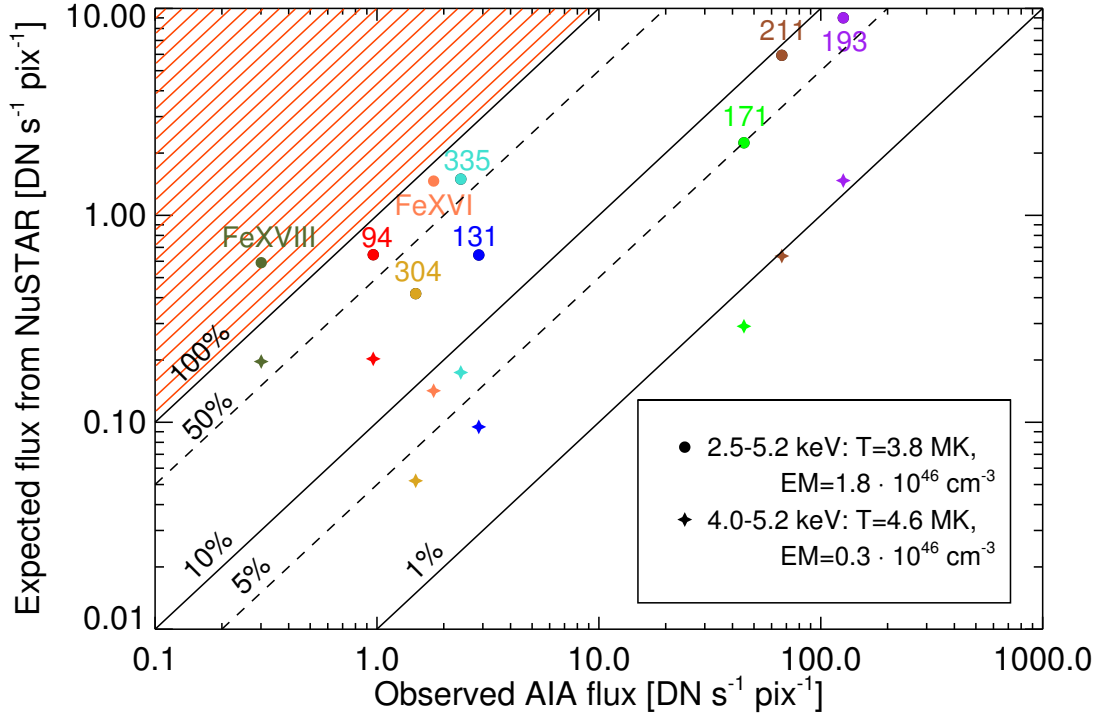


Figure 4.6: Comparison of expected and observed fluxes for 7 AIA channels and the derived Fe XVI and Fe XVIII channels, for the two extreme pairs of temperature and emission measure (values given in the legend) from the fits in Figure 4.4. The diagonal lines denote 1%, 5%, 10%, 50% and 100% ratios of the expected AIA fluxes from the *NuSTAR* source and the observed AIA fluxes. The red lines denote the (forbidden) area where the predicted AIA flux from the *NuSTAR* source is larger than the total observed AIA flux.

4.3.3 Comparison of *NuSTAR* to *FOXSI*

The *FOXSI* (Krucker et al. 2014) sounding rocket also uses direct focusing HXR optics similar to *NuSTAR*, but it is optimized especially for solar purposes. *FOXSI* has about one fifth of *NuSTAR*'s effective area with a higher spatial resolution (FWHM of $\sim 9''$). The main difference for solar observations between the two telescopes is the different low energy threshold. While *NuSTAR* detects photons down to ~ 2 keV, the *FOXSI* entrance window intentionally blocks the large number of low energy photons, giving a typical peak in the count spectrum around 5 keV. The entrance window largely reduces the number of incoming photons, keeping the livetime high for the faint, higher energy components. For example, a 25 minute observation by *NuSTAR* at 1% livetime and five times the effective area is equal to a *FOXSI* observation of 75 s at full livetime. However, this also

means that *FOXSI* is not sensitive to low temperature plasmas that are best seen below 4 keV.

The *FOXSI-2* rocket flew for a 6.5-minute observation interval during the *NuSTAR* solar pointing discussed here. *FOXSI-2* targeted AR 12222 for 35.2 seconds, though 12 minutes after the *NuSTAR* observation finished. As the *NuSTAR*/AIA source has a slow time variation, the time difference between the observations is of minor importance, at least for the order of magnitude estimate discussed here. Using the temperature and emission measure derived from *NuSTAR* ($T = 3.8$ MK and $EM = 1.7 \times 10^{46} \text{ cm}^{-3}$), the expected *FOXSI* total count rate is ~ 1.6 counts for the *FOXSI-2*'s most sensitive optics/detector pair D6. This value is computed above 5 keV and with the integration time of 35.2 seconds (integrating during the whole observation period). In total, 4 counts were observed by D6. This is a reasonable value given that the estimated non-solar background flux is 1.8 counts, while the expected count rate due to ghost-rays from sources outside of the FoV is unknown. Given the small-number statistics and the uncertainty of the ghost-ray background, the observed *FOXSI-2* measurement is consistent with the values expected for the plasma observed with *NuSTAR*, but does not provide any further diagnostics for this event.

4.4 Discussion and conclusions

In this chapter, we have presented the first observations of the EUV late-phase of a solar flare in X-rays with *NuSTAR*. *NuSTAR* has provided a unique opportunity to perform spectroscopy on X-rays from a coronal source a full day after the flare onset. With knowledge of the location of this faint source from *NuSTAR*, we were also able to find it in Fe XVIII by eliminating the lower temperature response of the AIA 94 Å channel and integrating for 25 minutes (adding together 125 maps to obtain a higher signal-to-noise ratio). Here, *NuSTAR* played a crucial role in providing the information needed for extracting the very faint signal which was far from evident in the 94 Å maps.

The fact that the flare loops have been observed so late in the flare evolution points to continuing energy input in the later phases of the solar flare evolution. To quantify this statement, we estimate the cooling times of subsequent flare loops and compare them to the flare duration. We follow the approach of Cargill et al. (1995), with the following formula for the cooling time of flare loops:

$$\tau_{cool} = 2.35 \cdot 10^{-2} \cdot L^{5/6} \cdot n_e^{-1/6} \cdot T_e^{-1/6}, \quad (4.4)$$

where τ_{cool} [s] is the cooling time (the time needed for flare loops to cool down to $\sim 10^5$ K) and L [cm], n_e [cm^{-3}] and T_e [K] are loop length, density and temperature at the start time. The temperature estimate of the initially formed flare loops from the *GOES* observations is 10.5 MK, while the emission measure is $5 \times 10^{48} \text{ cm}^{-3}$. Even though the above estimates might only be a rough approximation because of the high occultation of the flare, we are anyway making only an approximate calculation of the cooling time. By assuming the length of the

original flare loops to be $\sim 50''$, we estimate the density to be $9 \times 10^9 \text{ cm}^{-3}$. This gives us a cooling time of $\sim 1 \text{ hr}$, indicating that the original flare loops are long-gone at the time of *NuSTAR* observations and that the additional heating took place during the evolution of the flare system. The most probable explanation is the previously mentioned scenario of subsequent magnetic reconnections, resulting in reconnected loops being produced higher and higher in the corona.

The above results are in agreement with original *Skylab* and *Solar Maximum Mission* results, and the recent observations of a large flare loop system between 2014 October 14 – 16 by West & Seaton (2015). They conclude that the giant late-phase arches are similar in structure to the ordinary flare loops and formed by magnetic reconnection. Their reasoning follows the work of Forbes & Lin (2000), in which it is pointed out that the reconnection rate may not depend only on the magnetic field (in which case, it would decrease with height), but possibly on the local Alfvén speed, which is proportional to $B/\sqrt{\rho}$, where B is the magnetic field strength and ρ the density. So, if the density decreases sufficiently fast, the reconnection rate could remain constant out to $0.5R_{\odot}$ despite the decreasing magnetic field strength, and thus produce the giant flare loops analyzed by West & Seaton (2015) or in this study.

From *NuSTAR* and *GOES* data, it is possible to estimate the additional energy input needed to form the subsequent, rising flare loops. The total thermal energy of the loop system is proportional to the density, temperature and volume (e.g., Hannah et al. 2008):

$$E_{th} = 3NkT = 3k \cdot nVT, \quad (4.5)$$

while k is the Boltzmann constant. We have obtained all the above parameters for the original flare loops from *GOES* and for the post-flare loops a day after from *NuSTAR*. We estimate that the thermal energy content in *NuSTAR*-loops is 5% of the thermal energy content of the initially formed flare loops, indicating there is still significant energy release even a full day after the flare onset. Next, by assuming linearity in the change of density, loop length and temperature over time (for simplicity), it is possible to calculate the change in cooling times of all the post-flare loops formed in between. Although the above assumption might not be accurate for all (or any) of the parameters, we are only interested in calculating an order of magnitude estimate here. The other assumption we use is that new loop systems are only produced when the old ones vanish. This assumption is in principle not valid as new systems are produced while the old ones persist, but it gives us an approximate lower limit on the total thermal energy content in all the loops systems. The sequence is as follows: original post flare loops vanish after $\sim 1 \text{ hour}$, and during this time density, temperature and volume change as well, and a new loop system with a different cooling time is produced. We calculate that this sequence repeats about 12 times during the 24 hours between the flare onset and *NuSTAR* observations, with the total energy content in those 12 cycles of reconnection and cooling estimated at a factor of ~ 13 larger than the one released during the impulsive phase of the flare only.

Previous estimates of the additional energy input during the decay phase of solar flares were derived using radiative losses at specific wavelength ranges.

Woods et al. (2011) calculate the total radiated energy in the EUV band during the late phase to be between 0.4 and 3.7 times the flare energy in the X-rays during the peak. Emslie et al. (2012) conclude in their statistical study of 38 solar flares that, on average, the total energy radiated from hot SXR-emitting plasma exceeds the peak thermal energy content by a factor of ~ 3 . It is important to note that the above studies used non-overlapping wavelength ranges, thus missing the contribution to the total energy content from the wavelength range of the other study (and the rest of the wavelength spectrum). Our results for a single event are consistent with these statistical studies, especially as we compare our value with statistical averages that miss significant energy contributions.

In summary, all results indicate that the impulsive energy release is only a fraction of the energy release in the late phase of the flare evolution, at least for events with clearly observable late phase emission. This statement calls for re-examining the approach of using just the peak energy content or the nonthermal emission during the impulsive phase of the flare as the estimate of the total energy content of the flare. In order to assess this in more detail, a statistical study of similar events should be carried out. However, *NuSTAR* is not a solar-dedicated observatory, and therefore the observations are few and sporadic, making statistical studies difficult. Additionally, it is most likely that faint signals such as presented in this study can only be observed when the flare (and the active region) is occulted or at least over the limb, as the emission from these kinds of coronal sources on the disk would likely be masked by the much stronger emission of the active region beneath. Nevertheless, a statistical search for *SDO/AIA* Fe XVIII sources in above-the-limb flares could give us new insights about the influence of the long-lasting decay phase on flare energetics.

Bibliography

- Boerner, P. F., Testa, P., Warren, H., Weber, M. A., & Schrijver, C. J. 2014, *Sol. Phys.*, **289**, 2377
- Cargill, P. J., Mariska, J. T., & Antiochos, S. K. 1995, *ApJ*, **439**, 1034
- Del Zanna, G. 2013, *A&A*, **558**, A73
- Dere, K. P., Landi, E., Mason, H. E., Monsignori Fossi, B. C., & Young, P. R. 1997, *A&AS*, **125**, 149
- Emslie, A. G., Dennis, B. R., Shih, A. Y., et al. 2012, *ApJ*, **759**, 71
- Fárník, F., Švestka, Z., Hudson, H. S., & Uchida, Y. 1996, *Sol. Phys.*, **168**, 331
- Forbes, T. G. & Lin, J. 2000, *Journal of Atmospheric and Solar-Terrestrial Physics*, **62**, 1499
- Gallagher, P. T., Dennis, B. R., Krucker, S., Schwartz, R. A., & Tolbert, A. K. 2002, *Sol. Phys.*, **210**, 341
- Grefenstette, B. W., Glesener, L., Krucker, S., et al. 2016, *ApJ*, **826**, 20
- Hannah, I. G., Christe, S., Krucker, S., et al. 2008, *ApJ*, **677**, 704
- Hannah, I. G., Grefenstette, B. W., Smith, D. M., et al. 2016, *ApJL*, **820**, L14
- Harrison, F. A., Craig, W. W., Christensen, F. E., et al. 2013, *ApJ*, **770**, 103

BIBLIOGRAPHY

- Howard, T. A. & Harrison, R. A. 2004, *Sol. Phys.*, **219**, 315
- Hudson, H. S., Lemen, J. R., St. Cyr, O. C., Sterling, A. C., & Webb, D. F. 1998, *Geophys. Res. Lett.*, **25**, 2481
- Kopp, R. A. & Poletto, G. 1984, *Sol. Phys.*, **93**, 351
- Krucker, S., Christe, S., Glesener, L., et al. 2014, *ApJL*, **793**, L32
- Landi, E., Young, P. R., Dere, K. P., Del Zanna, G., & Mason, H. E. 2013, *ApJ*, **763**, 86
- Lin, R. P., Dennis, B. R., Hurford, G. J., et al. 2002, *Sol. Phys.*, **210**, 3
- Liu, K., Zhang, J., Wang, Y., & Cheng, X. 2013, *ApJ*, **768**, 150
- MacCombie, W. J. & Rust, D. M. 1979, *Sol. Phys.*, **61**, 69
- Madsen, K. K., Harrison, F. A., Markwardt, C. B., et al. 2015, *ApJS*, **220**, 8
- McIntosh, S. W., Leamon, R. J., Davey, A. R., & Wills-Davey, M. J. 2007, *ApJ*, **660**, 1653
- Nitta, N. V., Aschwanden, M. J., Boerner, P. F., et al. 2013, *Sol. Phys.*, **288**, 241
- Parenti, S., Reale, F., & Reeves, K. K. 2010, *A&A*, **517**, A41
- Reale, F., Guarrasi, M., Testa, P., et al. 2011, *ApJL*, **736**, L16
- Rust, D. M. & Hildner, E. 1976, *Sol. Phys.*, **48**, 381
- Stewart, R. T., McCabe, M. K., Koomen, M. J., Hansen, R. T., & Dulk, G. A. 1974, *Sol. Phys.*, **36**, 203
- Testa, P. & Reale, F. 2012, *ApJL*, **750**, L10
- Švestka, Z. 1984, *Sol. Phys.*, **94**, 171
- Švestka, Z., Dennis, B. R., Woodgate, B. E., et al. 1982, *Sol. Phys.*, **80**, 143
- Švestka, Z., Fárnik, F., Hudson, H. S., et al. 1995, *Sol. Phys.*, **161**, 331
- Warren, H. P., Winebarger, A. R., & Brooks, D. H. 2012, *ApJ*, **759**, 141
- West, M. J. & Seaton, D. B. 2015, *ApJL*, **801**, L6
- Withbroe, G. L. 1988, *ApJ*, **325**, 442
- Woods, T. N. 2014, *Sol. Phys.*, **289**, 3391
- Woods, T. N., Hock, R., Eparvier, F., et al. 2011, *ApJ*, **739**, 59
- Zarro, D. M., Sterling, A. C., Thompson, B. J., Hudson, H. S., & Nitta, N. 1999, *ApJL*, **520**, L139

Chapter 5

NuSTAR detection of X-ray heating events in the quiet Sun*

Matej Kuhar^{1,2}, Säm Krucker^{1,3}, Lindsay Glesener⁴, Iain G. Hannah⁵, Brian W. Grefenstette⁶, David M. Smith⁷, Hugh S. Hudson^{3,5}, Stephen M. White⁸

Abstract

The explanation of the coronal heating problem potentially lies in the existence of nanoflares, numerous small-scale heating events occurring across the whole solar disk. In this chapter, we present the first imaging spectroscopy X-ray observations of three quiet Sun flares during the *Nuclear Spectroscopic Telescope ARray* (*NuSTAR*) solar campaigns on 2016 July 26 and 2017 March 21, concurrent with the *Solar Dynamics Observatory*/Atmospheric Imaging Assembly (*SDO*/*AIA*) observations. Two of the three events showed time lags of a few minutes between peak X-ray and extreme ultraviolet (EUV) emissions. Isothermal fits with rather low temperatures in the range 3.2 – 4.1 MK and emission measures of $(0.6 - 15) \times 10^{44} \text{ cm}^{-3}$ describe their spectra well, resulting in thermal energies in the range $(2 - 6) \times 10^{26} \text{ erg}$. *NuSTAR* spectra did not show any signs of a nonthermal or higher temperature component. However, since the estimated upper limits of (hidden) nonthermal energy are comparable to the thermal energy estimates, the lack of a nonthermal component in the observed spectra is not a constraining result. The estimated *Geostationary Operational Environmental Satel-*

* This chapter has been published in *The Astrophysical Journal Letters*, **856**, 32 (2018)

¹ University of Applied Sciences and Arts Northwestern Switzerland, Bahnhofstrasse 6, 5210 Windisch, Switzerland

² Institute for Particle Physics and Astrophysics, ETH Zürich, 8093 Zürich, Switzerland

³ Space Sciences Laboratory, University of California, Berkeley, CA 94720-7450, USA

⁴ School of Physics and Astronomy, University of Minnesota - Twin Cities, Minneapolis, MN 55455, USA

⁵ SUPA School of Physics & Astronomy, University of Glasgow, Glasgow G12 8QQ, UK

⁶ Cahill Center for Astrophysics, 1216 E. California Blvd, California Institute of Technology, Pasadena, CA 91125, USA

⁷ Physics Department and Santa Cruz Institute for Particle Physics, University of California, Santa Cruz, 1156 High Street, Santa Cruz, CA 95064, USA

⁸ Air Force Research Laboratory, Albuquerque, NM, USA

lite (GOES) classes from the fitted values of temperature and emission measure fall between 1/1000 and 1/100 A class level, making them 8 orders of magnitude fainter in soft X-ray flux than the largest solar flares.

5.1 Introduction

The explanation of how the corona keeps its temperature of a few million Kelvin, termed the ‘coronal heating problem’, has eluded scientists for decades. Because solar flares release energy and heat ambient plasma, it is argued that they may provide (at least a part of) the needed energy to sustain coronal temperatures.

Solar flares follow a negative power-law frequency distribution with increasing energy, with a power-law index ~ 2 (e.g., Hudson 1991; Hannah et al. 2008). A flat distribution, with a power-law index below 2, implies that smaller events do not dominate the energy released in flares. Since the largest flares do not occur frequently enough to heat the solar corona, it has been instead argued that smaller-scale reconnection events could have a steeper frequency distribution, providing the needed energy input due to large numbers. Parker (1988) introduces the term *nanoflares* for such events, with energies speculated to be of the order of 10^{24} erg or less, as estimated from ultraviolet fluctuations within active regions (Porter et al. 1984). This triggered many theoretical studies on the role of small-scale events in coronal heating (e.g., Walsh & Ireland 2003; Klimchuk 2006; Browning et al. 2008; Tajfirouze & Safari 2012; Guerreiro et al. 2015; 2017).

Parker’s basic magnetic energy releases, however, are yet to be confirmed observationally, most probably due to their modest sizes and energies, combined with sensitivity limitations of present solar instruments. So far, only measurements of individual events down to $\sim 10^{24}$ erg (at the ‘high-energy’ end of Parker’s estimate) have been performed, while less energetic nanoflares could have even smaller energies and should form an ensemble of indistinguishable reconnection and heating processes that make the solar corona. In addition to searches for nanoflares in soft X-rays (SXR; e.g., Shimizu & Tsuneta 1997; Katsukawa & Tsuneta 2001; Terzo et al. 2011), the most complete statistical study of microflares in hard X-rays is by Hannah et al. (2008), using 6 years of *Reuven Ramaty High Energy Solar Spectroscopic Imager* (RHESSI, Lin et al. 2002) data and including more than 25 000 microflares. However, because RHESSI is sensitive to flares with temperatures above ~ 10 MK and emission measures (EMs) above 10^{45} cm^{-3} , the events included in the above study are much larger and more energetic than nanoflares proposed by Parker (1988). Another distinctive feature is that RHESSI observes microflares only from active regions, while nanoflares should occupy the whole solar disk. Quiet Sun (QS) flares, on the other hand, have been observed only in soft X-rays (SXR) and extreme ultraviolet (EUV) narrow-band filter observations (e.g., Krucker et al. 1997; Krucker & Benz 1998; Parnell & Jupp 2000; Aschwanden et al. 2000). These brightenings have been found to occur on the magnetic network of the QS corroborating the magnetic energy releases as their drivers. Radio events in the GHz range associated with

the EUV brightenings have been speculated to be signatures of nonthermal electrons accelerated during the energy release process (Benz & Krucker 1999). Their spectroscopic X-ray signatures, however, are too faint for the state-of-the-art solar X-ray instruments. Therefore, in order to confirm Parker’s nanoflare scenario of coronal heating, it is crucial to perform sensitive imaging spectroscopy X-ray observations of small-scale events across the whole solar disk.

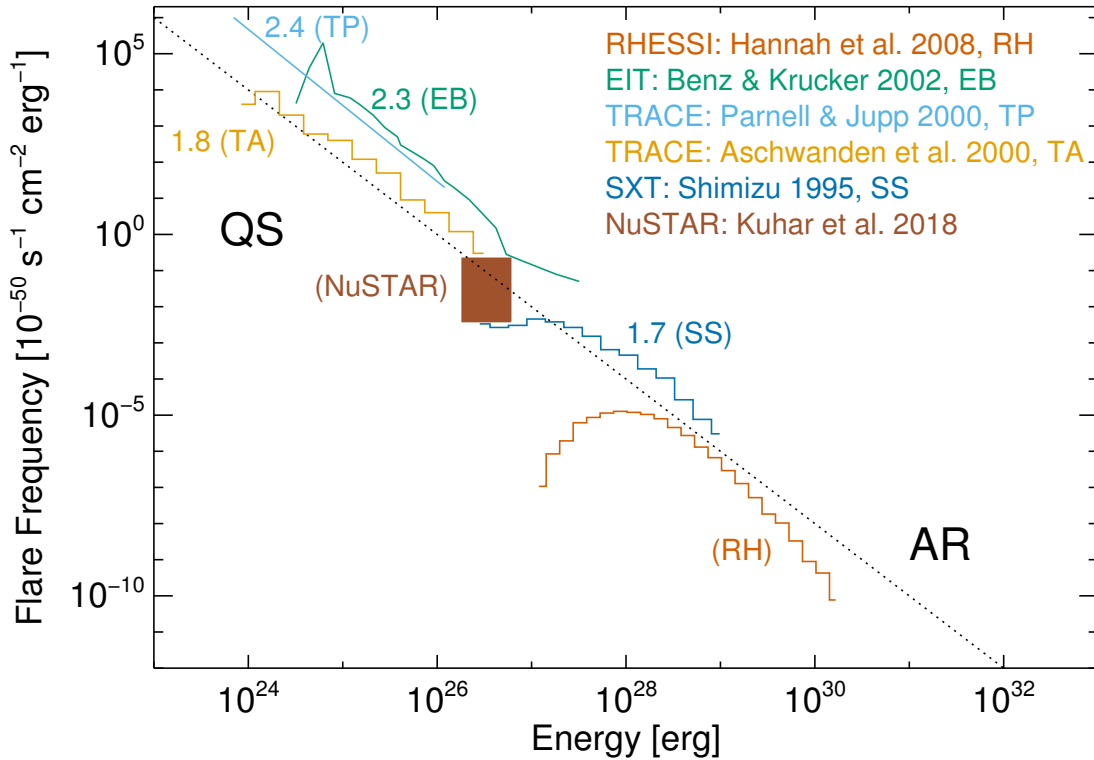


Figure 5.1: Flare frequency distribution vs. energy from various X-ray and EUV studies. *NuSTAR* observations analyzed in this chapter are presented as the brown rectangle. Note that the presented studies used data from different phases of the solar cycle, making comparisons of the flare occurrence between them difficult. The dotted line shows one frequency distribution with a power-law index of 2 to guide the eye. Taken from Hannah et al. (2011) and adapted to include our results.

The *Nuclear Spectroscopic Telescope ARray* (*NuSTAR*) is a focusing optics hard X-ray telescope launched in 2012 and operating in the energy range 3 – 79 keV (Harrison et al. 2013). Even though it is not solar-dedicated, it is capable of observing the Sun (Grefenstette et al. 2016), providing much higher sensitivity compared to indirect imaging telescopes such as *RHESSI*. It can therefore bridge the gap toward imaging spectroscopy in X-rays of small-scale heating events in the QS, and provide the opportunity to search for nonthermal signatures in them. This can be seen in Figure 5.1, where we show flare frequency distributions from various X-ray and EUV studies of microflares and QS brightenings (Shimizu 1995; Aschwanden et al. 2000; Parnell & Jupp 2000; Benz & Krucker 2002; Hannah et

al. 2008). The plot can be divided into two segments, the left one showing EUV observations of flares in the QS and the right one showing X-ray observations of microflares from active regions. QS *NuSTAR* observations from this study are shown by the brown box.

In this chapter, we present the first spectroscopically resolved X-ray measurements of QS flares. *NuSTAR* observations of QS heating events are described in Section 5.2. Data analysis and spectral fitting of the events are found in Section 5.3, while the discussion on this and possible future studies is presented in Section 5.4.

5.2 Observations

The data analyzed in this chapter were obtained in *NuSTAR* solar campaigns carried out on 2016 July 26 and 2017 March 21². Three QS events were observed during 1.5 hr of analyzed *NuSTAR* observations, one on 2016 July 26 and two others on 2017 March 21. They will be referred to as flares 1, 2 and 3 in the future sections, based on their chronological order.

Figure 5.2 shows the spatial structure and time evolution for each of the events. The left panels show the Atmospheric Imaging Assembly (AIA; Lemen et al. 2012) 335 Å images of the part of the solar disk where the events occurred, together with the 30%, 50% and 70% *NuSTAR* contours in red. *NuSTAR* images have been shifted to match the flare locations in AIA images in order to accommodate for uncertainties in absolute pointing (Grefenstette et al. 2016). A zoomed-in image of each event is shown in the inset. The right panels show the time evolution of *NuSTAR* flux above 2.0 keV, as well as the time evolution of AIA EUV channels. All fluxes are background-subtracted, where background is defined as the lowest emission time frame during the pre-event phase.

5.2.1 Time evolution

The time profiles of flares generally reveal different behaviors for the thermal and nonthermal X-ray component. Nonthermal emissions are most prominently observed during the rise phase of the thermal emission (‘impulsive phase’) and can show several peaks with individual durations from a minute down to a sub-second time scale (e.g., Aschwanden et al. 1995). The main thermal emission evolves more gradually, with a time profile often similar to the integrated non-thermal flux (the so-called ‘Neupert effect’, Neupert 1968). (Hard) X-ray peaks that occur before the thermal peak (seen in SXR and/or EUV) are therefore often interpreted as a signature of nonthermal emission (Veronig et al. 2005), but such a classification is not conclusive. Time lags between X-ray and EUV emission can also be produced by the different temperature sensitivity of X-ray and EUV observations: the X-ray peak is produced by the flare-heated plasma, which then

² Extensive information about all *NuSTAR* solar campaigns can be found at: http://ianan.github.io/nsigh_all/.

cools to lower temperatures visible in EUV. To resolve the ambiguities present in the time evolution of X-ray and EUV emission, a spectral analysis is required. In the following, we discuss the time evolution of the individual events focusing on potential nonthermal signatures, followed by the spectral analysis in Section 5.3.

Flare 1 shows an intriguing time evolution with two distinctive X-ray peaks, while flares 2 and 3 have one broad peak dominating both the X-ray and EUV evolution. Flare 3 shows simultaneous X-ray and EUV peaks, in contrast to flares 1 and 2 which show a time lag of a few minutes between peak X-ray and EUV emissions. The rise of the EUV emission, as well as the decay, is slower than in X-rays for all flares. In order to interpret the observed relative timing, it is important to consider the difference in temperature responses between *NuSTAR* and AIA. *NuSTAR* has a steeply increasing response toward higher temperatures between 1 and 10 MK, making it sensitive primarily to the highest temperature plasma in this range. The AIA temperature response, on the other hand, is much broader and the resulting flux represents contributions from plasma at various temperatures. The time evolution of flare 2 can be explained by the process of plasma cooling, where *NuSTAR* peaks first, followed by the AIA channels according to their temperature sensitivity. The other events are more complex, and only a detailed temporal and spatial differential emission measure analysis might allow us to understand their complicated time evolution, but this is outside the scope of this chapter. The spectral analysis presented in Section 5.3 further addresses the question of whether the delays between *NuSTAR* and AIA peaks imply nonthermal emission in these events.

5.2.2 Flare locations and morphology

Flare locations and morphologies can be found in the insets of the left panels in Figure 5.2. Flare 1 evidenced an ejection of material during the impulsive phase, seen in all AIA channels. It occurred in the QS. Flare 2 was a part of a long lasting, elongated structure located in proximity to the solar disk center, with the flaring area that was just a fraction of the whole structure. The morphology of the structure is reminiscent of heated flare loops. Flare 3 was a short-duration event that, like flare 1, was not associated with any kind of X-ray or EUV structure. However, it showed an even more complex structure than flare 1. The March events were clearly associated with the quiet Sun magnetic network structures, while the association is not as clear for the July event. However, this might be due to its proximity to the solar disk, where the line of sight effects could mask the signal.

To conclude, in spite of their modest sizes and emission, the observed events show very complex spatial and temporal morphologies and therefore cannot be described as “elementary” energy releases proposed by Parker. They were not part of active regions, and are therefore classified as QS events.

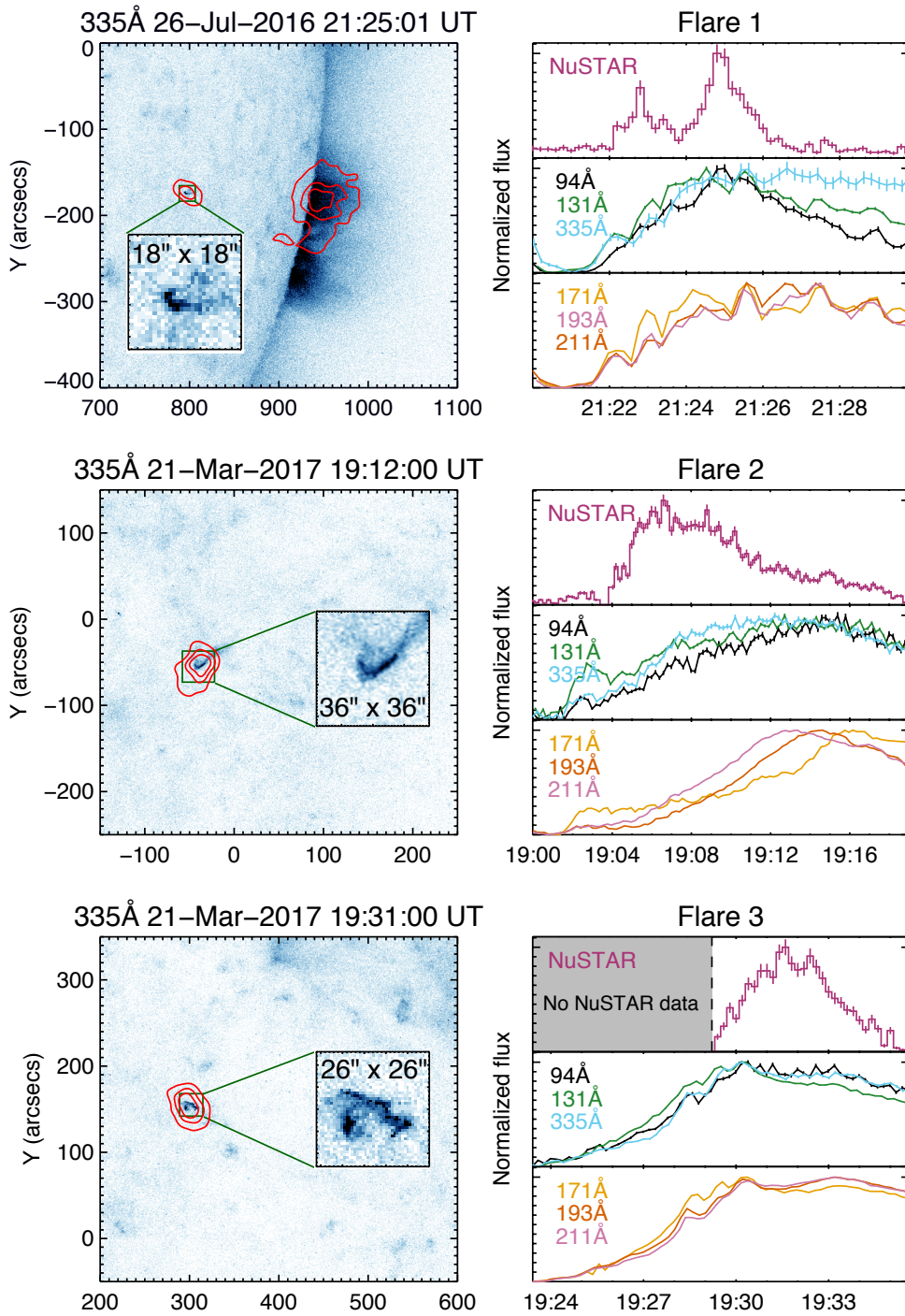


Figure 5.2: Overview plots of the three QS flares. *Left panels:* $400'' \times 400''$ AIA 335 Å images of the events, together with zoomed-in images of the event morphology in the insets. The 30%, 50% and 70% contours of maximum *NuSTAR* emission are shown in red. *Right panels:* Background-subtracted time evolution of the flaring region and flux uncertainties in the combined flux of *NuSTAR* focal plane modules A and B above 2.0 keV together with AIA 94, 131, 335, 171, 193 and 211 Å channels. Error bars in 171, 193 and 211 Å channels are smaller than the line thickness.

5.3 Data Analysis

5.3.1 Spectra

NuSTAR allows us to produce spectra for any time range, energy range (above 2.5 keV), and area. For our study, we use circular regions with diameter 55'' (a value close to *NuSTAR*'s half power diameter) at each flare's location. Integration times were chosen individually for each flare so that the majority of X-ray emission is included (presented spectra are flare-integrated) and are equal to 4, 8, and 3 minutes for flares 1, 2, and 3, respectively. To perform spectral fitting in XSPEC (Arnaud 1996), *NuSTAR* spectra and response matrix files were obtained using standard *NuSTAR* data analysis software³. In the following, we perform simultaneous fitting in XSPEC on the data from both focal plane modules, which are then combined to display the results shown in Figure 5.3 and Table 5.1. We fit an isothermal (APEC in the XSPEC package, using abundances from Feldman et al. 1992) plus a fixed background model between 2.5 and 5.0 keV, where we estimate the background as a 2-minute integrated emission in the pre-flare phase, mostly consisted of ghost-rays (photons from sources outside the field of view).

NuSTAR spectra are shown in Figure 5.3. The fits give temperatures of $3.96^{+0.05}_{-0.40}$, $4.01^{+0.05}_{-0.22}$ and $3.28^{+0.13}_{-0.06}$ MK, while their EMs lie in the range $5.6 \times 10^{43} - 1.5 \times 10^{45} \text{cm}^{-3}$. These values of temperature and EM place our events just in between the active region microflares and the QS events analyzed previously in the EUV. Our events are at or slightly below the *NuSTAR* detection limit, as derived from previous observations with lower livetime and much stronger ghost-ray signal (Marsh et al. 2017). Here we note that the estimated EM for flare 2 is probably a lower limit, as we estimate that up to 50% of the total flare emission might not be accounted for in our fits. This is due both to its proximity to the chip gap and a lot of changes in the combination of *NuSTAR* camera head units (CHUs) used for pointing, which resulted in many (abrupt) changes in the estimated flare location. This has probably no effect on the temperature estimates, but the actual EM is likely a factor of 2 larger than the one reported. This is also shown in Table 5.1, with a factor 2 in parenthesis for parameters affected by this effect. The above-reported temperatures and EMs place the observed events in the estimated range between 1/1000 and 1/100 GOES A-class equivalents, or between 7 and 8 classes fainter than the largest solar flares.

It is interesting to note the low temperatures of *NuSTAR* QS flares. While *RHESSI* is designed to observe flares with temperatures above 10 MK, *NuSTAR* is able to observe lower temperatures due to its higher low-energy sensitivity. However, because *NuSTAR*'s sensitivity also increases with increasing temperature, the fit-determined temperatures are the highest temperatures (as weighted by emission measure) present in the events. Therefore, it seems that QS flares reach only modest temperatures compared to those generally observed in regu-

³ <https://heasarc.gsfc.nasa.gov/docs/nustar/analysis/>

lar active region flares. The only other possibility is that hotter QS events have significantly lower EMs, making them difficult to observe even with *NuSTAR*.

5.3.2 Thermal energy content

We use the standard approach of estimating total thermal flare energy content from the flare plasma at the highest temperature as derived from *NuSTAR* spectra. This approach assumes that any cooler plasma, such as that observed in the EUV, is a result of the cooling process. Wright et al. (2017) estimated that this approximation could be up to $\sim 30\%$ different from the estimate from a complete, differential emission measure analysis of multithermal plasma in an active region microflare observed with *NuSTAR* and AIA. In this approximation, the thermal energy content of an event with temperature T , emission measure EM and volume V is given by the formula (e.g., Hannah et al. 2008):

$$E_{th} \sim 3NkT = 3kT\sqrt{EM \cdot V}. \quad (5.1)$$

To estimate upper and lower limits on the total thermal energy content, we use the combination of maximum and minimum of possible values for temperature and EM as given by the fits.

Because the observed QS flares are not spatially resolved with *NuSTAR*, we estimate flare volumes as the area of flaring 335 Å pixels (other channels have similar flaring areas) to the power of 3/2. As *NuSTAR* is only sensitive to the hottest plasma, while AIA is sensitive to a broader range of temperatures, this estimate provides an upper limit for the actual volume and, consequentially, a lower limit for the density and an upper limit for the thermal energy content (an overestimate up to a factor of 5 in the thermal energy content is possible). Density estimates can be calculated with the formula $n = \sqrt{EM/V}$ and fall in the range $(0.5 - 4) \times 10^9 \text{ cm}^{-3}$. These values are similar to those derived from SXR QS flares by Krucker et al. (1997) $((1 - 5) \times 10^9 \text{ cm}^{-3})$, but larger than densities derived from EUV QS events by Aschwanden et al. (2000) $((0.2 - 0.9) \times 10^9 \text{ cm}^{-3})$. We calculate the following thermal energy contents for flares 1, 2 and 3: $(3.8 - 6.0) \times 10^{26}$, $(1.8 - 2.5) \times 10^{26}$, and $(3.9 - 5.9) \times 10^{26}$ erg. These values are about 5 orders of magnitude smaller than in largest solar flares.

5.3.3 Nonthermal emission

There is no evidence for a high temperature or a nonthermal component in the spectra presented in Figure 5.3, and no counts above ~ 5 keV are observed. By setting an upper limit for the potentially hidden nonthermal contribution, we estimate an upper limit of the energy in nonthermal electrons in the same way as has been done in Wright et al. (2017) and taking flare 1 as an example. The addition of a hidden nonthermal component with a low-energy cutoff at 5 keV and a power-law index of 7 still reproduces the observed spectrum well, giving undetectable signal above the cutoff. The estimated upper limit of the nonthermal energy equals $\sim 5 \times 10^{26}$ erg, a value within the uncertainties of the estimated

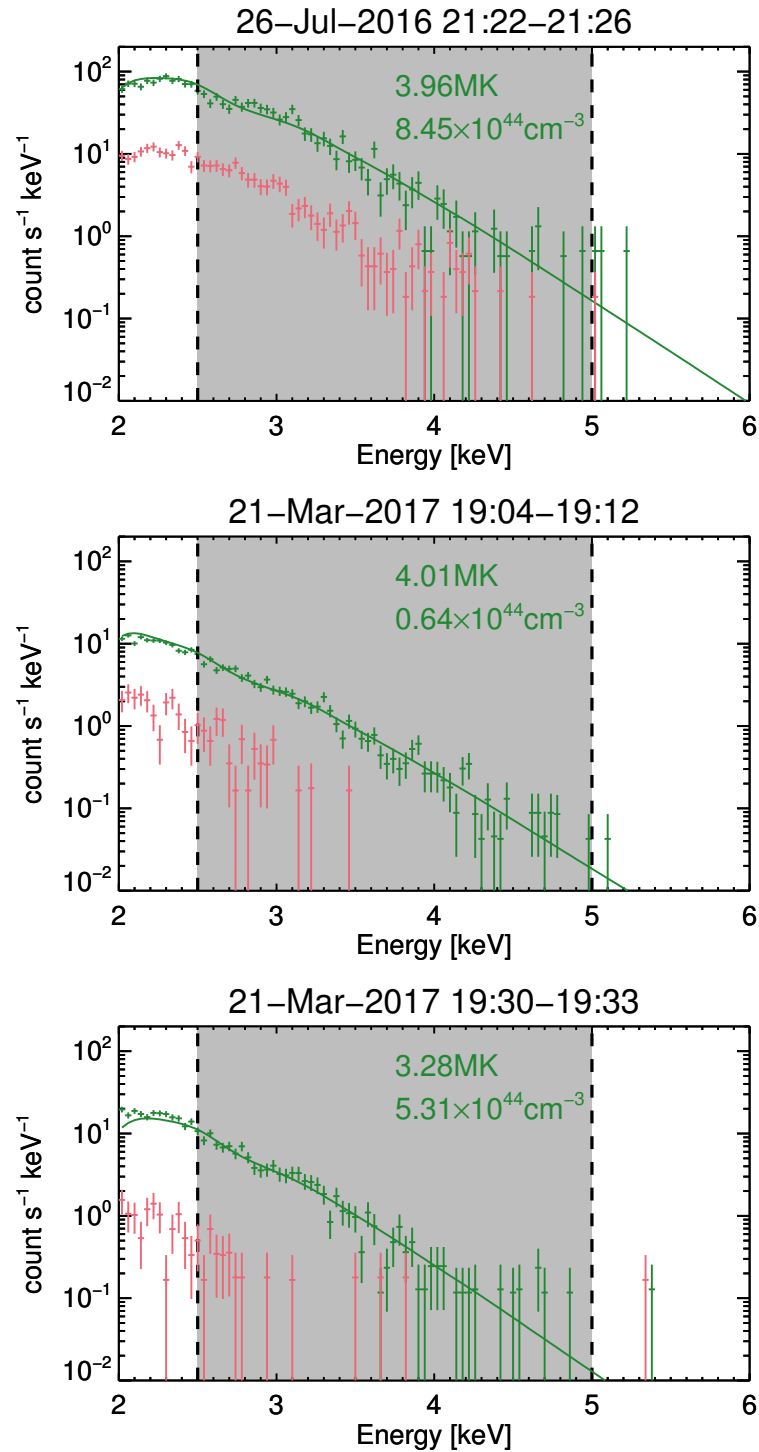


Figure 5.3: *NuSTAR* spectra of the observed QS flares. Spectra with best isothermal fits for *NuSTAR* focal plane modules A and B combined is shown in dark green, while the background counts are shown in pink. The energy range 2.5 – 5.0 keV used for spectral fitting is denoted by the gray area between the vertical dashed lines.

| Flare | Date [yyyy/mm/dd] | Time [hh:mm] | Location [x, y] | Area [arcsec ²] | Temperature [MK] |
|-------|----------------------|-----------------|--------------------|--------------------------------|------------------------|
| 1 | 2016/07/26 | 21:24 | [795, -175] | 38 | $3.96^{+0.05}_{-0.40}$ |
| 2 | 2017/03/21 | 19:04 | [-40, -55] | 75 | $4.02^{+0.05}_{-0.22}$ |
| 3 | 2017/03/21 | 19:30 | [300, 150] | 85 | $3.28^{+0.13}_{-0.06}$ |

| Flare | Emission measure [10 ⁴⁴ cm ⁻³] | Density [10 ⁹ cm ⁻³] | Energy 10 ²⁶ [erg] | GOES class [A] |
|-------|--|--|--------------------------------------|--------------------|
| 1 | $8.5^{+6.3}_{-0.9}$ | $3.0^{+1.0}_{-0.2}$ | $4.5^{+1.5}_{-0.7}$ | 0.01 |
| 2 | $(2\times) 0.64^{+0.22}_{-0.08}$ | $(\sqrt{2}\times) 0.51^{+0.08}_{-0.03}$ | $(\sqrt{2}\times) 2.1^{+0.4}_{-0.2}$ | $(2\times) 0.0009$ |
| 3 | $5.3^{+1.8}_{-1.8}$ | $1.3^{+0.2}_{-0.3}$ | $4.9^{+1.0}_{-1.0}$ | 0.003 |

Table 5.1: QS flare parameters.

thermal energy contents in Section 5.3.2. Hence, the non-detection of a nonthermal component in the observed spectra is not a constraining result, with its upper limits still consistent with the observed heating.

5.4 Discussion and conclusions

In this chapter, we analyzed three QS flares observed in X-rays above 2.0 keV with *NuSTAR*. We were able to measure their X-ray spectra for the first time and derive flare peak temperatures (see Table 5.1 for the summary of the derived parameters). Despite their modest sizes and X-ray emission, these events show very complex spatial morphologies in the EUV. They are therefore not elementary energy releases and still much larger than Parker’s idea of nanoflares.

Figure 5.4 shows our events in the T –EM parameter space, together with two *NuSTAR* active region microflares observed in previous campaigns (Glesener et al. 2017; Wright et al. 2017). The green box represents SXR QS events from Krucker et al. (1997), showing that they reach even lower temperatures and that they are below the sensitivity limits of our current *NuSTAR* observations. The isocurves show *GOES* classes, while the yellow area denotes the parameter space observable by *RHESSI*. For flares with temperatures between 3 and 4 MK as discussed here, *RHESSI* is sensitive to EMs above $\sim 10^{49}$ cm⁻³, meaning we gained

at least four orders of magnitude in EM sensitivity compared to *RHESSI*. Another interesting result are the rather low temperatures of up to ~ 4 MK, indicating that QS flares might be reaching lower temperatures than the ones generally observed in active region flares.

In contrast to hints coming from the time evolution of *NuSTAR* and AIA fluxes, *NuSTAR* spectra did not show any sign of a high-temperature or a non-thermal component. However, as the estimated upper limits of energy in the hidden nonthermal component are comparable to the calculated thermal energies, the lack of a nonthermal component is not a strong diagnostic result.

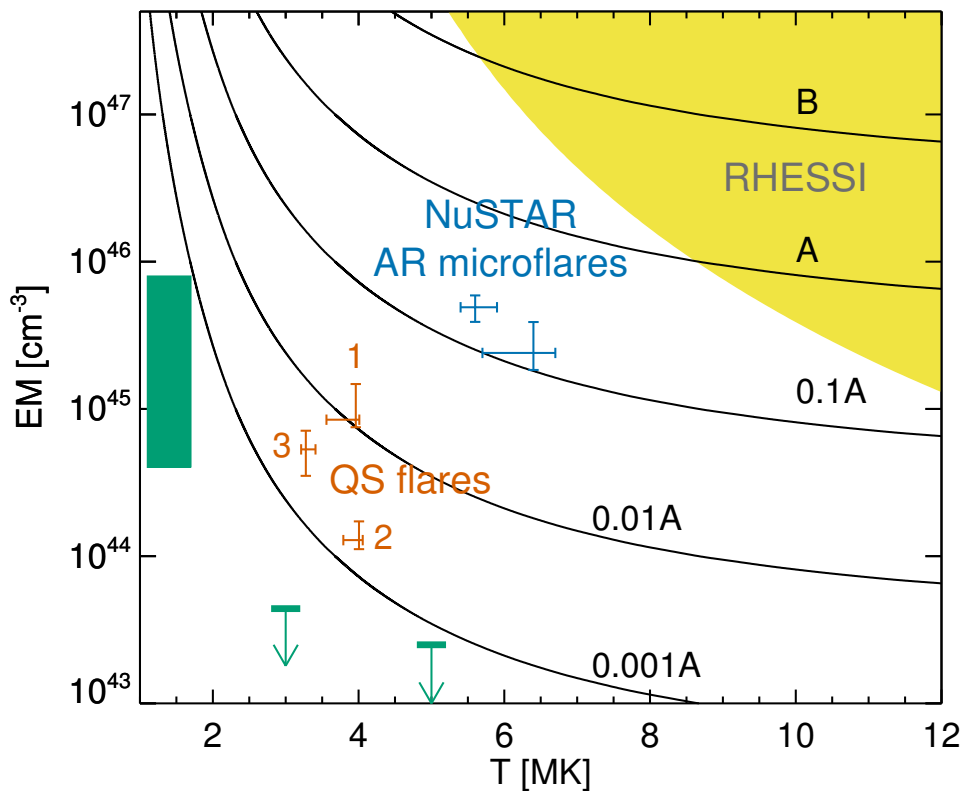


Figure 5.4: Three analyzed events (orange) in the T –EM parameter space, together with two active region microflares (blue) observed in previous *NuSTAR* solar campaigns. The QS network flares observed with *Yohkoh*/Soft X-Ray Telescope (SXT; Krucker et al. 1997) are depicted with the green box, together with the estimated upper limits in the temperature range of our QS events. *GOES* classes between 0.001A and B are shown by isocurves. The part of the parameter space observable by *RHESSI* is shown in yellow.

What follows next? Solar observations with *NuSTAR* started in 2014 September and have been carried out sporadically every few months, depending on science questions addressed and solar conditions, giving 12 observations in total at the time of writing. Taking into account the EUV QS flare frequency distribution (Figure 5.1), we expect a few QS events of energies $\sim 10^{26}$ erg per hour within the *NuSTAR* field of view. This is roughly in agreement with our observations

BIBLIOGRAPHY

of 3 events in 1.5 hours of data. We overlay our observations in the frequency distribution plot in Figure 5.1 as a brown shaded box. The height of the box represents uncertainty in determining the number of events in the low-statistics regime following the approach of Gehrels (1986) and taking the conservative 99% confidence interval, while the width of the box represents the thermal energy range of our events.

As the Sun's activity decreases toward solar minimum in 2019/2020, we expect progressively better conditions for observations of QS flares. We can get an estimate of this by inspecting detector livetimes and count rates of the observed events. The data for flare 3 are taken here as an example. We emphasize the following points that will improve the sensitivity during optimal observing conditions:

1. Livetime could improve by a factor of $1/0.59 \approx 1.7$ in periods of low solar activity.
2. *NuSTAR* detected 900 counts above 2.5 keV during the event, with background contributing $\sim 3\%$ of the emission (see Figure 3). In the absence of any activity during solar minimum observations, we expect ghost-rays to largely disappear, reducing the background emission to values that are close to zero. The spectral analysis could then be performed with many fewer counts than we observed for flare 3; an improvement in sensitivity of up to a factor of 10 seems feasible.
3. Counts below 2.5 keV, where *NuSTAR* calibration is less accurate due to threshold uncertainties and ghost-ray influence is strongest, have not been used for spectral fitting. In the absence of ghost-rays, however, using counts down to 1.6 keV can be used for flare detection. While spectral fitting will be affected by uncertainties in calibration below 2.5 keV, we might still get acceptable energy estimates. Moving the lower energy limit down to 1.6 keV would increase our statistics by a factor of 4.

Combining these factors would lead to a sensitivity increase of a factor of ~ 70 . Assuming the same flare temperature, *NuSTAR* could observe QS flares with EMs of $\sim 8 \times 10^{42} \text{ cm}^{-3}$ and thermal energies of $\sim 7 \times 10^{25} \text{ erg}$. Assuming the flare frequency distribution index of 2, we would expect ~ 15 events per hour within the *NuSTAR* field of view. Of course, smaller events might have lower temperatures and/or different areas than the events presented here, making it difficult to estimate a lower limit of the energy content that can be reached. Even if we do not reach such low energies, observing even a few events per hour would be a significant step forward to a statistical study, which would provide further insights into the energy content and heating processes in the faintest impulsive events on the Sun.

Bibliography

Arnaud, K. A. 1996, *Astronomical Data Analysis Software and Systems V*, **101**, 17

- Aschwanden, M. J., Schwartz, R. A., & Alt, D. M. 1995, *ApJ*, **447**, 923
- Aschwanden, M. J., Tarbell, T. D., Nightingale, R. W., et al. 2000, *ApJ*, **535**, 1047
- Benz, A. O., & Krucker, S. 1999, *A&A*, **341**, 286
- Benz, A. O., & Krucker, S. 2002, *ApJ*, **568**, 413
- Browning, P. K., Gerrard, C., Hood, A. W., Kevis, R., & van der Linden, R. A. M. 2008, *A&A*, **485**, 837
- Feldman, U., Mandelbaum, P., Seely, J. F., Doschek, G. A., & Gursky, H. 1992, *ApJS*, **81**, 387
- Gehrels, N. 1986, *ApJ*, **303**, 336
- Glesener, L., Krucker, S., Hannah, I. G., et al. 2017, *ApJ*, **845**, 122
- Grefenstette, B. W., Glesener, L., Krucker, S., et al. 2016, *ApJ*, **826**, 20
- Guerreiro, N., Haberreiter, M., Hansteen, V., & Schmutz, W. 2017, *A&A*, **603**, A103
- Guerreiro, N., Haberreiter, M., Hansteen, V., & Schmutz, W. 2015, *ApJ*, **813**, 61
- Hannah, I. G., Christe, S., Krucker, S., et al. 2008, *ApJ*, **677**, 704
- Hannah, I. G., Hudson, H. S., Battaglia, M., et al. 2011, *Space Sci. Rev.*, **159**, 263
- Harrison, F. A., Craig, W. W., Christensen, F. E., et al. 2013, *ApJ*, **770**, 103
- Hudson, H. S. 1991, *Sol. Phys.*, **133**, 357
- Katsukawa, Y., & Tsuneta, S. 2001, *ApJ*, **557**, 343
- Klimchuk, J. A. 2006, *Sol. Phys.*, **234**, 41
- Krucker, S., & Benz, A. O. 1998, *ApJL*, **501**, L213
- Krucker, S., & Benz, A. O. 2000, *Sol. Phys.*, **191**, 341
- Krucker, S., Benz, A. O., Bastian, T. S., & Acton, L. W. 1997, *ApJ*, **488**, 499
- Lemen, J. R., Title, A. M., Akin, D. J., et al. 2012, *Sol. Phys.*, **275**, 17
- Lin, R. P., Dennis, B. R., Hurford, G. J., et al. 2002, *Sol. Phys.*, **210**, 3
- Marsh, A. J., Smith, D. M., Glesener, L., et al. 2017, *ApJ*, **849**, 131
- Neupert, W. M. 1968, *ApJL*, **153**, L59
- Parker, E. N. 1988, *ApJ*, **330**, 474
- Parnell, C. E., & Jupp, P. E. 2000, *ApJ*, **529**, 554
- Porter, J. G., Toomre, J., & Gebbie, K. B. 1984, *ApJ*, **283**, 879
- Shimizu, T. 1995, *PASJ*, **47**, 251
- Shimizu, T., & Tsuneta, S. 1997, *ApJ*, **486**, 1045
- Tajfirouze, E., & Safari, H. 2012, *ApJ*, **744**, 113
- Veronig, A. M., Brown, J. C., Dennis, B. R., et al. 2005, *ApJ*, **621**, 482
- Terzo, S., Reale, F., Miceli, M., et al. 2011, *ApJ*, **736**, 111
- Walsh, R. W., & Ireland, J. 2003, *A&A Rev.*, **12**, 1
- Wright, P. J., Hannah, I. G., Grefenstette, B. W., et al. 2017, *ApJ*, **844**, 132

BIBLIOGRAPHY

Chapter 6

Summary and outlook

This chapter brings conclusions of the thesis and an outlook to the future. Section 6.1 is reserved for the summary and discussion of the most important results and possible follow-up studies. We continue with the possibilities of combining *NuSTAR* observations with instruments in other wavelength regimes (Section 6.2). A special emphasis is given to the Atacama Large Millimeter/submillimeter Array (ALMA), a new radio facility located in Chile and providing exciting new observations with unprecedented spatial resolution and sensitivity in the (sub)millimeter range. Section 6.3 gives an outline of the most important new and future instruments in solar physics, both ground-based and in-space.

6.1 Summary of presented and possible follow-up studies

6.1.1 *STIX* grids calibration

In Chapter 2 we presented the method for the analysis and full calibration of grids used for imaging X-rays in *STIX*. The method used both optical and X-ray data obtained at the Paul Scherrer Institute in Villigen (Switzerland). The data sets are complementary and they are both essential in order to extract all the (geometrical) grid parameters which will serve as an input to the data analysis software.

STIX grids were produced through the process of chemical etching of $\sim 30 \mu\text{m}$ tungsten foils. 12 layers of tungsten foils were stacked together to obtain the needed thickness of $\sim 400 \mu\text{m}$. In order to obtain sufficiently small periods in the range $38 - 54 \mu\text{m}$ for windows 11, 12, 13, 17, 18, 19, those grids were produced in a different way than the other windows. Here, not 12 but 6 (windows 12, 17, and 19) or 4 (windows 11, 13, and 18) layers of tungsten foils were stacked together and displaced relative to each other to obtain the needed periods. This is shown in Figure 6.1. However, this geometrical structure leads to significantly different transmission profiles than for the single-stack windows. Simulations of the transmission profiles in the case of two- and three-stacked grids are shown in the left and right panels of Figure 6.1, respectively. Similar profiles can be observed in the obtained X-ray data sets. However, their analysis is much more complicated as the profiles are dependent on the properties of each individual stack. A careful optical analysis will be performed for each stack separately. However, because

their images are quite different from the single-stack windows, this is planned for detailed future analysis and it is outside the scope of the thesis.

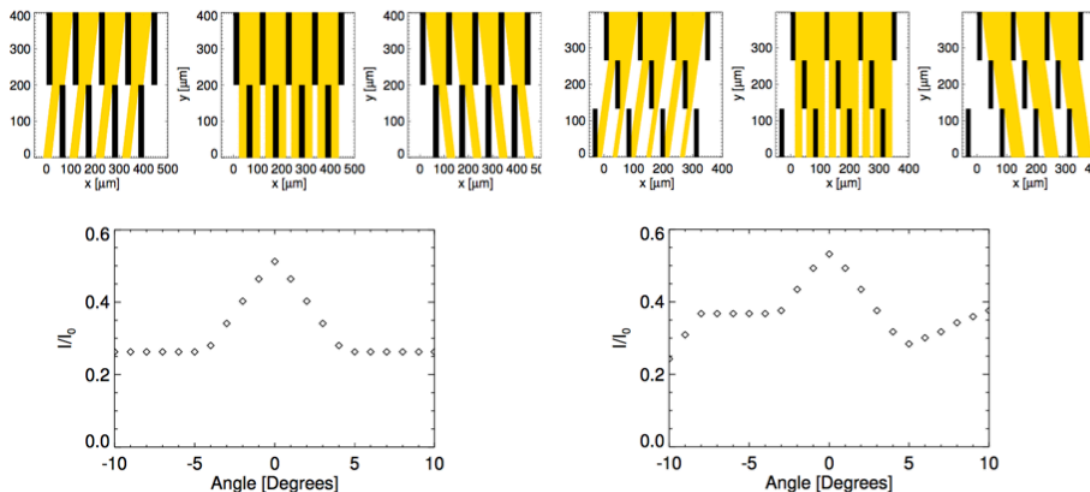


Figure 6.1: Simulated transmission profiles for grids produced of two (left) and three (right) layers of etched tungsten. The upper panels show the paths of light for -10, 0 and 10 degrees, nicely indicating the asymmetry observed in the profiles of the finest grids.

6.1.2 Correlation of HXR and WL emission

The statistically significant sample of 43 flares confirmed good correlation between the HXR and WL emission in solar flares (Chapter 3). The correlation is best observed for electrons of ~ 50 keV, reaching value of 0.68. The correlation decreases steeply for lower energies, while the decrease is slower at higher energies. This suggests that the high energy tail (above 50 keV) of the electron distribution produces WL emission, while less energetic electrons get stopped higher in the chromosphere and heat the chromosphere to million degree temperatures.

Three possible follow-up studies are considered: extending the analysis to less energetic events (*GOES* class C and smaller), the investigation of what seems a clear cutoff of WL intensity observed in the correlation plots, and the analysis of the connection between HXR and EUV emission in flares from the sample. The problem in optical observations of less energetic flares lies in the fact that their WL emission is often masked by ever-present intensity fluctuations of the photosphere. However, it would be most interesting to see whether they follow the same distribution as the strongest ones, as the WL emission in smaller flares has been observed only seldomly. Because the HMI data archive is quite big (more than ~ 7 years of continuous observations), the statistically significant sample of small flares should be obtained. The second study would concentrate on the most efficient WL producers, observed to follow a clear straight line in the correlation plots. This could point to the maximum contribution of WL emission in the total energy budget of solar flares. The targets of interest for the two possible studies

are highlighted in blue and red in Figure 6.2. Finally, in order to test the scenario in which lower energy electrons heat the chromospheric plasma to coronal temperatures and the more energetic ones cause WL emission, the correlation between EUV and HXR emission for the same set of flares is planned for investigation, using the de-saturation algorithm for AIA images (Schwartz et al. 2014).

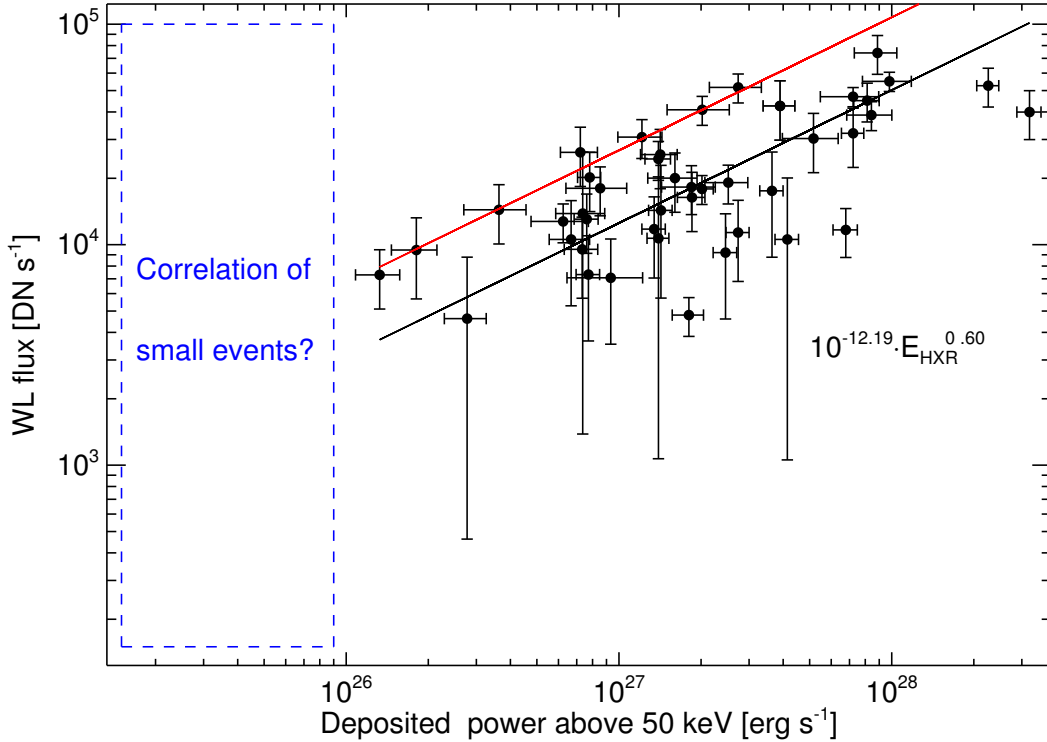


Figure 6.2: Possible future studies concerning WL emission in solar flares: correlation for smaller events (blue) and the most efficient WL events (red).

6.1.3 Long-lasting emission in the gradual phase

NuSTAR observed a curious X-ray emission above the west limb on 2014 December 11 (Chapter 4). We were able to connect this emission to the solar flare occurring 24 hours before *NuSTAR* observations, at ~ 18 UT on 2014 December 10. Such a long-lasting emission can be explained by the continuous formation of new flare loop systems arching ever higher in the solar corona. Their estimated total energy content might be an order of magnitude larger than the one derived at flare peak. The revision of the standard approach in estimating flare energetics, where the energy is calculated just from flare peak time, is suggested, as it obviously leads to a large underestimation of the true value.

Additionally to the 2014 December 11 observations, late phase emissions have been observed with *NuSTAR* in 2017 September 11 – 13. This time, the run was

part of an accepted observing proposal. The observations covered three days, each time in the duration of a few hours, and targeted an occulted active region on the eastern limb. The observation times are depicted with gray boxes in the *GOES* time evolution plot in Figure 6.3. The start of the campaign was on 2017 September 11, one day after the last of four X-class flares occurring that month. As in the 2014 December 11 run, the high coronal emission might prove to be connected to the flare occurring long before the observations. *NuSTAR* maps of the occulted region are shown in Figure 6.3 for each observing day. In the first two days, emission from the occulted active region can be clearly seen, probably representing X-ray emission from the tops of the loop systems. Due to the high occultation, no emission from the active region can be seen on the last day, and the detected counts are dominated by ghost-rays. Since *RHESSI* covered the peak of the flare on 2017 September 10, the combined observations will provide a much more complete picture of the peak- and late-phase evolution than for 2014 December 10 flare. Furthermore, much more *NuSTAR* data is available than before (~ 24 hours compared to 25 minutes on 2014 December 11).

6.1.4 X-ray emission from flares in the quiet Sun

Three small X-ray flares in the quiet Sun were observed with *NuSTAR*, one on 2016 July 26 and the other two on 2017 March 21 (Chapter 5). *NuSTAR* allowed the first X-ray imaging spectroscopy observations of these events. Their emission reached only low energies up to ~ 5 keV. Spectral fits revealed temperatures in the range 3.2 – 4.1 MK and emission measures of $(0.6 - 15) \times 10^{44} \text{ cm}^{-3}$. *NuSTAR* spectra did not show direct evidence of a nonthermal or higher temperature component. The calculated upper limits of a (hidden) nonthermal component were comparable to the thermal energy estimates. Hence, the lack of a nonthermal component in the spectra is not viewed as a constraining result, but might be caused by the insufficient sensitivity and imperfect observing conditions.

In future solar observations during solar minimum, even smaller events with energies in the 10^{25} erg range are expected to be observed. Since their occurrence is expected to be of the order of few events per hour within the *NuSTAR* FoV, enough events for a statistical study should be acquired, which would be an important step towards detecting (nonthermal) X-ray emission in nanoflares.

6.2 Simultaneous observations with ALMA and other instruments

In the context of small events, simultaneous observations with ALMA are particularly interesting as they allow studying the chromospheric response associated with the heating seen by *NuSTAR* in the corona. ALMA is currently the world's largest ground-based astronomical facility, consisting of 66 antennas that provide observations of astrophysical phenomena including the Sun in the (sub)millimeter range. Solar imaging observations can be performed in two

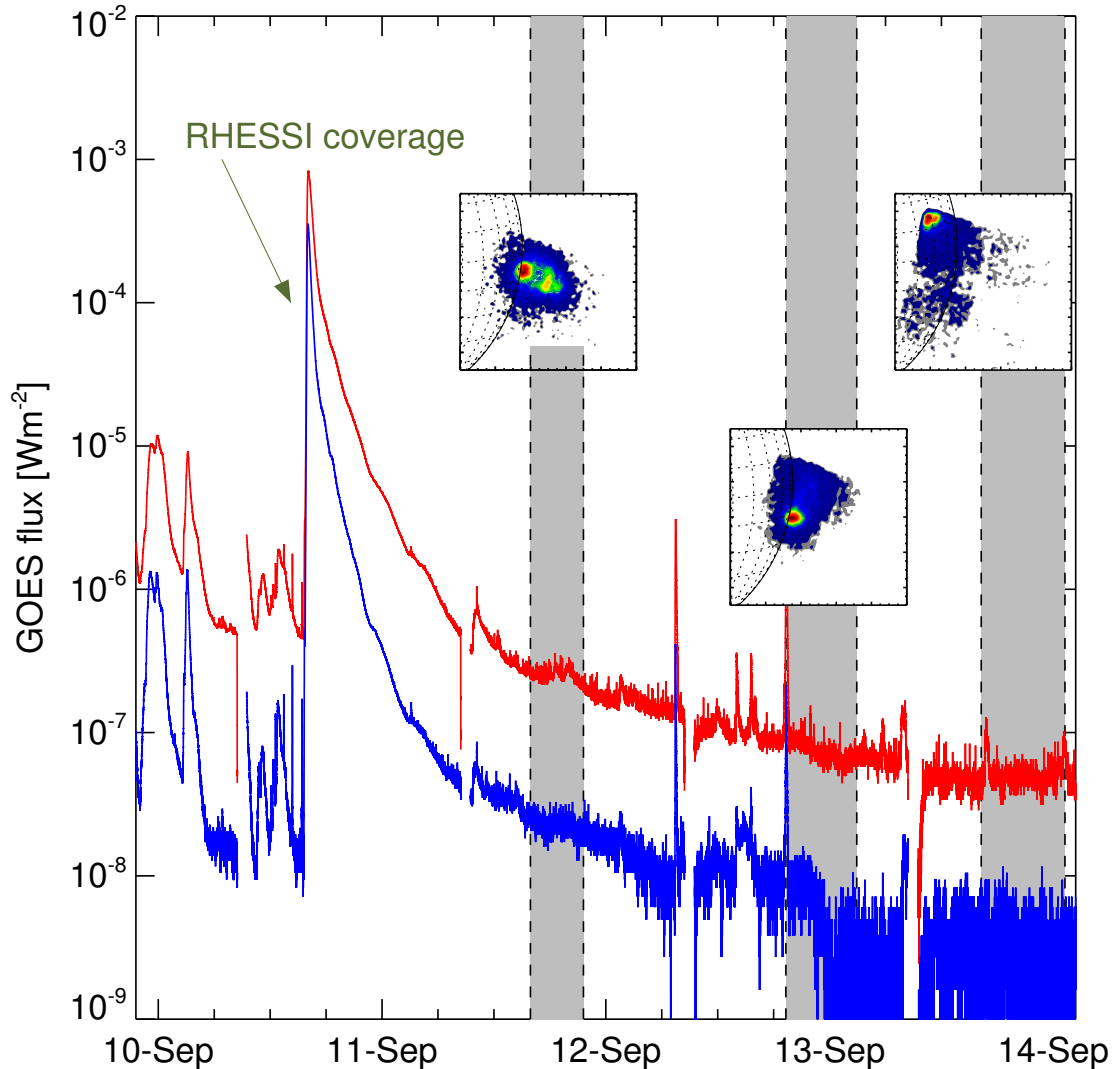


Figure 6.3: *GOES* 1 – 8 Å (red) and 0.5 – 4 Å (blue) time evolution of the full solar disk emission on 2017 September 10 – 14. The last of four X-class flares that month occurred on 2017 September 10 at ~ 16 UT, showing the largest increase in emission. In the days that followed, a gradual decrease of *GOES* SXR flux was observed, with a few flares occurring at various locations on the solar disk, represented by sharp peaks. *NuSTAR* observing times are marked by grey areas within the vertical dashed lines. *NuSTAR* images above 2.0 keV of the occulted active region and tops of remaining flare loops during each of these observations are also shown. The emission in the last day is too faint to be observed, probably due to the very high occultation, and is dominated by the ghost-ray emission from a bright source to the north-east (note that the ghost-ray emission is strongest in the top-left corner of the *NuSTAR* FoV).

modes: single-dish and interferometric. Single-dish mode, which involves scanning the Sun with a single antenna, has already been used to obtain full-disk images (solar mosaics, see White et al. 2017). However, the full advantages of ALMA are obtained in the interferometric mode, where information from all antennas is combined. This has been shown in the work by Shimojo et al. (2017), even though only 30/66 antennas were used. Of course, the FoV in this mode is limited, implying that the target for the observation has to be known. However, a high time cadence of ~ 1 s can be achieved. Therefore, there is a trade-off between time cadence, FoV and angular resolution between the modes, and the usage of each is dependent on the science questions addressed. Example images from both campaigns are shown in Figure 6.4, which nicely illustrates the advantages and downsides of both approaches.

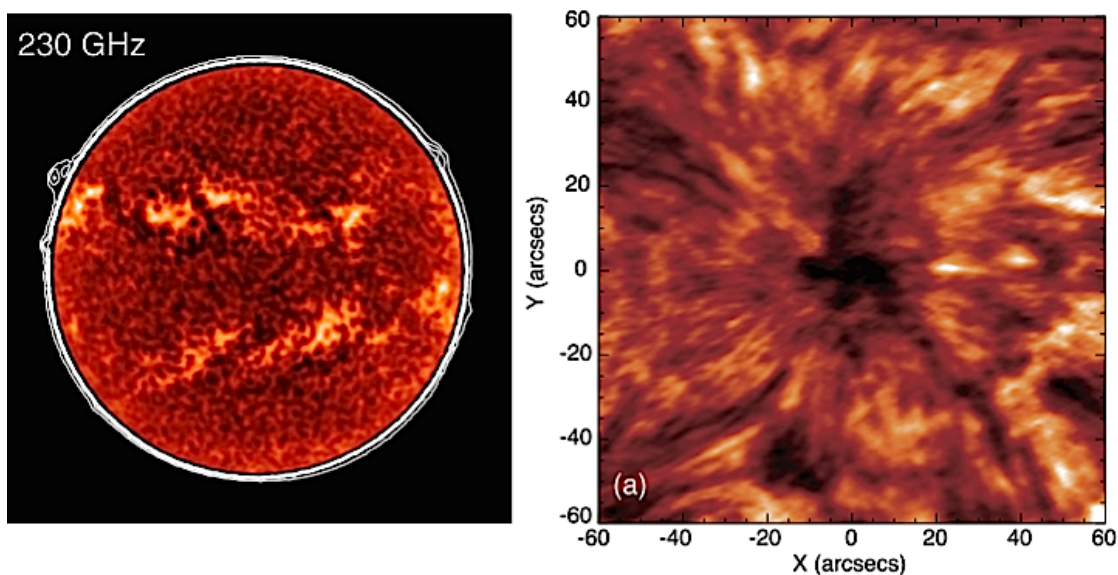


Figure 6.4: ALMA band 6 (230 GHz/1.3 mm) images of the Sun. *Left:* Mosaic image taken in the single-dish mode on 2015 December 17 (White et al. 2017). *Right:* Image of a sunspot taken in the interferometric mode on 2015 December 18 (Shimojo et al. 2017).

ALMA is particularly interesting for simultaneous observations with *NuSTAR*, because it has sufficient sensitivity for the faintest phenomena on the Sun. As the ALMA (sub)millimeter emission comes from the chromosphere, the two instruments can be combined to acquire the full picture of flare energization, in both the chromosphere and the corona. With that in mind, the FHNW heliophysics group has submitted an SNF proposal with their Croatian colleagues from Hvar observatory for combined ALMA/*NuSTAR* observations. Each group is specialized in one of the instruments, maximizing the synergy. Some of the important envisioned outcomes are:

1. Observations of coronal X-ray bright points with *NuSTAR* (X-ray), ALMA (radio) and AIA (EUV). Estimates of the energy in the corona and the chromosphere in these structures will be obtained, which will help understanding the energy partition between different atmospheric layers. An example

6.2. Simultaneous observations with ALMA and other instruments

of combined ALMA, *GOES/SXI* and *AIA* observations of a bright point is shown in Figure 6.5, nicely illustrating the advantages of this approach.

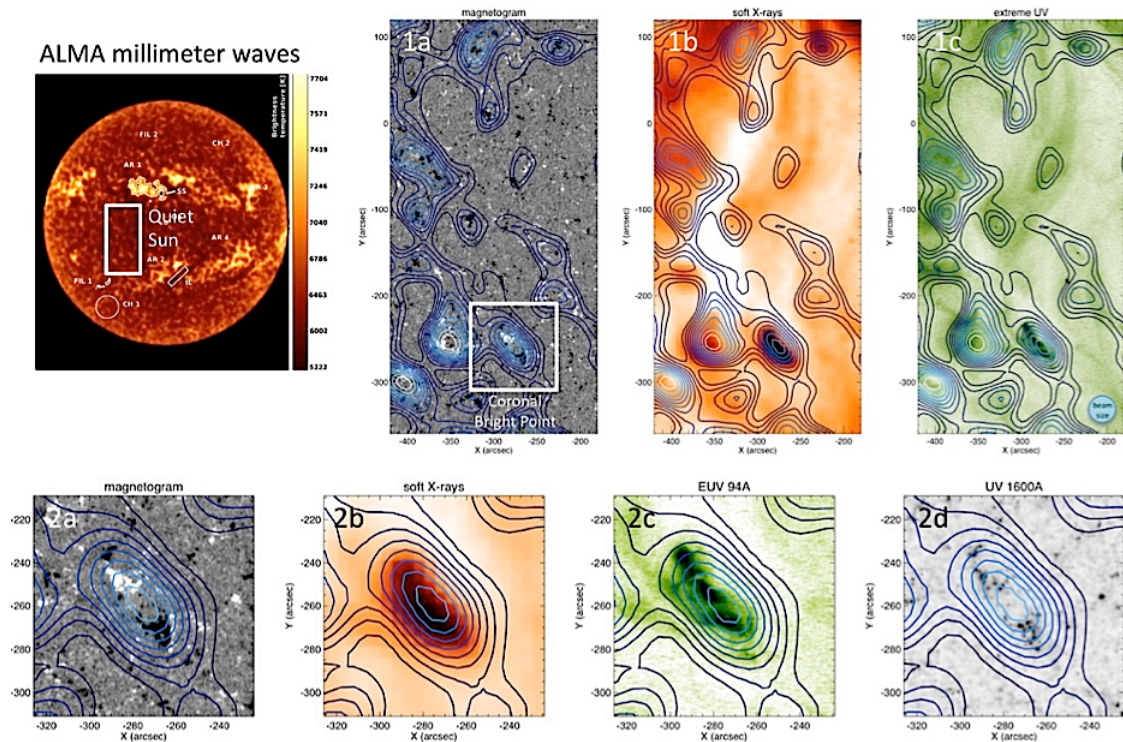


Figure 6.5: ALMA, *GOES/SXI* and *AIA* observations of an X-ray bright point. The top left panel shows ALMA full-disk image. Panels 1a-c represent the disk area depicted with the white box. Images show magnetic field strengths (a), X-ray emission (b) and EUV (c) emission. Bottom panels represent zoomed-in images of the X-ray bright point, showing a nice overlay of different instruments. ALMA contours are shown in blue.

2. Observations of QS flares in X-rays, radio, EUV and $H\alpha$. Combining observations in all of these wavelengths will hopefully resolve the questions on relative timing between chromospheric and coronal heating, as well as the energy partition between them in solar flares. Also, we expect to obtain temperature distributions of the heated plasma from SXR and EUV observations, and to obtain better estimates of their total energy. The existing observations are enough to fulfill this package, with some interesting ALMA campaigns during *NuSTAR* solar observation runs expected to become public in summer 2018. We show one of these in Figure 6.6, with the ALMA FoV represented with the green circle. The QS flare reached only modest temperature of ~ 2.6 MK and it is estimated to be the least energetic event observed with *NuSTAR* so far.
3. Direct detection of nonthermal emission in QS flares with ALMA through observation of the synchrotron emission. As nonthermal bremsstrahlung emission might be too faint to be observed in X-rays with *NuSTAR*, the

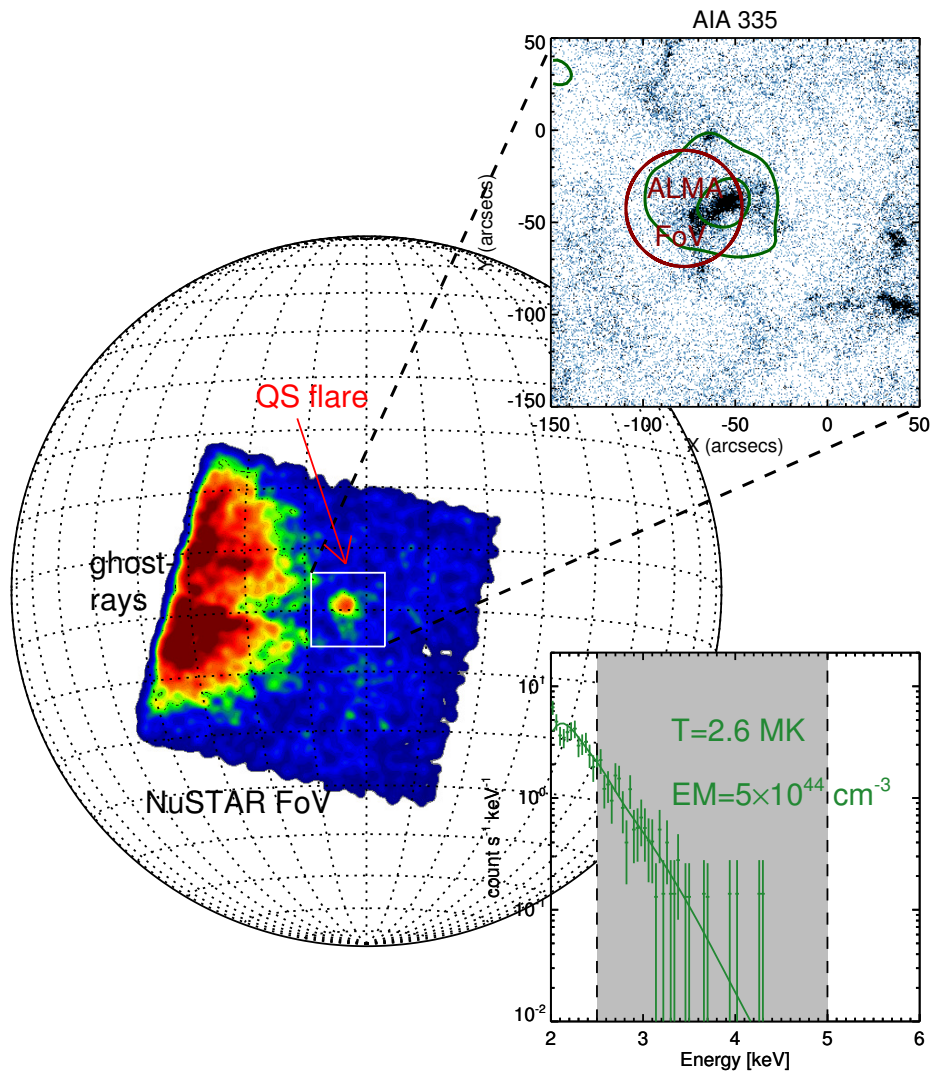


Figure 6.6: An example of overlapping ALMA and *NuSTAR* observations of a QS flare. Even though ALMA data of this campaign are not public yet, the flare was located within its FoV.

alternative approach involves using ALMA's two wavelength bands simultaneously, in order to measure spectral shape of QS flares in the radio domain. The thermal emission is expected to have a flat spectrum with frequency, while the nonthermal synchrotron emission shows a decrease. Both types of spectra have been observed in microwave data (Krucker et al. 1997) from the Very Large Array (VLA). Even though extrapolating VLA data to the ALMA frequency range implies a low nonthermal signal in the range 0.1 – 1.0 Jansky, it might still be strong enough to be detected. The nonthermal emission in ALMA frequency range is caused by synchrotron emission of relativistic electrons (MeV energy range), and not bremsstrahlung emission from weakly relativistic electrons as in the case of HXRs. The detection

of this radiation would represent one of the key findings in explaining the hot temperatures observed in the corona.

To conclude, ALMA observations of QS flares would provide two additional (crucial) pieces of information on QS flares: their chromospheric response to heating and an independent measurement of their nonthermal emission. First would give insights into the energy partition between the chromosphere and the corona in QS flares, the information which could be also used or scaled for other flares. The second one is maybe even more important and represents an even better chance of the direct detection of nonthermal signal in spectra of QS flares. As the nonthermal emission in the ALMA frequency range is caused by the synchrotron and not bremsstrahlung radiation, this measurement is not critically dependent on densities but on magnetic fields. A study of one QS flare candidate for which we potentially have both ALMA and *NuSTAR* data (there is some uncertainty about ALMA pointing) is envisioned in immediate future. Furthermore, FHNW and Hvar observatory have submitted an ALMA observing proposal in April 2018 just for this purpose. Therefore, more simultaneous *NuSTAR*/ALMA observations of QS flares are expected in future ALMA observing cycles.

6.3 What is next in solar physics?

6.3.1 Focusing optics in X-rays

In addition to European efforts in developing *STIX*, our American colleagues at the NASA Goddard Space Flight Center are currently leading the efforts on the solar-dedicated focusing optics X-ray imager *FOXSI* as a spacecraft mission (see Figure 6.7). Focusing optics allows much better dynamic range and orders of magnitude lower background rates compared to indirect imaging. This will allow observations of coronal and chromospheric X-ray sources simultaneously, which was not possible with *RHESSI* and other previous instruments, as the intensity ratio of these sources lies in the range of ~ 100 . Observing the coronal source simultaneously with and separately from the chromospheric one at very low energies will help in understanding acceleration mechanisms in solar flares and provide accurate estimates of the low energy cutoff discussed in Chapter 1. Also, *FOXSI* images will be free of artifacts coming from the image reconstruction methods based on Fourier analysis and implemented in *RHESSI* and *STIX*. Some of these advantages were already shown in *FOXSI* sounding-rocket flights and can be seen in Figure 1.18.

FOXSI fits within the NASA Small Explorer (SMEX) programme and its current design is shown in Figure 6.7. Some of the most interesting properties include the FoV of $9 \times 9'$, spectral resolution below 1 keV in the 3 – 70 keV range and angular resolution of $8''$ at full-width half-maximum (Christe et al. 2017). *FOXSI* will be optimally designed for observations of solar flares (of different scales) and quiescent active regions. Its dynamic range, estimated at a factor

of 100 for well separated sources ($> \sim 20''$), combined with much lower background when compared to *RHESSI*, will make it much more sensitive to fainter X-ray sources. *FOXSI* is currently in a competitive phase A study¹ and, if selected, it is planned to start observations at the onset of the next solar maximum in 2022. The selection of this mission by NASA would be extremely important for solar physics, as it would continue on the legacy of *RHESSI* as a solar-dedicated X-ray telescope. The NASA decision on funding is expected in April 2019. In the meantime, the group is preparing another *FOXSI* proposal, this time in combination with an EUV slit spectrograph, for the Medium-Class Explorers (MIDEX) mission.

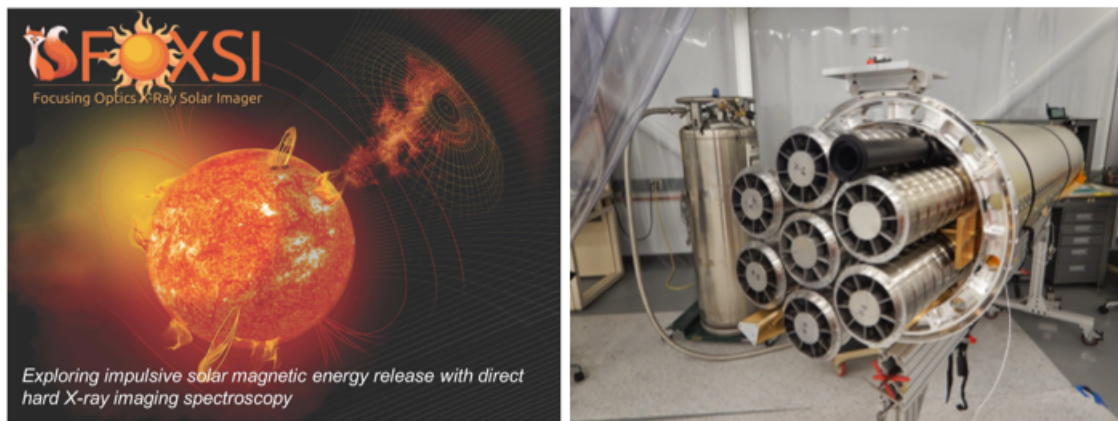


Figure 6.7: FOXSI telescope.

6.3.2 Other wavelengths

Beyond X-ray instruments, a variety of instruments in other wavelength regimes are scheduled for launch (space-based) or construction (ground-based) in the next decade. First in line, *Parker Solar Probe* was launched in August 2018 and it contains multiple instruments to acquire information on solar wind properties, solar magnetic fields and the corona. It will perform in-situ measurements at a distance as close as $\sim 8.5 R_{\odot}$ above the photosphere (Fox et al. 2016). The Daniel K. Inouye Solar Telescope (DKIST) is a ground-based solar telescope currently under construction on Haleakalā (Hawaii) and scheduled for first observations in 2019. It will observe in the visible and the infrared range and contain instruments for high spatial/temporal resolution imaging, spectropolarimetry, and magnetic field measurements (Tritschler et al. 2016). In the radio domain, exciting results are coming from the upgraded facilities at the Very Large Array (VLA), ALMA just started to use full capabilities during solar observations, while LOw-Frequency ARray (LOFAR, van Haarlem et al. 2013) is the newest radio interferometer operating in the range 10 – 240 MHz, with new stations being added across the whole Europe. Expanded Owens Valley Solar Array (EOVSA) is a

¹ <https://www.nasa.gov/press-release/nasa-selects-proposals-to-study-sun-space-environment>

radio interferometer operated by the New Jersey Institute of Technology (NJIT) and performing observations in the band 1 – 18 GHz. The project expanded on the Owens Valley Solar Array (OVSA) by adding new antennas and replacing some of the old facilities². Its importance lies in the fact that it is solar-dedicated, and all of the observing time is reserved for solar physics topics. Finally, as the flagship European project in the next decade, the *Solar Orbiter* mission is emphasized again. Besides *STIX*, it will contain 9 additional instruments, both in-situ and remote-sensing³. Especially interesting for the high-energy solar physics are stereoscopic studies of solar flares with *STIX* and *MiSolFa*, allowing for the first time the direct measurement of the directivity of the accelerated electron population.

6.3.3 Bright future

Finally, I would like to reinstate the importance of understanding our closest star in detail. I am sure that the Sun will remain one of the key targets of scientific interest considering its proximity and importance, not only to scientists, but also to the whole human civilization. Or, as Copernicus stated⁴

Finally we shall place the Sun himself at the center of the Universe.

Bibliography

- Christe, S., Shih, A. Y., Krucker, S., et al. 2017, AGU Fall Meeting Abstracts, , SH44A07
 Fox, N. J., Velli, M. C., Bale, S. D., et al. 2016, Space Sci. Rev., **204**, 7
 Krucker, S., Benz, A. O., & Aschwanden, M. J. 1997, A&A, **317**, 569
 Schwartz, R. A., Torre, G., & Piana, M. 2014, ApJL, **793**, L23
 Shimojo, M., Bastian, T. S., Hales, A. S., et al. 2017, Sol. Phys., **292**, 87
 Tritschler, A., Rimmele, T. R., Berukoff, S., et al. 2016, Astronomische Nachrichten, **337**, 1064
 van Haarlem, M. P., Wise, M. W., Gunst, A. W., et al. 2013, A&A, **556**, A2
 White, S. M., Iwai, K., Phillips, N. M., et al. 2017, Sol. Phys., **292**, 88

² <http://ovsa.njit.edu/>

³ The list of instruments and their most important science goals can be found at: <http://sci.esa.int/solar-orbiter/51217-instruments/>

⁴ https://en.wikiquote.org/wiki/Nicolaus_Copernicus

BIBLIOGRAPHY

Curriculum vitae

PERSONAL

Name: Matej Kuhar
Date of birth: 3.8.1990.
Place of birth: Slavonski Brod, Croatia
Nationality: Croatian
Marital status: married

EDUCATION

9/2014 – 8/2018 Doctoral studies at the Institute for Particle Physics and Astrophysics, ETH Zürich, Switzerland, and in collaboration with the Institute for Data Science, University of Applied Sciences and Arts Northwestern Switzerland

Doctoral thesis: *Through X-ray eyes: Solar flares and advances in observational techniques*

7/2009 – 9/2014 Master of physics studies at the Faculty of Science, University of Zagreb, Croatia

Master thesis: *Modelling radiation from the solar atmosphere in the sub-mm, mm and cm wavelength range*

9/2005 – 5/2009 Gymnasium Matija Mesić, Slavonski Brod, Croatia

Natural sciences and mathematics course

7/1997 – 7/2005 Elementary school Ivan Goran Kovačić, Slavonski Brod, Croatia

EXPERIENCE

9/2014 – 8/2018 PhD student (ETH)/Research Assistant (FHNW)

Publications

Publications in refereed journals

1. Krucker, S.; Saint-Hilaire, P.; Hudson, H. S.; Haberreiter, M.; Martínez Oliveros, J. C.; Fivian, M. D.; Hurford, G.; Kleint, L.; Battaglia, M.; **Kuhar, M.**; Arnold, N. G., 2015, *ApJ*, 802, 19
2. **Kuhar, M.**; Krucker, S.; Martínez Oliveros, J. C.; Battaglia, M.; Kleint, L.; Casadei, D.; Hudson, H. S., 2016, *ApJ*, 816, 6
3. Grefenstette, B. W.; Glesener, L.; Krucker, S.; Hudson, H. S.; Hannah, I. G.; Smith, D. M.; Vogel, J. K.; White, S. M.; Madsen, K. K.; Marsh, A. J.; Caspi, A.; Chen, B.; Shih, A.; **Kuhar, M.**; Boggs, S. E.; Christensen, F. E.; Craig, W. W.; Forster, K.; Hailey, C. J.; Harrison, F. A.; Miyasaka, H.; Stern, D.; Zhang, W. W., 2016, *ApJ*, 826, 20
4. **Kuhar, M.**; Krucker, S.; Hannah, I. G.; Glesener, L.; Saint-Hilaire, P.; Grefenstette, B. W.; Hudson, H. S.; White, S. M.; Smith, D. M.; Marsh, A. J.; Wright, P. J.; Boggs, S. E.; Christensen, F. E.; Craig, W. W.; Hailey, C. J.; Harrison, F. A.; Stern, D.; Zhang, W. W., 2017, *ApJ*, 835, 6
5. Wright, P. J.; Hannah, I. G.; Grefenstette, B. W.; Glesener, L.; Krucker, S.; Hudson, H. S.; Smith, D. M.; Marsh, A. J.; White, S. M.; **Kuhar, M.**, 2017, *ApJ*, 844, 132
6. Marsh, A. J.; Smith, D. M.; Glesener, L.; Hannah, I. G.; Grefenstette, B. W.; Caspi, A.; Krucker, S.; Hudson, H. S.; Madsen, K. K.; White, S. M.; **Kuhar, M.**; Wright, P. J.; Boggs, S. E.; Christensen, F. E.; Craig, W. W.; Hailey, C. J.; Harrison, F. A.; Stern, D.; Zhang, W. W., 2017, *ApJ*, 849, 131
7. Brajša, R.; Sudar, D.; Benz, A. O.; Skokić, I.; Barta, M.; De Pontieu, B.; Kim, S.; Kobelski, A.; **Kuhar, M.**; Shimojo, M.; Wedemeyer, S.; White, S. M.; Yagoubov, P.; Yan, Y., 2017, *A & A*, 613, 17
8. **Kuhar, M.**; Krucker, S.; Glesener, L.; Hannah, I. G.; Grefenstette, B. W.; Smith, D. M.; Hudson, H. S.; White, S. M., 2018, *ApJL*, 856, 32
9. Oka, M.; Birn, J.; Battaglia, M.; Chaston, C. C.; Hatch, S. M.; Livadiotis, G.; Effenberger, F.; Imada, S.; Miyoshi, Y.; **Kuhar, M.**; Eriksson, E.; Khotyaintsev, Y. V.; Retinò, 2018, *Space Sci. Rev.*, 214, 82

Publications in conference proceedings

1. Skokić, I; Brajša, R.; Sudar, D.; **Kuhar, M.**; Benz, A. O., Ninth Workshop 'Solar Influences on the Magnetosphere, Ionosphere and Atmosphere', proceedings of the conference held 30 May-3 June, 2017 in Sunny Beach, Bulgaria. Edited by K. Georgieva, B. Kirov and D. Danov. ISSN 2367-7570, 2017, p. 121-126